

# SILICON PHOTONIC MICRORESONATORS FOR MULTIPLEXING AND COHERENT OPTICAL SOURCES

A Dissertation

Presented to the Faculty of the Graduate School

of Cornell University

in Partial Fulfillment of the Requirements for the Degree of

Doctor of Philosophy

by

Brian Derek Stern

May 2018

© 2018 Brian Derek Stern  
ALL RIGHTS RESERVED

# SILICON PHOTONIC MICRORESONATORS FOR MULTIPLEXING AND COHERENT OPTICAL SOURCES

Brian Derek Stern, Ph.D.

Cornell University 2018

Silicon photonics allows optical waveguides to be integrated onto small chips and fabricated using scalable manufacturing. Integrated microresonators enhance the interaction between light and matter, enabling greater precision and control of light for a wide range of applications, including optical communications, sensing, and signal generation. This dissertation presents demonstrations of silicon photonic devices based on microresonators being used for switching, modulation, lasing, and four-wave mixing.

Silicon waveguides have the potential for extremely high bandwidth density and can use multiplexing approaches similar to those emerging in fiber communications networks. Spatial multiplexing uses a new degree of freedom to expand bandwidth capacity in waveguides. Mode-multiplexed waveguides in silicon enable such high capacities and help relieve design constraints related to the use of multiple lasers.

Here new functionalities for integrated mode-division multiplexing are presented. A fully-reconfigurable switch supporting multiple spatial modes and wavelengths is demonstrated. Additionally, an on-chip multimode link with three modes is demonstrated using integrated modulators.

In another demonstration, a silicon nitride microresonator is used in a hybrid semiconductor laser cavity to provide resonant feedback. A narrow laser linewidth is achieved by leveraging the length enhancement of the microres-

onator. Coherent communications and other phase-sensitive applications rely on such narrow laser linewidths.

In the final demonstration, which is a highlight of this dissertation, a fully-integrated frequency comb source is demonstrated. For the first time, a Kerr frequency comb is generated in an integrated microresonator without the need for an external laser. Soliton mode-locked combs are generated with extremely low power consumption, allowing battery operation of the compact comb source. This result could allow ubiquitous deployment of precise optical devices for sensing, spectroscopy, timing, and communications.

## BIOGRAPHICAL SKETCH

Brian Stern received his B.S. magna cum laude in Electrical & Computer Engineering from gorgeous Cornell University in 2013. In June 2013, he began doctoral research at Cornell with Professor Michal Lipson in the Cornell Nanophotonics Group. There he first worked on multiphoton neural imaging before settling on the topic of integrated photonics for optical communications. In 2015, Brian and Professor Lipson's research group moved to Columbia University in New York City. In New York, his research expanded to include integrated lasers, frequency combs, and phased arrays for lidar.

*Alla Luce*

## ACKNOWLEDGEMENTS

I would like to thank my advisor, Professor Michal Lipson, for enormous support and guidance during the completion of my Ph.D. Her unending optimism, creativity, and energy are truly incredible. Michal creates an environment for groundbreaking research to happen in a supportive atmosphere, and the results are always amazing. Her dedication to everything she does and tireless work ethic are inspiring, and the success of the group is largely due to that. While she emerged almost immediately as a leader in the field of silicon photonics, she has continually moved the group into new areas, both scientifically and geographically, and managed to become a leader in those areas as well. Michal has been an excellent teacher for demonstrating how to approach problems and present results. She has also always shown great warmth and personal concern for all of us working with her and has offered me generous help on many occasions. I am truly grateful for having the opportunity to work with Michal these past several years.

I also thank other mentors who contributed to my Ph.D. success. Professor Alexander Gaeta first introduced me to photonics and inspired further study in the field. He has also provided great insight while discussing research, especially during our collaboration on the frequency comb work. Professor Clifford Pollock taught an engaging course on lasers which further raised my interest in the topic. I also enjoyed the opportunity to discuss my work and hear his perspectives, especially when his office was adjacent to ours. Professor Keren Bergman has been a close partner on many research projects, including my multimode work. Moving to Columbia allowed much greater interaction between our groups, for which we both have benefited from being able to meet quite often. I would also like to thank Dr. Arthur Ballato, who introduced me to a lot of

classical science and culture and has always provided sage advice.

The members of the Cornell Nanophotonics Group (later Lipson Nanophotonics Group) were critical in supporting my research. In addition to helping on specific projects, the frequent discussions on topics both relevant and wholly irrelevant helped to make research more enjoyable and to provoke many new ideas. I can't thank Dr. Carl Poitras enough for guiding me at the beginning of my research and for teaching me so much about silicon photonics. I also deeply thank Professor Jaime Cardenas for everything he taught me, for his tremendous help with research, for staying late to help with e-beam, and for tacos (thank you Cecilia). Thank you Lawrence for passing on so much fabrication knowledge and for many discussions on modes and resonators. Thank you to Danny for passing on active fabrication know-how and industry expertise; to William for fabricating the best nitride waveguides in the world and for sharing ribs; to Avik for insightful discussions and dubious puns; to Austin for expertly guiding my first short project; to Steve for teaching me so much about frequency combs; to Aseema for advice on so many topics beyond just glue; to Chris for his help and knowledge about everything and anything; to Oscar for help with polishing and pretending to speak things we don't really speak; and to Gaurang for not touching the RF equipment in the winter. Thank you to everyone in the group with whom I have regularly discussed research and other topics: Moshe, Kevin, Mian, Romy, Shreyas, Bishu, Mohammad, Raphael, Amin, Felipe, Daniel, Ipshita, Brian, You-Chia, Euijae, Utsav, Lin, Sam, Min, Mateus, Goran, and Reuven. You have formed an amazing group, and it is not possible to list here everything you have done to help.

Also thank you to Lee, Christine, and Yoshi for helping with experiments. Thank you Kim and Krystal for keeping the group running, and thanks to Scott

for amazing department support. Thank you Woosung and Alberto for giving me an industry perspective. Thank you Travis and Jesse for helping me build my first, but not last, laser cavity. Finally I thank my family for everything they've done.

The work in this dissertation resulted not only from the work of me and my colleagues, but also built on the prior research of others, including those cited in the references. It is my hope that the work presented here will continue to advance the field of photonics and open new research areas.

## TABLE OF CONTENTS

Biographical Sketch . . . . .	iii
Dedication . . . . .	iv
Acknowledgements . . . . .	v
Table of Contents . . . . .	viii
List of Tables . . . . .	x
List of Figures . . . . .	xi
<b>1 Introduction</b>	<b>1</b>
1.1 Silicon photonics . . . . .	1
1.2 Organization of the dissertation . . . . .	4
<b>2 Integrated photonics</b>	<b>5</b>
2.1 Fiat lux: Waves and light . . . . .	5
2.2 Waveguides . . . . .	8
2.3 Coupled modes . . . . .	16
2.4 Microresonators . . . . .	19
2.5 Carrier depletion modulators . . . . .	26
2.6 Integrated photonic fabrication . . . . .	29
<b>3 Integrated lasers</b>	<b>32</b>
3.1 Electromagnetic radiation . . . . .	32
3.2 Lasers . . . . .	32
3.3 Pulsed and mode-locked lasers . . . . .	36
3.4 Semiconductor lasers . . . . .	37
3.5 Laser linewidth . . . . .	39
<b>4 Nonlinear optics and frequency combs</b>	<b>48</b>
4.1 Nonlinear optics . . . . .	49
4.2 Four-wave mixing . . . . .	50
4.3 Frequency combs . . . . .	52
4.4 Solitons . . . . .	54
<b>5 Mode multiplexing</b>	<b>57</b>
5.1 Switch . . . . .	57
5.1.1 Processing multimode signals . . . . .	58
5.1.2 Multimode switch . . . . .	59
5.1.3 Device fabrication . . . . .	62
5.1.4 Results . . . . .	64
5.1.5 Fabrication tolerance of mode multiplexing . . . . .	68
5.1.6 Discussion . . . . .	70
5.1.7 Scaling considerations for multimode switching . . . . .	71
5.2 Multimode on-chip link . . . . .	73

<b>6</b>	<b>Integrated narrow linewidth laser</b>	<b>81</b>
6.1	Introduction . . . . .	81
6.2	Cavity reflection assisted Si <sub>3</sub> N <sub>4</sub> laser . . . . .	82
6.3	Resonator and laser characterization . . . . .	87
6.4	Further linewidth reduction . . . . .	90
6.5	Conclusion . . . . .	91
<b>7</b>	<b>Fully integrated frequency comb source</b>	<b>93</b>
7.1	Introduction . . . . .	93
7.2	Integrated Kerr comb source . . . . .	95
7.3	Laser characterization . . . . .	99
7.4	Comb and soliton generation . . . . .	100
7.5	Discussion . . . . .	104
<b>8</b>	<b>Discussion and Future Directions</b>	<b>106</b>
8.1	Multimode silicon photonics . . . . .	106
8.2	Narrow linewidth lasers . . . . .	109
8.3	Microresonator frequency combs . . . . .	110
<b>A</b>	<b>Coupling to multimode fiber</b>	<b>113</b>
	<b>Bibliography</b>	<b>115</b>

## LIST OF TABLES

5.1	Table of coupling gaps for ring resonators in multimode switch. .	61
5.2	Table of implantation values for ring modulator. . . . .	76

## LIST OF FIGURES

1.1	Left: Magnetic-core memory made in 1968. Right: A modern CPU integrating a billion transistors. . . . .	2
1.2	Left: A tabletop optical setup with discrete, manually positioned components. (Courtesy of Andre Luiten). Right: Photonic chips integrating many optical components, fabricated on a silicon wafer. . . . .	3
2.1	Diagram of a planar slab waveguide cross-sectional view. The electric field direction $\hat{y}$ is out of the plane. . . . .	9
2.2	Cross-sectional view of a single-mode fiber. The index $n_1$ of the core is slightly higher than the index $n_2$ in the cladding. . . . .	11
2.3	Mode profiles for various modes of a few-mode fiber (FMF). . . . .	12
2.4	Cross-sectional profile for the TE <sub>0</sub> mode in a 250 x 450 nm silicon waveguide surrounded by SiO <sub>2</sub> at 1550 nm wavelength. Dimensions are in nm. Color scale units are V/m. The arrows show the magnitude and direction of $E_x$ . . . . .	13
2.5	Cross-sectional profile for the TE <sub>0</sub> mode in a 250 nm thick silicon waveguide surrounded by SiO <sub>2</sub> at 1550 nm wavelength. The waveguide width is varied from 300 nm to 800 nm. . . . .	14
2.6	Cross-sectional profile for modes in a 250 x 450 nm silicon waveguide surrounded by SiO <sub>2</sub> at varying wavelengths. Note that at 3000 nm, a wider view is used to show the entire mode. . . . .	15
2.7	Cross-sectional profile for the first three TE modes in a 250 x 1200 nm silicon waveguide surrounded by SiO <sub>2</sub> at 1550 nm wavelength. . . . .	15
2.8	Top view of two coupled waveguides as light is injected to the upper waveguide propagating towards the right. (a) Light couples back and forth between the waveguides. (b) A larger coupling gap reduces the coupling rate. (c) The two waveguides are set to unequal widths, so light never fully couples between them. . . . .	17
2.9	Cross sectional view of $E_x$ for two coupled silicon waveguides. . . . .	18
2.10	Diagram of a ring resonator, including the field in the bus waveguide $S_{in}$ , the field in the ring $a$ , the coupling between the two $\kappa$ , the ring propagation loss $\alpha$ , and the output field in the bus waveguide $S_{out}$ . . . . .	19
2.11	Spectral profile of transmission past ring resonator near $\omega_0$ . . . . .	21
2.12	Diagram of a ring resonator including a waveguide drop port. . . . .	23
2.13	Spectral profile of drop port transmission near $\omega_0$ . . . . .	23

2.14	(a) Through port transmission (power) of ring resonator with coupling between CW and CCW modes. The degenerate splitting corresponds to $\mu = 2.5 \times 10^8 \text{ rad s}^{-1}$ . $Q_0 = 1.5 \times 10^7$ and $Q_L = 4 \times 10^6$ . The x-axis range is $\omega_0 \pm 1 \times 10^9 \text{ rad s}^{-1}$ . (b) Reflected power in bus waveguide due to CCW mode, assuming the same conditions as (a). . . . .	26
2.15	(a) Calculated reflected power for varying coupling values ( $\kappa$ ), from undercoupling to near critical coupling. The coupling due to backscattering $\mu = 2.5 \times 10^8 \text{ rad s}^{-1}$ and $Q_0 = 1.5 \times 10^7$ are fixed. (b) Calculated reflected power for varying coupling values, from near critical coupling to overcoupling, assuming the same conditions as (a). . . . .	27
2.16	Band diagram of a silicon pn junction operating in reverse bias. . . . .	27
2.17	Basic fabrication steps for patterning silicon waveguides. . . . .	30
3.1	Energy density of blackbody radiation at 3,400 K according to Planck's law. The peak energy density occurs at $1.5 \mu\text{m}$ . . . . .	33
3.2	Band diagram of a double-heterostructure. . . . .	39
3.3	Intensity of optical field $E$ influenced by spontaneous emission with a random phase. . . . .	40
3.4	Diagram of an extended cavity laser, including a semiconductor-based gain section of length $L_0$ , and a passive section of length $L_1$ . . . . .	43
3.5	(a) Diagram of the conditions for lasing. The level of cavity loss (constant) must equal the gain, and only frequencies satisfying the integer-multiple phase condition may lase. Multiple modes with similar loss may lase in this case. (b) In the case of frequency-dependent loss, such as that introduced by a filter, a single mode may be selected to lase. . . . .	44
3.6	Phase response of a ring resonator close to resonance. . . . .	45
3.7	(a) Diagram showing change in lasing conditions in response to a change in gain. First, a perturbation in gain shifts the constant phase curve downwards. The lasing frequency is in turn shifted by an amount $\Delta\omega$ . (b) The same gain perturbation $\Delta g$ is applied to a cavity with steeper phase and loss profiles. This results in a smaller $\Delta\omega$ . (Based on [1]) . . . . .	46
4.1	Diagram showing degenerate four-wave mixing process, whereby a pump generates sidebands. Left: energy level diagram. Right: spectral diagram. . . . .	51

5.1	<p>In order to enable access to individual mode-multiplexed channels, multimode signals are temporarily encoded as the fundamental mode (step (1)), and are then processed independently (step (2)). Processing by variable attenuation is shown as an example for the case of 12 channels (three modes and four wavelengths). Finally, the channels are restored as higher-order spatial modes (step (3)) and coupled to a multimode waveguide output. . . . .</p>	59
5.2	<p>(a) Block diagram of 1x2 multimode switch operation. The four input data channels, consisting of two modes at two different wavelengths, may be switched in any combination to the two outputs. The example shows three channels routed to Output 1 and one channel to Output 2. (b) Schematic of multimode switch. The input <math>TE_1</math> channels are converted to the fundamental mode through phase-matching to single-mode rings. The channels are switched using actively-tuned rings to route them individually. This example shows three channels routed from Input 1 to Output 1 using on-resonance rings, and the fourth channel (<math>TE_0 \lambda_2</math>) is routed from Input 1 to Output 2 using an off-resonance ring. (c) Illustration of mode (re)conversion approach showing the phase-matched coupling region. . . . .</p>	60
5.3	<p>(a) Optical microscope image of fabricated device. The input channels are coupled into single-mode waveguides from an off-chip laser, and a multiplexer (mux) produces the MDM input to the multimode switch. The areas highlighted in blue show the multimode waveguides. The four small rings actively switch the four channels and are tuned by integrated heaters. Following the switch, each of the two outputs is demultiplexed (demux) so that the channels can be individually monitored off-chip. (b) SEM image of a ring resonator in the fabricated device with active heater used to tune the resonance. (c) Crosstalk measurements for the different channels. Spectral profiles at both outputs for each of the input four channels, compared with the profiles from interfering channels. . . . .</p>	63

5.4	(a) Testing configuration, including tunable laser, polarization controller, fiber polarizer, electro-optic modulator (Mod.), pattern generator (PG) for the $2^7 - 1$ pseudo-random binary sequence (PRBS), function generator clock source (CLK), Er-doped fiber amplifier (EDFA), tunable band-pass filter (1.4 nm), digital communications analyzer (DCA), variable optical attenuator (VOA), optical receiver (Recv.), limiting amplifier (LA), and bit-error rate tester (BERT). (b) Eye diagrams of the switched signals for all channels at both outputs are open. Comparison with the rise time of back-to-back eyes confirms that the output signal is bandwidth-limited. (c) Error free transmission ( $BER < 10^{-9}$ ) is achieved with power penalties ranging from 0.5 to 1.4 dB, compared to the back to back (B2B) references. . . . .	65
5.5	(a) Testing setup for simultaneous switching, derived from that of Figure 5.4a, includes fiber spools for decorrelation and decoherence of data channels, a 50:50 combiner/splitter, and pitch reducing optical fiber array (PROFA). Solid connections are in fiber, and dotted connections are electrical. (b) Eye diagrams for each 10 Gb/s channel switching to either output. (c) Bit-error rate measurements for simultaneous operation of all channels. The worst-case switching configuration for each channel is plotted. For each channel, a back to back reference was measured by replacing the PROFA and chip with an attenuator replicating the insertion loss. The best-performing back to back measurements for each wavelength are plotted. All channels achieve error-free ( $BER < 10^{-9}$ ) transmission, except the $TE_1\lambda_1$ channel, which is impaired when switched to Output 1 due to a fabrication error causing one ring resonator to be under-coupled with a narrow bandwidth. . . . .	67
5.6	(a) Method for accessing individual modes in a multimode waveguide. A single-mode ring resonator which is properly phase-matched to the bus waveguide will drop the $TE_1$ channel, while the $TE_0$ channel can be adiabatically tapered into a single-mode waveguide. (b) Simulated effective index of 250-nm tall Si waveguide as a function of width. The phase-matching condition is met when the index for $TE_0$ in the single-mode waveguide (point A) matches that of the $TE_1$ in the multimode bus waveguide (point B). The $TE_0$ signals can adiabatically taper to the same width as the multimode bus waveguide (point C) and back. . . . .	69
5.7	Sensitivity of phase-matching to width for coupling between $TE_0$ mode in 450 nm waveguide and $TE_1$ mode in 930 nm waveguide. The simulation shows a large tolerance for fabrication variations in width dimensions of waveguides. . . . .	70

5.8	Simulated mode transmission for adiabatic linear taper of width of multimode silicon waveguides. All modes rapidly reach high transmission when taper lengths exceed several micrometers. In (a), a taper from 1.41 $\mu\text{m}$ width to 1.85 $\mu\text{m}$ is 99% efficient in just 4 $\mu\text{m}$ , while in (b), from 1.85 $\mu\text{m}$ to 2.4 $\mu\text{m}$ , this efficiency is reached by 6 $\mu\text{m}$ . . . . .	72
5.9	Diagram of integrated multimode link design. A single laser is used for all three channels, while after modulation, each channel is multiplexed into its respective mode. At the end of the transmission region, the signals are demultiplexed. . . . .	73
5.10	Plot of effective index versus waveguide width for the modes supported in a multimode silicon waveguide. . . . .	74
5.11	(a) Microscope image of fabricated microring modulator before cladding and metal deposition. The yellow box around the ring is a remaining 50 nm slab of silicon, while elsewhere the waveguides are fully etched. (b) Cross-sectional view showing pn junction location in waveguide. (c). SILVACO simulation of dopant density following implantation and anneals. . . . .	76
5.12	Measured current-voltage characteristics of the ring modulator. Device operation for modulation is in reverse bias. . . . .	78
5.13	Plot of measured crosstalk and insertion loss for each channel accounting for the optimal wavelength of each. . . . .	78
5.14	(a) Microscope image of silicon chip showing microring modulators, mode multiplexers, and demultiplexers. (b) Eye diagrams at 12.5 Gb/s for the three modes. . . . .	79
6.1	(a) Schematic of our laser. The ring acts as a partial reflector by taking advantage of the coupling of the counter clockwise (CCW) propagating mode to the clockwise (CW) mode, which reflects light back into the cavity. (b) Comparison of the pass-by configuration used here (bottom), which leads to a high loaded $Q$ , with the commonly used add-drop configuration (top), which often leads to a lower loaded $Q$ . (c) Schematic of our laser cavity design (not to scale). . . . .	83
6.2	(a) Photograph of the coupled chips. Wirebonds are used to supply current to the RSOA, and needle probes (not shown) are used to apply voltage to the heater on the $\text{Si}_3\text{N}_4$ chip. (b) Measured transmission and reflection spectra of $\text{Si}_3\text{N}_4$ microring resonator. The degeneracy of the CW and CCW modes causes the resonance splitting (double peak), which is accounted for in the resonance fitting. . . . .	86

6.3	(a) Measured spectrum of laser output showing single-mode operation and high side mode suppression ratio (SMSR). (b) Measured uncooled laser output power at room temperature. (c) Measured spectra showing lasing across a wide range of wavelengths. By adjusting the voltage applied to the micro-heater integrated on the ring, lasing is obtained at discrete wavelengths within a 27 nm range. . . . .	88
6.4	(a) Delayed self-heterodyne (DSH) test set-up. EDFA: Erbium Doped Fiber Amplifier. PC: Polarization Controller. (b) Measured DSH beat note in radio frequency (RF) spectrum analyzer. The -40 dB width equals 200 times the Lorentzian linewidth, which is found to be 13 kHz here. The resolution bandwidth used is 10 kHz with 325 ms sweep time. . . . .	89
6.5	Calculated linewidth versus $Q$ , with current cavity parameters (blue), and improved coupling (red). Laser cavities based on $\text{Si}_3\text{N}_4$ have the potential to reach beyond the demonstrated 13 kHz linewidth and produce sub-Hz linewidths. . . . .	90
7.1	Concept illustration of an integrated Kerr comb source with an on-chip amplifier and microresonator. . . . .	94
7.2	(a) Microscope image and diagram of integrated comb source, including laser cavity and nonlinear microresonator for comb generation. The amplifier waveguide provides electrically-pumped optical gain and includes a reflective facet on one end, while the opposite side is coupled to the $\text{Si}_3\text{N}_4$ portion of the laser cavity. The microring filters are tunable using integrated microheaters. The larger microresonator generates a partially reflected beam to form a second effective mirror of the laser cavity. This microresonator also has a high $Q$ to enable FWM and comb generation. (b) Photograph of the fully integrated comb source. The RSOA is edge-coupled to the $\text{Si}_3\text{N}_4$ chip and supplied with electric current via wirebonds, while the comb output is measured using an optical fiber. . . . .	96

7.3	(a) Measured transmission spectrum for the Vernier filter rings. By adjusting the voltage applied to the microheaters, the filters relative detuning is adjusted and a single transmission wavelength is selected. (b) Measured optical transmission and reflection spectra (normalized) of the high- $Q$ microresonator. The 32-MHz resonance bandwidth reveals a $Q$ of $8 \times 10^6$ . The narrow-band reflection is generated by coupling via Rayleigh scattering between counter-propagating beams in the ring, which is apparent due to the resonance splitting observed from these degenerate beams. (c) Laser output spectrum showing single-mode lasing with over 60 dB side-mode suppression ratio (SMSR). (d) Output optical power of laser versus pump current at 1580 nm. . . . .	97
7.4	Simulated optical spectrum of soliton generated with 700 $\mu$ W optical pump power. The microresonator dimensions used in the model are $730 \times 1800$ nm with a radius of 120 $\mu$ m, corresponding to a 194 GHz FSR (pulse repetition rate). . . . .	98
7.5	(a-c) Spectra of output from comb source as measured by an optical spectrum analyzer (OSA) at varying stages of comb generation with corresponding RF spectra. A current supply provides 130 mW electrical pump power. (d) Frequency comb matching soliton profile generated with a AAA battery supplying pump power of 98 mW. Inset: RF spectrum showing low-noise state. Right: Photograph of integrated comb source with a printed circuit board and the battery. . . . .	101
7.6	(a) Simulation of single-soliton comb generated with 2.35 mW pump power. The microresonator dimensions used in the model are $730 \times 1800$ nm with a radius of 120 $\mu$ m, corresponding to a 194 GHz FSR (pulse repetition rate). (b) Optical spectrum of measured single-soliton comb (from Figure 7.5c) generated with 2.5 mW pump power. The $\text{sech}^2$ profile matches well with the simulated comb at slightly higher pump power. . . . .	102
7.7	(a) Schematic of the modular comb source configuration, based on the typical external pump scheme. Here the integrated laser is distinct from the nonlinear microresonator, with a Sagnac loop mirror serving as the laser output coupler. (b-d) Optical output spectra at varying stages of comb generation with corresponding RF spectra. . . . .	103
A.1	Diagram of an adiabatic multimode fiber coupler. Light from a few-mode fiber couples to a large integrated intermediate waveguide and then adiabatically to a silicon waveguide. . . . .	113

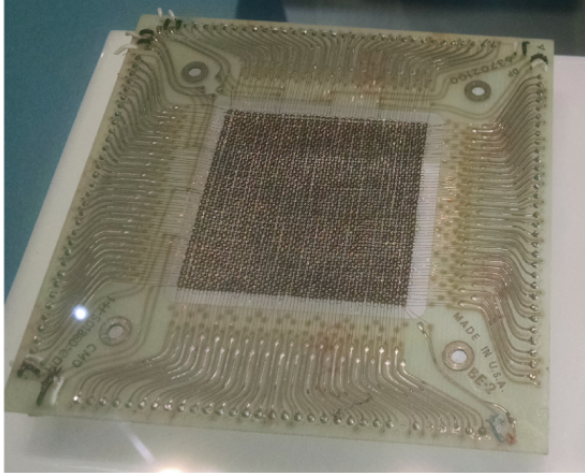
# CHAPTER 1

## INTRODUCTION

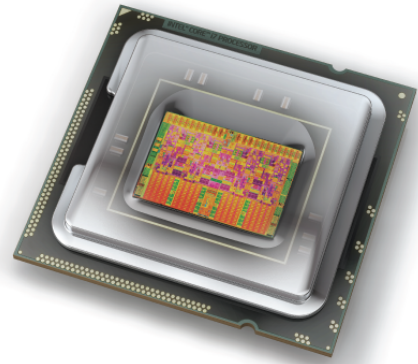
### 1.1 Silicon photonics

Silicon photonics is an emerging technology that leverages fabrication tools from the microelectronics industry in order to produce optical devices on silicon chips. Many applications are leveraging silicon photonics for different reasons. For optical communications, the immediate interest is reducing the cost and expanding the capabilities of transceivers for sending and receiving data over a distance. In the field of sensing, the high confinement of light in silicon waveguides and microscopic scale of integrated devices allow for enhanced optical sensitivity. Large complex systems such as optical phased arrays rely on the reliability of silicon to enable scalable integrated systems. As these areas now find commercial viability, advancements may allow for other applications, such as quantum optical circuits, to emerge as well.

In many ways, the progress of silicon photonics and its projected future are related to the story of electronic integration. Until the late 1960s, computer memory was hand-made by weaving wires and magnetic cores (Figure 1.1). This process was time-consuming, expensive, and not scalable to large amounts of memory. When memory and central processing units (CPUs) based on integrated electronics were first developed, the serial manufacturing of magnetic cores became a thing of the past. Silicon wafers could include many copies of electronic devices that could be fabricated in parallel. With decades of advancements since then, billions of transistors can now be integrated on a single CPU (Figure 1.1), allowing widespread adoption of computers and dramatic reduc-



Magnetic-core memory



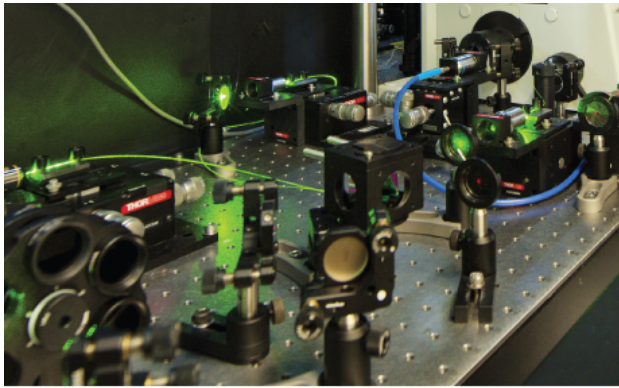
Modern CPU

Figure 1.1: Left: Magnetic-core memory made in 1968. Right: A modern CPU integrating a billion transistors.

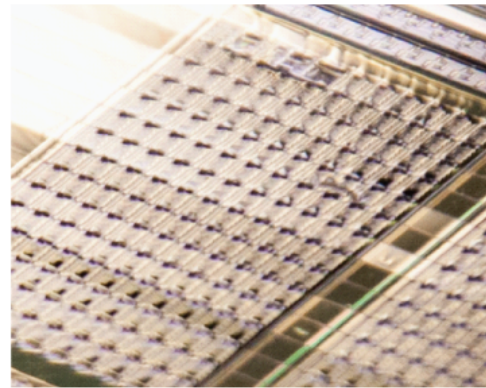
tions in cost (both per transistor and per computation).

An analogous trajectory for photonic integration is often projected. While integration of certain components, such as semiconductor lasers, has been common for decades, the promise of silicon photonics is that the high yield attained by the purity of crystalline silicon and the expertise in processing it will allow large-scale integration of optical devices. The discrete optical components common in tabletop optical setups and bulky photonic products can potentially be miniaturized and fabricated on wafers containing many chips. Besides the reduction in cost and size, the integrated devices are robust in that they cannot be misaligned due to e.g. vibrations. Additionally, the large-scale integration enables new applications such as optical phased arrays that would not be practical with manual assembly of components (Figure 1.2).

The dominant motivating force behind silicon photonics has been the potential to expand the capabilities of optical communications. While optical fibers



Tabletop optical setup



Silicon photonic chips

Figure 1.2: Left: A tabletop optical setup with discrete, manually positioned components. (Courtesy of Andre Luiten). Right: Photonic chips integrating many optical components, fabricated on a silicon wafer.

carrying high data bandwidths have been commonly used for telecommunications for decades, high bandwidths are needed more than ever at shorter and shorter distances, e.g. in data centers. Growing demand for bandwidth in metro networks, between switching racks in data centers, in supercomputers, and potentially on the board level will drive demand for large volumes of optical transceivers. The scalability of silicon photonics makes it a prime candidate for the task.

An essential component in silicon photonics is the microresonator. Microresonators offer a wide range of capabilities to silicon photonics for many applications, from data modulation to sensing to waveform generation. They bring greatly enhanced control to integrated photonic devices, and as such, they are the primary tool used in the devices demonstrated here, namely optical switches, laser cavities, and Kerr frequency comb sources. Ring resonator basics are discussed in Section 2.4.

## 1.2 Organization of the dissertation

This dissertation first introduces relevant background on topics related to the three primary devices demonstrated here. Chapter 2 introduces integrated photonics, including electromagnetic waves, waveguides, microresonators, and nanofabrication. Chapter 3 describes laser operation, semiconductor lasers, and the derivation of the laser linewidth. Chapter 4 explains the field of nonlinear optics, frequency combs, and solitons. With the introductory background now covered, Chapter 5 presents two demonstrations of devices using multimode silicon waveguides to increase the bandwidth capacity of integrated optical networks. Next, Chapter 6 describes the design and demonstration of an integrated laser using a novel approach to achieve an extremely narrow linewidth. Chapter 7 presents a fully-integrated frequency comb source that finally enables low-power and portable operation.

CHAPTER 2  
INTEGRATED PHOTONICS

## 2.1 Fiat lux: Waves and light

Although light has always been central to our perception of the world, many of its properties were not scientifically understood until relatively recently. Ancient philosophers had determined the nature of light's reflection and refraction, but electromagnetic theory was needed to explain the propagation of light. In this section, we will first derive the wave equation for light.

The foundation of electromagnetism is based in Maxwell's equations, which describe the electric and magnetic field amplitudes in a medium:

$$\nabla \cdot \vec{D} = \rho \quad (2.1)$$

$$\nabla \cdot \vec{B} = 0 \quad (2.2)$$

$$\nabla \times \vec{E} = -\frac{\partial \vec{B}}{\partial t} \quad (2.3)$$

$$\nabla \times \vec{H} = \vec{J} + \frac{\partial \vec{D}}{\partial t} \quad (2.4)$$

where  $\vec{D} = \varepsilon \vec{E}$  is the electric displacement field,  $\vec{B} = \mu \vec{H}$  is the magnetic field,  $\varepsilon$  is the electric permittivity of the medium, and  $\mu$  is the magnetic permeability of the medium. In materials lacking sources, the charge density  $\rho$  and current density  $\vec{J}$  are zero. To reach the wave equation, we can first take the curl of Equation 2.3:

$$\nabla \times (\nabla \times \vec{E}) = \nabla \times -\frac{\partial \vec{B}}{\partial t} \quad (2.5)$$

$$= -\mu(\nabla \times \frac{\partial \vec{H}}{\partial t}) \quad (2.6)$$

The time derivative can be removed from the curl operation:

$$\nabla \times \nabla \times \vec{E} = -\mu \frac{\partial}{\partial t} (\nabla \times \vec{H}) \quad (2.7)$$

We can then substitute in the right side of Equation 2.4, assuming no current, to obtain

$$\nabla \times \nabla \times \vec{E} = -\mu \frac{\partial}{\partial t} (\frac{\partial \vec{D}}{\partial t}) \quad (2.8)$$

$$= -\mu\epsilon \frac{\partial^2 \vec{E}}{\partial t^2} \quad (2.9)$$

We can use the vector identity

$$\nabla \times \nabla \times \vec{A} = \nabla(\nabla \cdot \vec{A}) - \nabla^2 \vec{A} \quad (2.10)$$

to obtain

$$\nabla(\nabla \cdot \vec{E}) - \nabla^2 \vec{E} = -\mu\epsilon \frac{\partial^2 \vec{E}}{\partial t^2} \quad (2.11)$$

From Equation 2.1, we can deduce that  $\nabla \cdot \vec{E} = 0$ , assuming that  $\nabla\epsilon/\epsilon = 0$ . This leaves

$$0 - \nabla^2 \vec{E} = -\mu\epsilon \frac{\partial^2 \vec{E}}{\partial t^2} \quad (2.12)$$

$$\nabla^2 \vec{E} = \mu\epsilon \frac{\partial^2 \vec{E}}{\partial t^2} \quad (2.13)$$

This is the homogeneous wave equation, which takes the same form as the equation for mechanical waves. We can then deduce that the coefficient on the right side is  $1/v^2$ , where  $v$  is a velocity. In vacuum, the velocity then equals

$$v = \sqrt{1/\mu_0\epsilon_0} = 2.998 \times 10^8 \text{ m/s} \quad (2.14)$$

This velocity, Maxwell noticed in the 19<sup>th</sup> century, happened to match earlier estimates of the speed of the light. This result was a strong indication for Maxwell that light is an electromagnetic wave traveling at a velocity  $c$ . As waves, light can experience interference and diffraction. Unlike other waves, such as sound, light can propagate in vacuum. In materials with  $\epsilon$  or  $\mu$  greater than those of vacuum, light effectively travels slower than  $c$  by a factor  $n$ , the index of refraction:

$$v_p = \frac{c}{n} \quad (2.15)$$

$$n = \frac{\sqrt{\mu\epsilon}}{\sqrt{\mu_0\epsilon_0}} \quad (2.16)$$

In most materials,  $n$  falls in the range of 1 to 4. The index of refraction is useful for describing the reflection and refraction of light as it enters different materials. Similar to the impedance mismatch which causes reflections of voltages on electrical transmission lines, the reflection of light depends on the difference in  $n$  between the incident side ( $n_1$ ) and the second side ( $n_2$ ). We can momentarily picture light as rays rather than waves in order to aid explanation of some basic properties. The reflection and transmission of light, in power, at normal incidence is given by the Fresnel equations

$$R = \left| \frac{n_1 - n_2}{n_1 + n_2} \right|^2 \quad (2.17)$$

$$T = \left| \frac{2n_1}{n_1 + n_2} \right|^2 \quad (2.18)$$

This tells us that, for example, light entering glass ( $n \approx 1.5$ ) from air ( $n = 1$ ) reflects 4% of the incident power. However, we will see shortly that complete reflection using these indices is possible and will enable all of the applications described in the remaining chapters.

In addition to reflection, light bends at interfaces with different  $n$ . The phenomenon of refraction is described by Snell's Law:

$$n_1 \sin \theta_1 = n_2 \sin \theta_2 \quad (2.19)$$

where  $\theta_1$  and  $\theta_2$  are the incident and transmitted angles relative to the surface normal. If we solve for  $\theta_2$ , we obtain

$$\theta_2 = \sin^{-1} \left( \frac{n_1}{n_2} \sin \theta_1 \right) \quad (2.20)$$

We can notice that for  $\sin \theta_1 > n_2/n_1$  (the critical angle), the argument of  $\sin^{-1}$  is greater than unity, which implies that a phase shift must occur to satisfy Snell's Law [2]. In this case, the incident light ray is reflected at the same angle  $\theta_1$ , in a process called total internal reflection.

## 2.2 Waveguides

Total internal reflection means that if light is incident from a material with a higher index of refraction relative to the surrounding material, and the steepness of the angle relative to the interface is not too large, the light can be confined in the former. Such waveguides allow precise control of the path of light over long distances. Unlike free-space propagation of light as waves, which spread out due to diffraction, guided waves can maintain a determined shape as they propagate. This topic will be explored further in this section.

A planar slab waveguide is depicted in Figure 2.1. For  $n_1 > n_2$ , light that is input beyond the critical angle continually experiences total internal reflection in the waveguide. The waveguide can even bend, and if the critical angle

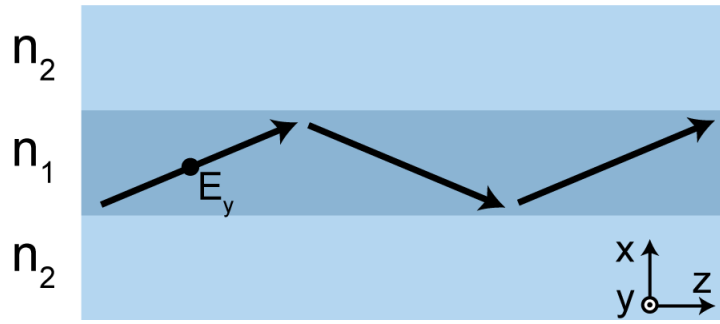


Figure 2.1: Diagram of a planar slab waveguide cross-sectional view. The electric field direction  $\hat{y}$  is out of the plane.

condition is still met, the light follows the shape of the waveguide.

By analyzing the incidence of a plane wave beyond the critical angle, it can be derived that the transmitted electric field amplitude  $\vec{E}_t$  is given by [2]

$$\vec{E}_t = \sqrt{T} E_0 e^{-\gamma x} e^{j\beta z} \hat{y} \quad (2.21)$$

where the propagation coefficient  $\beta$  and the decay factor  $\gamma$  are given by

$$\beta = k_0 n_1 \sin \theta_1 \quad (2.22)$$

$$\gamma = k_0 n_2 \sqrt{\frac{n_1^2}{n_2^2} \sin^2 \theta_1 - 1} \quad (2.23)$$

Equation 2.21 tells us that an electric field exists beyond the guiding core, even though the light is totally reflected. This is one place where the ray picture and wave description of light diverge. This evanescent field decays at positions farther from the waveguide, and it decays faster for larger index contrast. The evanescent field is crucial for coupling between parallel waveguides.

Note that the orientation of the light has been such that  $\vec{E}$  is in the  $\hat{y}$  direction (orthogonal to the material boundary surface normal); this is called a transverse electric (TE) field. For a transverse magnetic (TM) field,  $\vec{H}$  polarized along  $\hat{y}$ .

Although it would seem that *any* angle of incidence greater than the critical angle should result in light perpetually bouncing back and forth at that totally reflected angle, that is not the case. There are discrete *modes* supported by waveguides, rather than a continuum of states. The modes are eigenvalues of the waveguide, constituting an orthogonal, complete basis such that linear combinations of modes may be excited.

Inside the waveguide core ( $n_1$ ), the electric field is oscillatory. Outside of the core, in the cladding, the field is evanescent and decays exponentially. At the interfaces, Maxwell's equations require that the tangential components of  $\vec{E}$  and  $\vec{H}$  are continuous across the boundaries. Applying these conditions, it can be shown that the allowed TE modes in a waveguide must satisfy the characteristic equation

$$\tan(h\kappa_1) = \frac{2\gamma_2}{\kappa_1(1 - \frac{\gamma_2^2}{\kappa_1^2})} \quad (2.24)$$

where  $h$  is the thickness of the waveguide core (in the  $\hat{x}$ -direction),  $\gamma_2$  is the decay coefficient in the cladding (assuming symmetry), and  $\kappa_1$  is the transverse wavevector defined as

$$\kappa_1 = \sqrt{k_0^2 n_1^2 - \beta^2} \quad (2.25)$$

Equation 2.24 can be solved numerically by finding the intersection of the two sides of the equation. Each intersection corresponds to a mode described by its  $\kappa_1$  value, which in turn corresponds to a propagation coefficient  $\beta$  and an angle by Equation 2.22. The characteristic equation describes how a finite number of modes can be supported in a waveguide. One can immediately notice that large values of  $h$  result in a rapidly periodic tangent function, meaning more intersections between the two sides. This means that thicker waveguides support more modes. Additionally, for waveguides where  $n_1 \approx n_2$  (but still  $n_1 > n_2$ ),

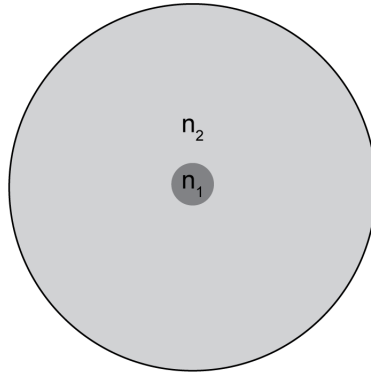


Figure 2.2: Cross-sectional view of a single-mode fiber. The index  $n_1$  of the core is slightly higher than the index  $n_2$  in the cladding.

$\gamma_2$  is very small, meaning that the mode decays slowly and extends far into the cladding. This also results in fewer modes being supported, because the light is weakly guided. Such low index contrast waveguides typically support a single mode (as is the case for optical fiber).

The characteristic equation tells us that only certain modes are supported for a given waveguide geometry, each associated with a different angle. The *shape* of the modes is also unique. The lowest-order TE mode, called  $TE_0$ , is roughly Gaussian, while the higher-order modes have increasing numbers of nodes in their oscillatory profiles. The higher-order modes are less confined in the core, so their evanescent fields are stronger. Because the light travels partially in  $n_1$  and partially in  $n_2$ , we can describe an *effective* index of refraction  $n_{\text{eff}}$  for each of the modes. The fundamental mode  $TE_0$  is the most confined, so its  $n_{\text{eff}}$  is closest to  $n_1$ . Higher-order modes have  $n_{\text{eff}}$  approaching closer and closer to  $n_2$ .

The most common waveguides have two-dimensional cross sections. A very important type of waveguide is an optical fiber, which is made from glass with a doped core. Optical fibers have achieved amazingly low loss on the order of

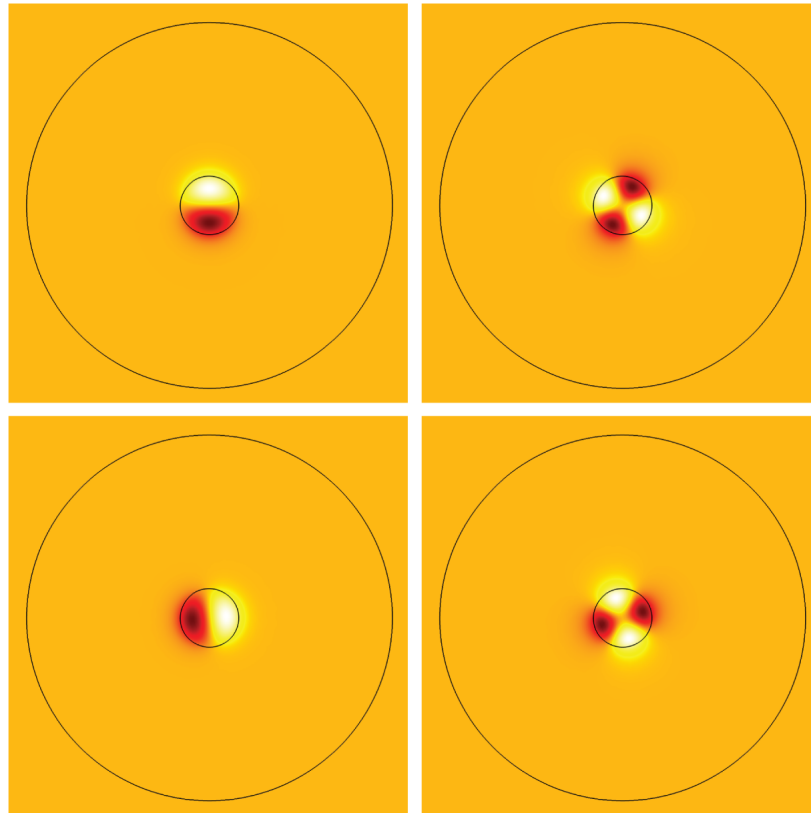


Figure 2.3: Mode profiles for various modes of a few-mode fiber (FMF).

0.2 dB/km, making them excellent for long-distance communications links. Figure 2.2 shows a step-index fiber waveguide cross section. Depending on the size of the core, the fiber may be either single-mode or multimode. Multimode fibers with core radius of e.g. 50  $\mu\text{m}$  are commonly used because they are tolerant to misalignment, with a few microns being only a fraction of the core size. The misalignment results in excitation of different modes, but this is not considered an issue because a large-area detector measures the total power without regard to modes. The cost of multimode fiber systems is typically cheaper than single mode for this reason. However, multimode fiber is limited in data rate and distance due to modal dispersion. Different modes travel at varying velocities corresponding to their  $n_{\text{eff}}$ , so high-speed data encoded on the light can become

blurred after some distance. In single mode fiber, the core is small enough that just a single mode is supported (and two polarizations). The lack of modal dispersion allows for high data rate signals, but the smaller size makes alignment more critical. There are also few-mode fibers (Figure 2.3) emerging for multiplexing applications (see Chapter 5).

Integrated waveguides typically have rectangular cross sections. The eigenmodes of these waveguides are found in essentially the same manner as the planar slab waveguides described above. However, because of the complexity of the additional dimension, the modes are solved here using finite element modeling software (COMSOL). Figure 2.4 shows a TE mode for a common silicon

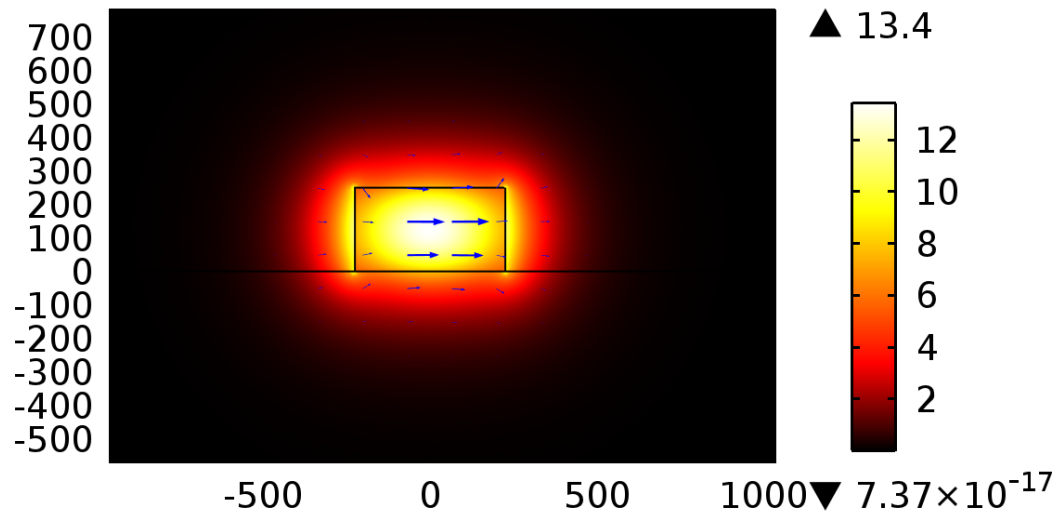


Figure 2.4: Cross-sectional profile for the TE<sub>0</sub> mode in a 250 x 450 nm silicon waveguide surrounded by SiO<sub>2</sub> at 1550 nm wavelength. Dimensions are in nm. Color scale units are V/m. The arrows show the magnitude and direction of  $E_x$ .

waveguide geometry. The mode profile has peak intensity in the center, while the field decays exponentially outside of the waveguide core. As waveguide

width increases, the fundamental mode becomes more confined in the waveguide (Figure 2.5). Wide waveguides may suffer less loss because they interact less with the potentially rough sidewalls of the waveguide, but the evanescent field decays faster, making them interact less with external features (such as other waveguides, or nearby particles for sensing). The narrower waveguides have highly delocalized modes that can have very large areas, making them useful for coupling to the large modes of a single mode fiber. The mode size is also relative to the wavelength of light (see Equation 2.23 for example). Figure 2.6 shows the same waveguide geometry with modes at different wavelengths. At 632 nm, the waveguide is multimode in both the width and height directions ( $TE_{11}$  is shown). At 1550 nm, the mode is single mode and mostly confined in the core, while at 3000 nm the mode is highly delocalized. Note that such large modes are typically lossy on SOI because the silicon substrate is separated from the mode by only 2-3  $\mu\text{m}$  of  $\text{SiO}_2$ .

Large waveguides support multiple modes simultaneously. Figure 2.7 shows three TE modes supported by a wide multimode silicon waveguide. Note that the modes are supported by the waveguide, but they are not necessarily excited. If the input of the waveguide is excited with the fundamental mode,

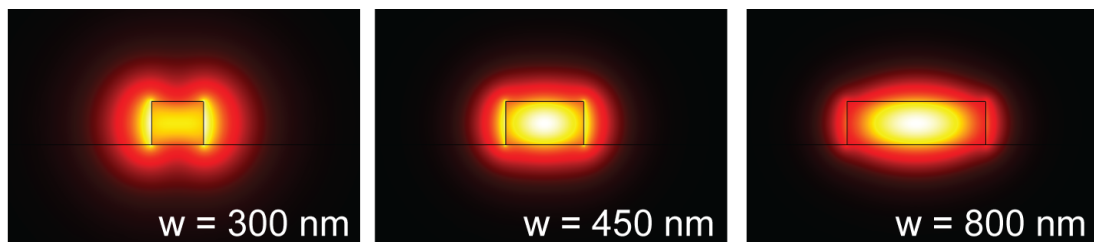


Figure 2.5: Cross-sectional profile for the  $TE_0$  mode in a 250 nm thick silicon waveguide surrounded by  $\text{SiO}_2$  at 1550 nm wavelength. The waveguide width is varied from 300 nm to 800 nm.

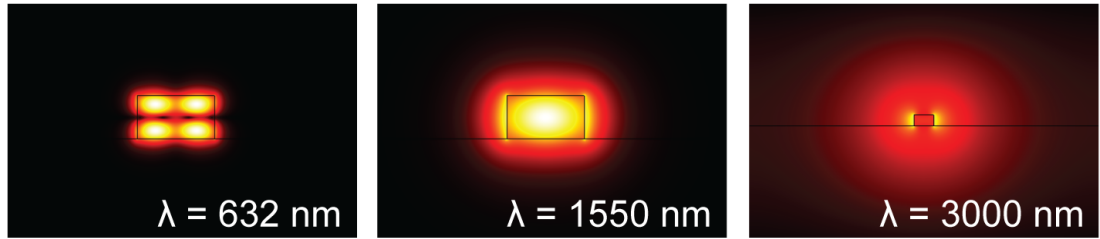


Figure 2.6: Cross-sectional profile for modes in a 250 x 450 nm silicon waveguide surrounded by SiO<sub>2</sub> at varying wavelengths. Note that at 3000 nm, a wider view is used to show the entire mode.

for example, then only that mode continues to propagate along the waveguide, because the other modes are orthogonal eigenmodes. Coupling may be induced, however, if the waveguide geometry changes, for example by bending the waveguide or suddenly changing its width. Chapter 5 discusses structures that precisely control mode excitation and propagation in waveguides.

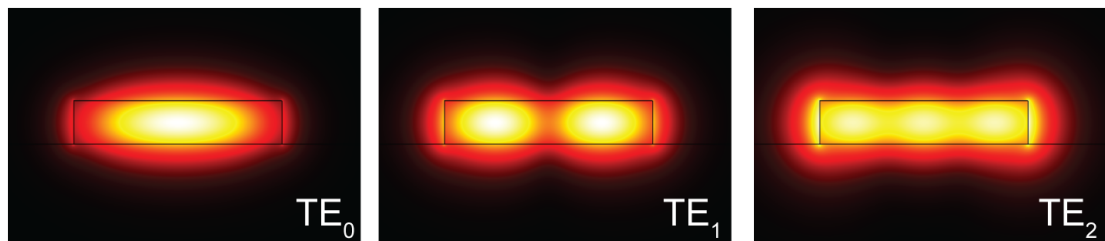


Figure 2.7: Cross-sectional profile for the first three TE modes in a 250 x 1200 nm silicon waveguide surrounded by SiO<sub>2</sub> at 1550 nm wavelength.

## 2.3 Coupled modes

Because integrated waveguides are lithographically defined, multiple waveguides can be positioned close together with excellent precision on the nanometer scale. This enables structures that rely on interactions between waveguides, such as directional couplers. A directional coupler consists of two waveguides in close proximity such that their evanescent fields overlap and light can couple between the waveguides.

Consider two parallel waveguides propagating in the  $z$ -direction. The electric field of each is

$$\vec{E}_{1(2)}(x, y, z) = E_{1(2)}(z) \vec{U}_{1(2)}(x, y) e^{-j\beta_{1(2)}z} \quad (2.26)$$

where  $\vec{U}_{1(2)}$  is the transverse mode shape in waveguide 1 or 2 and  $\beta_{1(2)}$  is the propagation constant for the uncoupled modes. If we assume weak coupling between the waveguides, we can find that the change in the amplitudes  $a_{1(2)}$  of the modes in each waveguide are given by

$$\frac{da_1}{dz} = -j\beta_1 a_1 - j\kappa_{12} a_2 \quad (2.27)$$

$$\frac{da_2}{dz} = -j\beta_2 a_2 - j\kappa_{21} a_1 \quad (2.28)$$

where  $\kappa_{12}$  and  $\kappa_{21}$  are the coupling constants between the waveguides [3]. The general solution for the amplitudes is then

$$a_1(z) = e^{-j\bar{\beta}z} (A_1 e^{jsz} + A_2 e^{-jsz}) \quad (2.29)$$

$$a_2(z) = e^{-j\bar{\beta}z} (B_1 e^{jsz} + B_2 e^{-jsz}) \quad (2.30)$$

where the  $A$  and  $B$  coefficients are amplitudes based on the initial conditions, and  $\bar{\beta}$  and  $s$  are propagation and coupling values given by

$$\bar{\beta} = \frac{\beta_1 + \beta_2}{2} \quad (2.31)$$

$$s = \sqrt{\left(\frac{\beta_1 - \beta_2}{2}\right)^2 + \kappa_{12}\kappa_{21}} \quad (2.32)$$

In the case where the waveguides are identical, i.e.  $\beta_1 = \beta_2$  and  $\kappa_{12} = \kappa_{21}$ , the coupled mode solution consists of sinusoidal coupling of light back and forth between the waveguides in the propagation direction. Figure 2.8 shows wave-

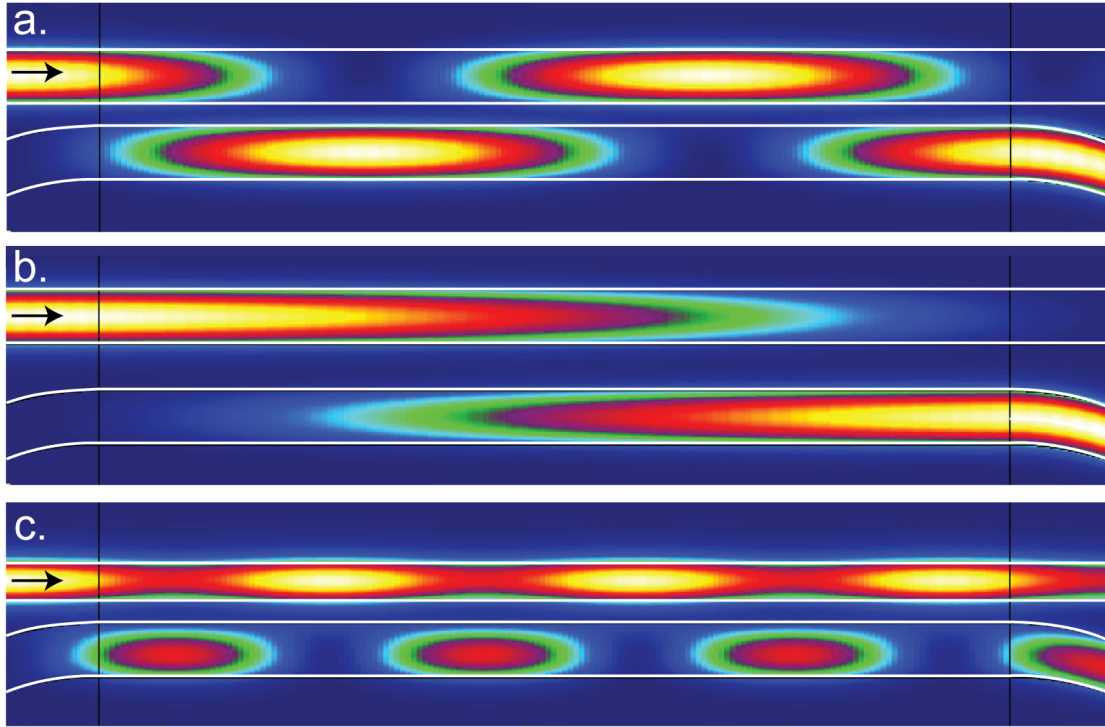


Figure 2.8: Top view of two coupled waveguides as light is injected to the upper waveguide propagating towards the right. (a) Light couples back and forth between the waveguides. (b) A larger coupling gap reduces the coupling rate. (c) The two waveguides are set to unequal widths, so light never fully couples between them.

guides in a directional coupler under various conditions. In Figure 2.8a, light is injected to the upper waveguide, while the lower waveguide bends closer in proximity. With the waveguides parallel, light couples back and forth according to Equations 2.29-2.30. By selecting the proper coupling length, the waveguides

can be separated once light has coupled from one waveguide to the other. In Figure 2.8b, the gap between the waveguides is increased, so the coupling rate is decreased. In Figure 2.8c, the upper waveguide is set to a narrower width than the lower waveguide, such that  $\beta_1 \neq \beta_2$ . The lack of phase matching means that light never fully couples to the lower waveguide.

Note that there is an alternate explanation for mode coupling in directional couplers. If both waveguides are considered together, rather than in isolation, they support certain "supermodes." Figure 2.9 shows that two waveguides in proximity support a symmetric mode and an anti-symmetric mode. The symmetric mode has a slightly higher  $n_{\text{eff}}$ , so they propagate at different velocities. Therefore, their propagation can be seen as interference (beating) between two modes, where the rate of beating is related to the difference in  $n_{\text{eff}}$ . The more closely spaced the two waveguides, the larger the difference in  $n_{\text{eff}}$  between the two modes. In the limiting case, the waveguides are very far apart with equal  $n_{\text{eff}}$ , so the coupling is zero.

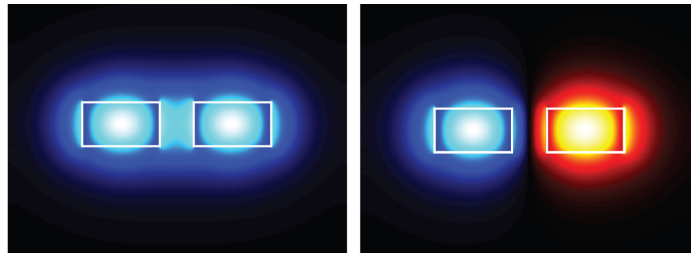


Figure 2.9: Cross sectional view of  $E_x$  for two coupled silicon waveguides.

## 2.4 Microresonators

Microresonators are among the most important tools enabled by silicon photonics. They provide greatly enhanced interactions between light and matter by increasing the intensity and interaction length of light while maintaining a compact size. They provide precise spectral features and enable high sensitivity and tunability. While some of these features are double-edged swords, microresonators offer performance that is often impossible by non-resonant approaches. The class of microresonators discussed here, microring resonators, have enabled small-footprint, low-power modulators in silicon photonics [4], as well as filters, switches [5], sensors [6], and cavities for parametric gain [7].

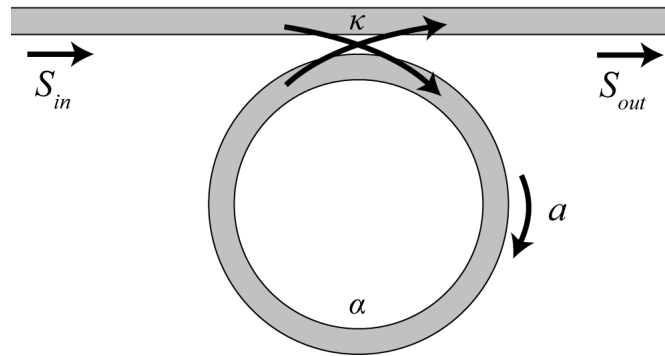


Figure 2.10: Diagram of a ring resonator, including the field in the bus waveguide  $S_{in}$ , the field in the ring  $a$ , the coupling between the two  $\kappa$ , the ring propagation loss  $\alpha$ , and the output field in the bus waveguide  $S_{out}$ .

A microring resonator is a waveguide that loops around to connect with itself, often in a circular shape. Light is coupled into the ring using a directional coupler, where the ring is often bending and the bus waveguide is often straight (Figure 2.10), but the coupling length is short enough that the two are approx-

imately phase matched. Consider an input field  $S_{\text{in}}$  to the bus waveguide couples to the ring resonator. The field  $a$  in the ring and the output field  $S_{\text{out}}$  are given by the rate equations [8]

$$\frac{da}{dt} = (j\omega_0 - 1/\tau_0 - 1/\tau_c)a + \kappa S_{\text{in}} \quad (2.33)$$

$$S_{\text{out}} = S_{\text{in}} - \kappa^* a \quad (2.34)$$

The coupling  $\kappa$  is related to the coupling time constant  $\tau_c$  by

$$|\kappa| = \sqrt{2/\tau_c} \quad (2.35)$$

and the resonator lifetime  $\tau_0$  is related to the loss  $\alpha$  by

$$\tau_0 = \frac{n_g}{\alpha c} \quad (2.36)$$

Here it is assumed that coupling to other modes is minimal.

Equation 2.33 has the frequency response

$$a(\omega) = \frac{\kappa}{j(\omega - \omega_0) + 1/\tau_0 + 1/\tau_c} S_{\text{in}}(\omega) \quad (2.37)$$

Therefore  $S_{\text{out}}$  is given by

$$S_{\text{out}}(\omega) = S_{\text{in}}(\omega) - \kappa^* a \quad (2.38)$$

$$= S_{\text{in}}(\omega) - \frac{\kappa\kappa^*}{j(\omega - \omega_0) + 1/\tau_0 + 1/\tau_c} S_{\text{in}}(\omega) \quad (2.39)$$

Finally the transmission amplitude past the waveguide is the ratio of output to input

$$T = \frac{S_{\text{out}}(\omega)}{S_{\text{in}}(\omega)} \quad (2.40)$$

$$= \frac{j(\omega - \omega_0) + 1/\tau_0 - 1/\tau_c}{j(\omega - \omega_0) + 1/\tau_0 + 1/\tau_c} \quad (2.41)$$

The resulting shape of the transmission power is Lorentzian (Figure 2.11). This

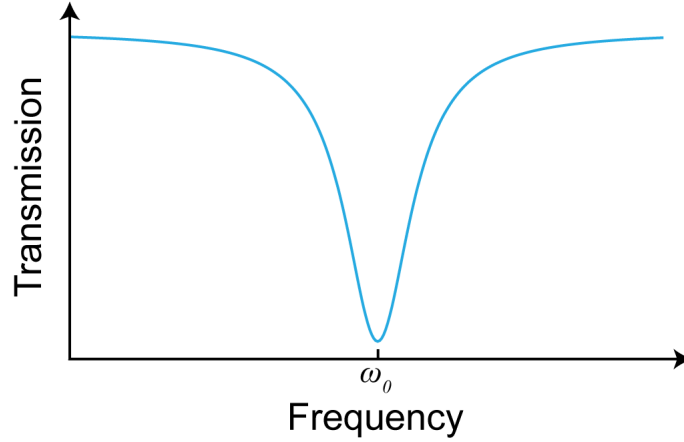


Figure 2.11: Spectral profile of transmission past ring resonator near  $\omega_0$ .

describes the steady state behavior of the ring. The frequency  $\omega_0$  is the resonance frequency of the ring. Being a resonator, the circumference of the ring  $L$  must equal an integer number of wavelengths

$$L = \frac{m\lambda}{n_{\text{eff}}} \quad (2.42)$$

where  $L$  is usually equal to  $2\pi R$ . Wavelengths satisfying this condition have resonances such as that in Figure 2.11. At these wavelengths, light coupled into the waveguide and light returning from a roundtrip interfere constructively in the ring, and light coupled back to the bus waveguide destructively interferes with the field in the bus waveguide. Therefore, transmission in the bus waveguide can significantly decrease on resonance. The remainder of the light eventually dissipates in the ring according to the propagation loss  $\alpha$ .

The spacing between resonances is the free-spectral range (FSR), given by

$$\text{FSR} = \frac{c}{n_g L} \quad (2.43)$$

The width of the resonance is related to the quality factor ( $Q$ ) of the ring. The intrinsic quality factor  $Q_0$  is equal to  $\omega_0 \tau_0 / 2$  and depends only on  $\alpha$ , rather than

the size of the resonator. Therefore measuring the  $Q_0$  of a resonance is a convenient way to measure small values of  $\alpha$ . We can also define a coupling quality factor  $Q_c = \omega_0\tau_c/2$  where strong coupling lowers  $Q_c$ . Finally, a loaded quality factor  $Q_L$  is defined

$$Q_L = \frac{1}{Q_0} + \frac{1}{Q_c} \quad (2.44)$$

$$= \frac{Q_0}{1 + \frac{Q_0}{Q_c}} \quad (2.45)$$

This corresponds to the actual full-width half-maximum of the resonance  $\Delta\omega = \omega_0/Q_L$ . When the ratio  $Q_0/Q_c$  is equal to unity, the ring is said to be critically coupled. This means that the light coupled into the ring balances exactly with the light lost [9]. Then,  $Q_L = Q_0/2$ . If the losses are high compared to the coupling, the ring is undercoupled, and the resonance does not reach zero transmission, and the resonance bandwidth narrows. If the coupling is larger than the losses, the ring is overcoupled, and again the resonance does not reach full extinction, but the resonance becomes broader.

One of the most exciting features of ring resonators is their ability to store energy. A basic metric of this ability is the finesse  $\mathcal{F}$ :

$$\mathcal{F} = \frac{\text{FSR}}{\Delta\nu_{1/2}} \quad (2.46)$$

where  $\Delta\nu_{1/2}$  is the full-width half-maximum resonance bandwidth in frequency. The highest finesse structures therefore must not only have low loss, but also small size. The field in the ring enhances the input field from the bus waveguide by a factor of  $(2/\pi)\mathcal{F}$ . The power in the ring can easily be over 1,000 times greater than the input waveguide power.

Consider now a second waveguide is coupled to the ring resonator (Figure 2.12) with coupling  $\kappa'$ . If we assume equal coupling constants for both the upper

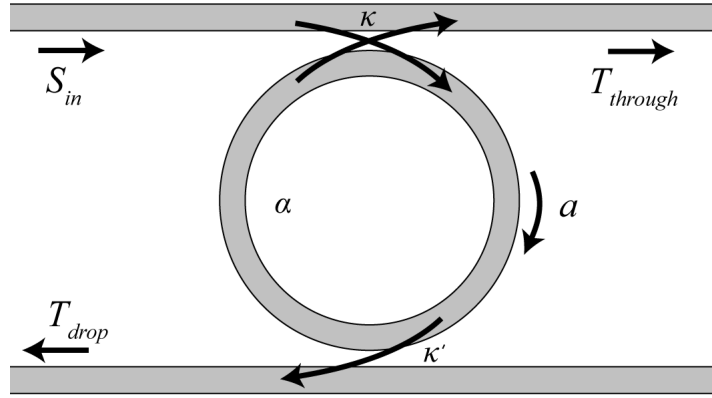


Figure 2.12: Diagram of a ring resonator including a waveguide drop port.

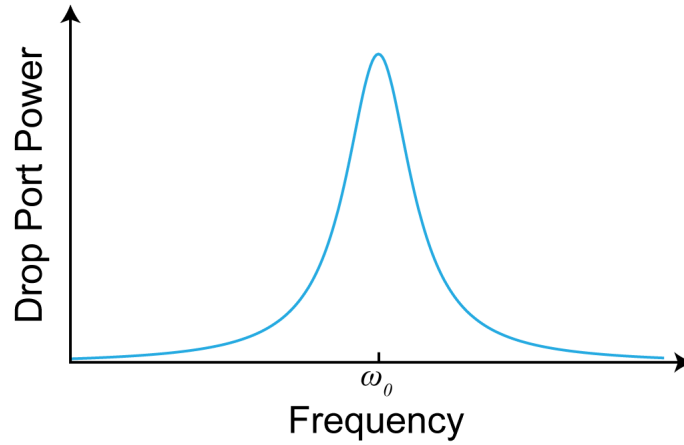


Figure 2.13: Spectral profile of drop port transmission near  $\omega_0$ .

(through) and lower (drop) ports, then the drop port transmission amplitude becomes [8]

$$T_{\text{drop}} = \frac{-2/Q_c}{j2\frac{\omega - \omega_0}{\omega_0} + \frac{1}{Q_0} + \frac{2}{Q_c}} \quad (2.47)$$

The power transmitted to the drop port is plotted in Figure 2.13. While the through port has a minimum in transmission on resonance, the drop port transmission is maximized. In fact, for strong coupling, nearly all of the light can be dropped by the ring on resonance. The critical coupling condition is now

modified to include  $\kappa'$ :

$$\kappa = \kappa' + \alpha \quad (2.48)$$

This means that the coupling at the through port must compensate for all losses in the ring, including coupling to the drop port.

Ring resonators in add-drop configuration are useful as spectral filters because they can drop light of a particular wavelength while other wavelengths experience high transmission to the through port. Accordingly, they are of great interest for wavelength-division multiplexing (WDM) in silicon photonics. Additionally, resonances can be tuned (shifted in frequency) through a number of effects, including thermo-optic tuning, carrier depletion and injection, and the Pockels effect in non-centrosymmetric materials (see Chapter 4). These effects change the index of refraction in the ring waveguide, however slightly, yet the enhanced sensitivity to change can cause large shifts in the resonance position  $\omega_0$ , even exceeding a full FSR. This makes rings useful for optical switching and modulation (see Chapter 5).

In our initial analysis of fields in a ring resonator (Equation 2.33), coupling to other modes was neglected. In some cases, there can be noticeable coupling between the clockwise mode excited by the input bus waveguide and the counterclockwise mode that may be excited through some coupling  $\mu$ . Including this coupling to the case of a ring resonator without a drop port, the fields are given

by

$$\frac{da_{cw}}{dt} = (j\omega_0 - \frac{1}{\tau_0} - \frac{1}{\tau_c})a_{cw} + j\mu a_{ccw} + \kappa S_{in} \quad (2.49)$$

$$\frac{da_{ccw}}{dt} = (j\omega_0 - \frac{1}{\tau_0} - \frac{1}{\tau_c})a_{ccw} + j\mu^* a_{cw} \quad (2.50)$$

$$S_{out} = S_{in} - \kappa^* a_{cw} \quad (2.51)$$

$$S_{ref} = -\kappa^* a_{ccw} \quad (2.52)$$

The clockwise (CW) and counterclockwise (CCW) modes are traveling waves, but the apparent field distribution in the ring consists of two standing waves. The two standing wave modes can have different quality factors, but here we will consider the common case where they are approximately equal. Because two coupled modes are circulating in the same resonator with the same propagation parameters, they are degenerate, and we expect that the resonance should split (like splitting of atomic energy levels). We can define an associated splitting quality factor  $Q_{split}$  equal to  $\omega_0/(2|\mu|)$ . The transmission ( $T = S_{out}/S_{in}$ ) and reflection ( $R = S_{ref}/S_{in}$ ) amplitudes are given by [8]

$$T = 1 - \frac{(j4\omega_R + \frac{2}{Q_L})/Q_c}{[j(2\omega_R - \frac{1}{Q_{split}}) + \frac{1}{Q_L}][j(2\omega_R + \frac{1}{Q_{split}}) + \frac{1}{Q_L}]} \quad (2.53)$$

$$R = -\frac{j2/(Q_{split}Q_c)}{[j(2\omega_R - \frac{1}{Q_{split}}) + \frac{1}{Q_L}][j(2\omega_R + \frac{1}{Q_{split}}) + \frac{1}{Q_L}]} \quad (2.54)$$

$$\omega_R \equiv \frac{\omega - \omega_0}{\omega_0} \quad (2.55)$$

Depending on the coupling between the counter-propagating modes and the  $Q_L$  of the ring, the splitting may or may not be apparent. Typically high  $Q_L$  is needed to see a noticeable splitting. Figure 2.14 plots the transmission and reflection for a ring with  $Q_L = 4 \times 10^6$ . The reflection on resonance is particularly strong. The coupling condition can be used to vary the reflection (Figure

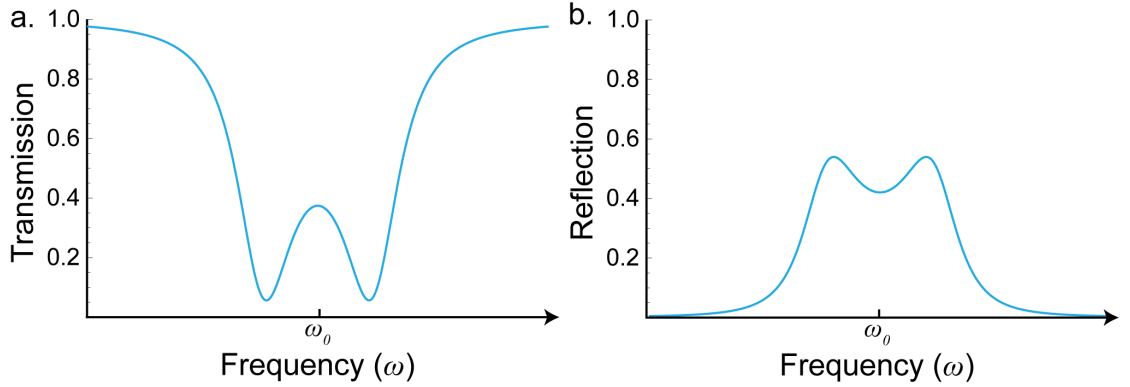


Figure 2.14: (a) Through port transmission (power) of ring resonator with coupling between CW and CCW modes. The degenerate splitting corresponds to  $\mu = 2.5 \times 10^8 \text{ rad s}^{-1}$ .  $Q_0 = 1.5 \times 10^7$  and  $Q_L = 4 \times 10^6$ . The x-axis range is  $\omega_0 \pm 1 \times 10^9 \text{ rad s}^{-1}$ . (b) Reflected power in bus waveguide due to CCW mode, assuming the same conditions as (a).

2.15). As coupling  $\kappa$  between the ring and the bus waveguide increases away from undercoupling, the reflection increases and the mode splitting becomes less apparent (Figure 2.15a). If coupling is increased further, the reflection decreases and broadens (Figure 2.15b). In general, lower loss (higher  $Q_0$ ) results in stronger reflection for a fixed  $\mu$ . However, in practical application,  $\mu$  likely has some correlation with  $Q_0$ . Experiments in microresonators have observed reflections on the order of 80% [10]. While such mode splitting and reflection is sometimes considered undesirable, a useful purpose is proposed in Chapter 6.

## 2.5 Carrier depletion modulators

Modulators are critical for digital and analog optical communications. An electro-optic modulator converts a changing electric field (or voltage) into a change in optical phase or transmission, typically at very fast speeds (i.e. GHz).

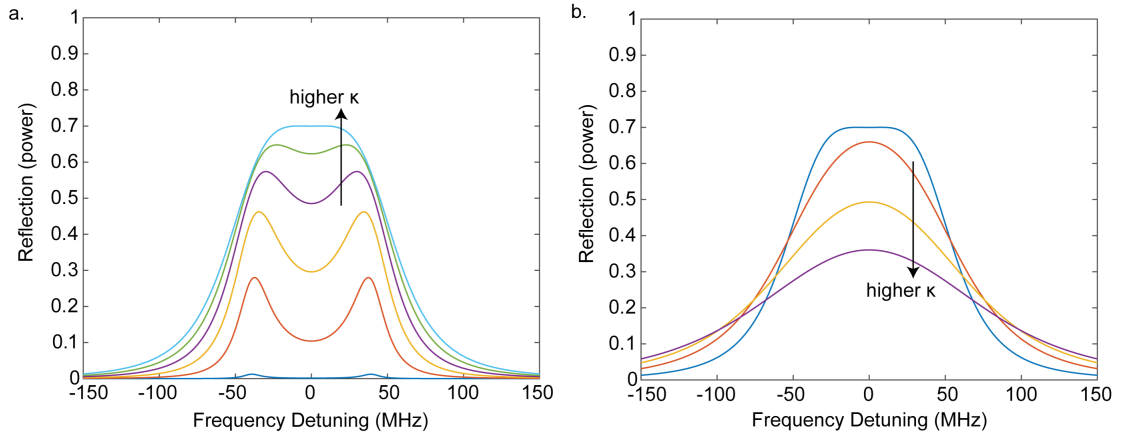


Figure 2.15: (a) Calculated reflected power for varying coupling values ( $\kappa$ ), from undercoupling to near critical coupling. The coupling due to backscattering  $\mu = 2.5 \times 10^8 \text{ rad s}^{-1}$  and  $Q_0 = 1.5 \times 10^7$  are fixed. (b) Calculated reflected power for varying coupling values, from near critical coupling to overcoupling, assuming the same conditions as (a).

A typical modulation approach in silicon photonics is based on the free-carrier plasma dispersion effect in silicon, where charge carrier density is modulated to change the refractive index. The exact structure considered here is a pn junction in silicon operating in reverse bias.

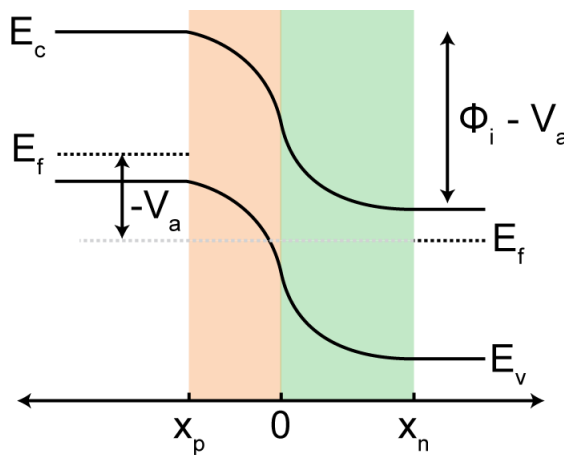


Figure 2.16: Band diagram of a silicon pn junction operating in reverse bias.

Consider a junction formed in silicon by introducing impurities (donors on the n-type side, and acceptors on the p-type side). In addition to the band bending  $\phi_i$  resulting from the difference in Fermi energies  $E_f$  on the two sides, consider that a reverse bias voltage  $V_a$  is applied. Figure 2.16 shows the band diagram of such a junction. The width of the depletion region  $x_d$  depends mainly on the donor and acceptor concentrations  $N_d$  and  $N_a$ :

$$x_d = x_p + x_n = \sqrt{\frac{2\epsilon(\phi_i - V_a)}{q} \left( \frac{1}{N_a} + \frac{1}{N_d} \right)} \quad (2.56)$$

where  $\epsilon$  is the permittivity of silicon and  $q$  is the electronic charge. By adjusting the applied voltage  $V_a$ , the width of the depletion region can be tuned.

The depletion region on the n-type side has a buildup of positive ions, while the p-type side has negative ions. These ions, like injected carriers, modify the index and absorption of silicon according to [11]

$$\Delta n = -(8.8 \times 10^{-22} \Delta N + 8.5 \times 10^{-18} \Delta P^{0.8}) \quad (2.57)$$

$$\Delta \alpha = 8.5 \times 10^{-18} \Delta N + 6.0 \times 10^{-18} \Delta P \quad (2.58)$$

where  $\Delta N$  and  $\Delta P$  are the electron and hole densities, respectively. Therefore, it is apparent that modulating the depletion width using a voltage modulation can result in a modulation of  $n$  [12].

When the depletion region is formed across a silicon waveguide's cross-section, the optical mode interacts strongly with the modulation in index, and the result is a phase shift. The phase shift can be useful in itself, or such a waveguide can be placed in a Mach-Zehnder interferometer (MZI) to translate the phase modulation to amplitude modulation. However, the loss introduced by the pn junction may become too large if the doping concentration is too high, resulting in a trade-off between index shift and loss. In Section 5.2, a pn junc-

tion is formed across a waveguide in a ring resonator so that the index shift is amplified by the sensitivity of the microresonator structure. Such compact microring modulators are desirable as optical data transmission moves to shorter distances and requires higher energy efficiency.

## 2.6 Integrated photonic fabrication

Silicon photonics utilizes many of the same wafer processing steps used in electronic integrated circuit fabrication. However, silicon on insulator (SOI) wafers are typically used. SOI wafers begin with crystalline silicon wafers, which are inexpensive and plentiful. Silicon wafers are typically cut from large boules of highly pure silicon. The wafers may range from 3 inches to 12 inches in diameter, with a thickness greater than 500  $\mu\text{m}$ . When silicon is brought to a high temperature in a furnace in the presence of oxygen, the surface thermally oxidizes, forming  $\text{SiO}_2$ . Ions can also be implanted to a controlled depth in the silicon wafer [13]. A wafer that has undergone these two steps can be bonded to another silicon wafer, and temperature treatment can induce splitting at the ion implantation depth. In this way, two layers of crystalline silicon are achieved on a single wafer (see first panel of Figure 2.17). The upper layer will eventually form the silicon waveguide, while the  $\text{SiO}_2$  serves as a cladding to separate the waveguide from the bottom silicon substrate.

The SOI wafer can be processed to form silicon waveguides by following several basic steps (Figure 2.17). First, a viscous material called photoresist is placed on the wafer, and when the wafer is spun at a high speed, the photoresist spreads out to form a uniform film of precisely controlled thickness. Pho-

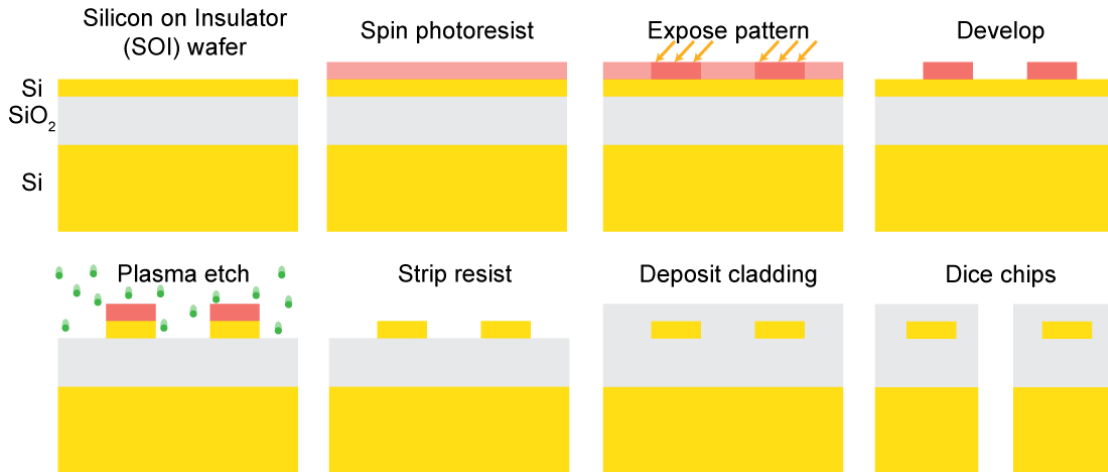


Figure 2.17: Basic fabrication steps for patterning silicon waveguides.

Photoresist can be either negative or positive tone. Negative photoresist molecules may crosslink when exposed to light of a particular wavelength, typically ultraviolet (UV) light. Unexposed negative photoresist can be removed in a solution of liquid developer. Positive photoresist has the opposite reaction; only the *exposed* areas are removed in the developer. Besides UV photoresists, there are also electron-beam (e-beam) resists which are exposed by a beam of electrons. E-beam uses the same technology as a scanning electron microscope (SEM) and can often reach finer resolutions than photolithography, but it is much slower. The beam exposes patterns on a wafer in serial fashion, while photolithography masks used in steppers or scanners can expose entire wafers in less than a minute.

Once a pattern is transferred into the photoresist (Figure 2.17), this pattern can be transferred to the silicon by etching. A plasma etcher allows anisotropic etching downwards from the photoresist mask. A typical etch chemistry involves SF<sub>6</sub> etching Si to form SiF<sub>4</sub>. Common considerations during etching are the selectivity of etching the silicon to removing the resist, the sidewall angle

of the etching (how anisotropic it is), and the roughness of the etch. Etch rates may vary across large wafers, so some devices have different dimensions even if designed to be identical. Therefore, design of integrated devices must take fabrication variations into account. Waveguides are sometimes etched in multiple steps to allow either fully etched or partially etched waveguides.

After the waveguides are defined, there may be additional processing steps specific to the needs of the device. A common series of steps for electro-optic devices involves ion implantation of dopants to form diodes, resistors, and contacts. For some applications, unclad devices are needed, but often a layer of  $\text{SiO}_2$  is deposited using e.g. plasma-enhanced chemical vapor deposition (PECVD) to clad the waveguides. At this point, it may be necessary to etch vias down to the silicon and fill them with metal. Multiple layers of metal wires may be included. Once all of this processing is completed, the wafer is diced into individual chips which can then be packaged.

## CHAPTER 3

### INTEGRATED LASERS

The laser is possibly the most important innovation of the 20<sup>th</sup> century. It has enabled communications systems, medical products, high-tech manufacturing, and scientific discoveries. In this chapter we will explain how lasers function and relevant considerations for designing integrated lasers.

### 3.1 Electromagnetic radiation

Most sources of light, such as the Sun or incandescent light bulbs, emit electromagnetic radiation according to their temperature as described by Planck's law:

$$\rho(\nu) = \frac{8\pi\nu^2}{c^3} \frac{h\nu}{e^{h\nu/kT} - 1} \quad (3.1)$$

where  $\rho$  is the energy density of light emitted,  $\nu$  is the frequency of light,  $h$  is Planck's constant, and  $k$  is Boltzmann's constant. As shown in Figure 3.1, this emission is very broad, covering a large range of wavelengths. A blackbody emitter with a temperature of 3,400 K is needed to have a peak near 1.5  $\mu\text{m}$ . Clearly, a more efficient and precise light source is desirable for many applications.

### 3.2 Lasers

Consider an atom with two energy levels,  $E_1$  and  $E_2$ , with  $E_1 < E_2$ . When the atom is in the higher level  $E_2$ , it can decay to  $E_1$  spontaneously and release a

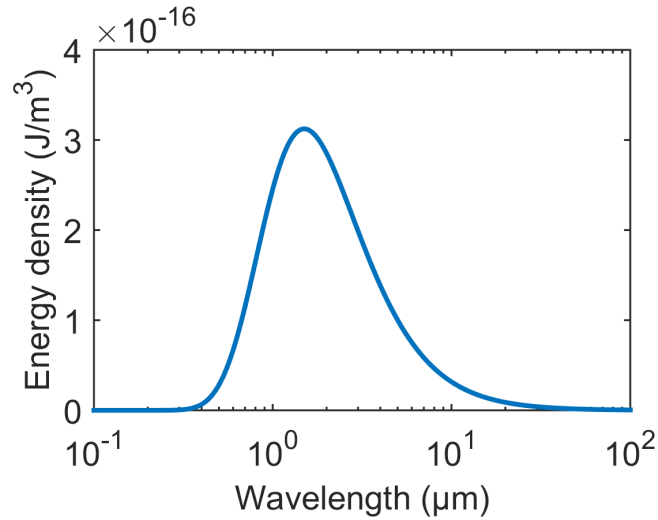


Figure 3.1: Energy density of blackbody radiation at 3,400 K according to Planck's law. The peak energy density occurs at 1.5  $\mu\text{m}$ .

photon with an energy corresponding to the energy difference

$$E = h\nu \quad (3.2)$$

$$= E_2 - E_1 \quad (3.3)$$

This stochastic process is called *spontaneous emission*. The atom can alternately decay from  $E_2$  to  $E_1$  without emitting a photon. In this process of non-radiative decay, the energy may convert to heat for example [14]. There is another potential fate of the excited state  $E_2$ : *stimulated emission*. The term *laser* began as the acronym "light amplification by stimulated emission of radiation." The process of stimulated emission is chiefly responsible for the unique properties of laser light. In this process, an incident photon with energy matching that of Equation 3.2 may stimulate the atom to decay to  $E_1$  and, in the process, to emit a photon in phase with the incident light and in the same direction. This offers the possibility of additional photons joining the pack through stimulated emission, resulting in a strong beam of coherent light.

Another important process may occur when the atom is initially in the ground state  $E_1$ . An incident photon may be absorbed and excite the atom to  $E_2$  during *stimulated absorption*. This process, however, dampens our hopes for obtaining lasing. The rate equations for these processes results in the condition that  $N_2$ , the number atoms in  $E_2$ , must satisfy the threshold condition [14]

$$N_2 > g_2 N_1 / g_1 \quad (3.4)$$

where  $g_1$  and  $g_2$  are the degeneracies of the two states, respectively. The threshold condition in Equation 3.4 requires a population inversion. This essentially says that if more atoms are in the excited state, then stimulated emission is more likely than absorption when an incident photon flux arrives. However, the rates of stimulated emission and absorption between two states are equal. At thermal equilibrium, these two processes counteract, and population inversion is not possible.

The solution to achieving net amplification through stimulated emission uses more than two levels. In a three-level laser, atoms are excited from the ground state ( $E_1$ ) to  $E_3$  by a pump (usually originating from an electric current or another laser). The atomic or molecular structure is such that  $E_3$  quickly decays to  $E_2$ . The transition from  $E_2$  to  $E_1$  then constitutes the stimulated emission process of the laser. The atoms in  $E_1$  should be rapidly pumped to  $E_3$  to minimize stimulated absorption and to maintain the population inversion. Four-level lasers often provide an easier route to lasing because the lower lasing level can rapidly decay to an even lower level, rather than relying on pumping.

The above process describes how optical amplification is obtained. If an amplifier is placed in a resonant cavity, then the feedback increases the intracavity optical intensity, which promotes further stimulated emission. A basic design of

a laser cavity is a gain material placed between two mirrors, one reflecting 100% and the other with a lower reflection. The second mirror serves as the output coupler and helps to determine the output power of the laser. Being an optical cavity, only certain longitudinal modes (wavelengths) are supported due to the boundary conditions of the cavity. Only the modes overlapping with the gain material's spectral bandwidth may lase. Multiple lasing modes would typically be undesirable because they must each compete for gain, resulting in noise. If the gain is broad, intracavity filters may be used to select a single mode to lase, and tuning these filters can allow tunable lasing. Note that the mode spacing (FSR) is inversely proportional to the cavity length (according to Equation 2.43), so long laser cavities, such as fiber lasers, can have closely-spaced modes that are more challenging to filter. The number of transverse modes can be restricted by using a single-mode waveguide in the cavity.

If the cavity losses, including the transmission of the output coupler mirror, are not too large, the intracavity power  $I$  eventually reaches a level ( $I_{sat}$ ) where the gain  $g$  saturates

$$g = \frac{g_0}{1 + \frac{I}{I_{sat}}} \quad (3.5)$$

where  $g_0$  is the unsaturated gain coefficient. When the output of the laser reaches a steady-state, it is called a continuous wave laser. Lasers may be arranged to emit time-dependent output, as well. Such pulsed lasers will be discussed in the following section.

### 3.3 Pulsed and mode-locked lasers

A common method of creating pulsed lasers is called Q-switching. This technique can result in nanosecond length pulses with megawatt peak power (the power averaged over the period is much lower than the peak power) [14]. In Q-switching, the cavity loss is periodically changed to control the population inversion. The loss may be modulated using active techniques such as acousto-optic modulators, or by passive techniques using saturable absorbers with intensity-dependent loss.

Another approach for achieving pulsed laser output is mode-locking. If a laser is oscillating on a large number of longitudinal modes evenly spaced in frequency by the FSR, the output power varies periodically in time. Note that a Fourier transform of discrete frequencies corresponds to a set of discretely timed pulses. However, because the relative phases of the modes are typically random, the output appears mostly random as well. If there is a definite relation between the phases of the  $N$  modes, though, then the output is a single pulse at a period of  $\tau_p = 1/\Delta\nu$ . The pulse duration  $\Delta\tau_p$  is given by the total bandwidth of the oscillations,  $1/(N\Delta\nu) = 1/\Delta\nu_L$ . Because the pulse duration depends mainly on the gain bandwidth, many mode-locked lasers have demonstrated fs-length pulses. Additionally, the peak power is given by  $N^2E_0^2$  rather than the average power of  $NE_0^2$  from a non-mode-locked laser with the same number of oscillating modes and electric field amplitude  $E_0$ .

Like Q-switching, mode-locking can be achieved actively or passively. Active amplitude modulation, for example, can be used at the frequency  $\Delta\nu$  so that modulation side-bands coincide with adjacent lasing modes. In this way, the

fields of the oscillating modes become coupled, giving rise to a locked phase relationship between them. Passive mode-locking can be achieved using a suitably fast saturable absorber. Because of the random initial phase relationship between modes, there are certain peaks naturally present in the output in time. These pulses experience lower loss from the saturable absorber, so they grow faster and the survival of a single, high-intensity pulse results in mode-locking. A similar passive mode-locking approach uses a Kerr lens (see Chapter 4) to create an intensity-dependent transmission. Because the speed of this nonlinear optical effect is extremely fast, it has been used to generate some of the shortest mode-locked pulses [14].

### **3.4 Semiconductor lasers**

Semiconductor lasers are based on the same basic components as gas and solid-state lasers: a resonant cavity, a gain medium, and often spectral filters. However, semiconductor lasers are easily electrically pumped, making them much more convenient to use in many applications, from optical communications to medical imaging and lidar (laser ranging). The lifetime of semiconductor lasers can be hundreds of years, as compared to thousands of hours for flash-lamp pumping [3]. Most importantly, semiconductor lasers can be fabricated at wafer-scale, allowing the production of large quantities of inexpensive, compact lasers.

The materials used to make semiconductor lasers form crystals with covalent bonds. The bonding between many unit cells of the crystal results in splitting of their energy levels into bands, specifically the valence band and conduction

band. At 0 K, the conduction band is empty, while at higher temperatures some electrons are promoted to the conduction band, leaving holes in the valence band, according to a Fermi-Dirac distribution. Electrons may also be excited to the conduction band through pumping with an electric current. With electrons in the conduction band, an incident photon flux stimulates electron-hole pairs to recombine, simultaneously emitting additional photons. In addition to stimulated emission, photons may be absorbed by the semiconductor, boosting electrons to the conduction band and leaving holes in the valence band. Electrons in the conduction band may also spontaneously recombine with holes to emit photons. This process is used in light-emitting diodes (LEDs), but is undesirable in lasers. Additionally, nonradiative recombination of electron-hole pairs may result in heat generation rather than emission of photons.

The photon emitted corresponds to the difference in energy levels between the initial and final states of the electron as it moves from the conduction band to the valence band. The momentum  $\hbar k$  of the electron in the conduction band must closely correspond to the  $k$ -vector of an available state in the valence band, otherwise additional momentum is needed. Unfortunately, silicon has an indirect bandgap and has not been shown to allow efficient stimulated emission. Instead, the common materials used for semiconductor lasers include those with direct bandgaps, including III-V compounds such as indium phosphide and gallium arsenide. The material bandgap can be adjusted using alloys of these materials, allowing selection of the wavelength of light emitted, commonly in the range 650 nm - 1.55  $\mu\text{m}$ .

A common structure forming a semiconductor laser is a double-heterostructure  $p$ - $i$ - $n$  diode (Figure 3.2). When operated in forward bias, the

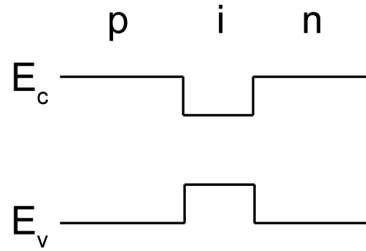


Figure 3.2: Band diagram of a double-heterostructure.

diode injects electrons and holes into a potential well in the *i*-region. Because of this well, it can be expected that all carriers recombine here. Additionally, the reduced bandgap and higher index of refraction in the potential well conveniently forms a waveguide. Such a structure can be fabricated such that the waveguide is terminated at the facets of the cleaved chip, where strong Fresnel reflections form a Fabry-Perot cavity for the laser. Another approach uses distributed Bragg reflector (DBR) mirrors composed of periodic index variations to allow greater mode selectivity than Fabry-Perot lasers. The DBR laser wavelength may also be tuned by applying an electric current to change the refractive index, effectively modifying the grating period. Similar to DBR lasers, distributed feedback (DFB) lasers use gratings to periodically vary the index, but the grating continues for the length of the gain section, rather than solely at the boundaries of the cavity.

### 3.5 Laser linewidth

Lasers emit monochromatic, coherent light, but their spectral purity has limitations. Due to spontaneous emission, photons that are not coherent with those originating from stimulated emission are periodically emitted. Spontaneous

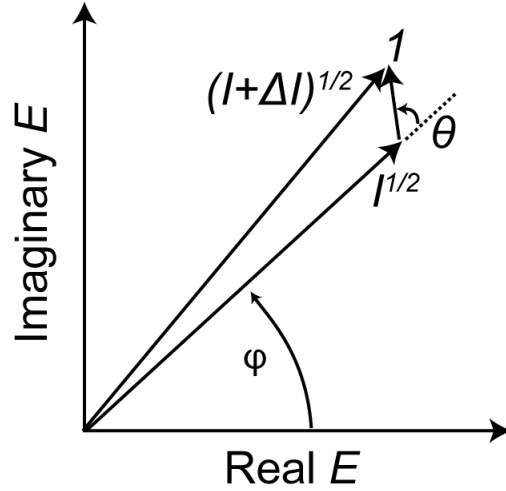


Figure 3.3: Intensity of optical field  $E$  influenced by spontaneous emission with a random phase.

emission adds noise to the phase of the output field, which in turn corresponds to frequency noise. The laser linewidth is a measure of this frequency noise. In semiconductor lasers, for example, linewidths are typically greater than 1 MHz.

For many applications, the laser linewidth is a critical parameter. In optical communications, an overly broad linewidth can limit the modulation formats and data rate used [15]. For coherent lidar, narrow linewidths enable long distance ranging. Additionally, sensors monitoring small phase changes require narrow linewidth lasers. In this section, the derivation of the theoretical linewidth is given, and several techniques for achieving narrow linewidths are discussed.

In lasers, spontaneous emission adds random phase contributions to a background of coherent emission. The lasing field  $E$  is given by

$$E = \sqrt{I}e^{i\phi} \quad (3.6)$$

where the average intensity  $I$  is also the average number of photons in the cav-

ity [16]. A spontaneous emission event contributes a unit magnitude perturbation at a random phase  $\phi + \theta$  (Figure 3.3). After  $N$  spontaneous emission events, the phase fluctuation is

$$\Delta\phi = \sum_{i=1}^N \sqrt{I}(\sin \theta - \cos \theta) \quad (3.7)$$

The average phase fluctuation  $\langle \Delta\phi^2 \rangle$  then becomes

$$\langle \Delta\phi^2 \rangle = \frac{N}{2I} = \frac{R_{sp}t}{2I} \quad (3.8)$$

where  $R_{sp}$  is the spontaneous emission rate, and  $t$  is the time period. The relative rates of spontaneous and stimulated emission,  $R_{sp}$  and  $R_{st}$ , are related by

$$\frac{R_{sp}}{R_{st}} = \frac{1}{I} \quad (3.9)$$

which describes how many photons contribute to the relevant mode. Next, the power  $P$  is described by the intensity, photon energy, and lifetime:

$$P = \frac{I}{\tau_c} h\nu \quad (3.10)$$

where the cavity lifetime  $\tau_c$  relates to the cavity bandwidth  $\Delta\nu_c$  by

$$\Delta\nu_c = \frac{1}{2\pi\tau_c} \quad (3.11)$$

Finally, if we use the knowledge that the power spectrum is Lorentzian, the full width half maximum (linewidth) is given by

$$\Delta\nu = \frac{\pi h\nu(\Delta\nu_c)^2}{P} \quad (3.12)$$

Equation 3.12 is the Schawlow-Townes linewidth including Lax's correction [16]. This equation describes the quantum limit for a laser's linewidth; the laser does not necessarily have this linewidth, as the phase noise may be affected by other factors, such as thermal fluctuations. In semiconductor lasers,

$\tau_c$  is typically short due to the compact size and higher losses of diode lasers. Therefore, the Schawlow-Townes linewidth is much larger in these lasers.

An additional effect broadens the linewidth even further in semiconductor lasers. After a spontaneous emission event, the change in carrier density changes the gain, which is related to the imaginary part of the refractive index  $n''$ . The change in carrier density also affects the real part of the refractive index  $n'$ , which results in another phase change. A factor  $\alpha$  is defined as the ratio of these changes:

$$\alpha = \frac{\Delta n'}{\Delta n''} \quad (3.13)$$

The typical value for  $\alpha$  is approximately 5. It has been shown that the coupling between phase and intensity fluctuations broadens the laser linewidth by  $1 + \alpha^2$  [16]. This can mean an increase of approximately 50 times the previous Schawlow-Townes linewidth. Equation 3.12 now becomes

$$\Delta\nu = \frac{\pi h\nu n_{sp}(\Delta\nu_c)^2(1 + \alpha^2)}{P} \quad (3.14)$$

where the spontaneous emission factor  $n_{sp} \approx 2.5$ . This equation will be used in Chapter 6 to analyze semiconductor laser linewidths.

Now several factors that allow linewidth reduction are discussed. They concern using extensions to the laser cavity beyond the semiconductor portion in order to moderate the aforementioned limitations resulting from spontaneous emission in the semiconductor. Consider a laser cavity that includes a passive section in addition to the semiconductor gain section (Figure 3.4). A photon in this cavity spends a portion of time per roundtrip in the semiconductor section and a portion of time in the passive section, with the ratio being  $\nu_{g0}L_1/\nu_{g1}L_0$  [1]. As we know from Equation 3.8, the spontaneous emission rate is proportional to  $I$ , the square of the field in the semiconductor. By including the new reduction

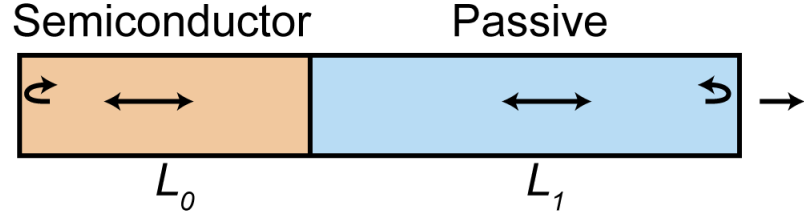


Figure 3.4: Diagram of an extended cavity laser, including a semiconductor-based gain section of length  $L_0$ , and a passive section of length  $L_1$ .

factor accounting for the fraction of the field in the passive section, the linewidth is then reduced to

$$\Delta\nu = \frac{\Delta\nu_0}{\left(1 + \frac{\nu_{g0}L_1}{\nu_{g1}L_0}\right)^2} \quad (3.15)$$

Therefore, by including a longer passive section, significant linewidth reduction is possible. However, this may complicate the principle of monolithic fabrication of the semiconductor and increase the size of the laser from a that of a chip to that of a free-space cavity. Note that here we assume no reflection at the interface between the two sections. If a resonator is formed in the passive section, though, then the additional roundtrips further increase the proportion of the photon field in the passive section.

Consider a single-section Fabry-Perot laser of length  $L$ . In order for lasing to occur in a cavity at steady state, the gain  $g$  must equal the loss. The frequency of lasing must additionally satisfy the condition for roundtrip phase

$$2kL = \frac{2\omega_0Ln_0}{c} + \frac{2(\omega - \omega_0)L}{\nu_{g0}} - \alpha gL = 2\pi N \quad (3.16)$$

where  $k$  is the propagation constant,  $n_0$  is the refractive index,  $\alpha$  is the Henry factor from Equation 3.13, and  $N$  is an integer. These two conditions can be visualized by plotting gain versus optical frequency (Figure 3.5a). For a broad, flat gain bandwidth, many modes may satisfy the conditions and lase.

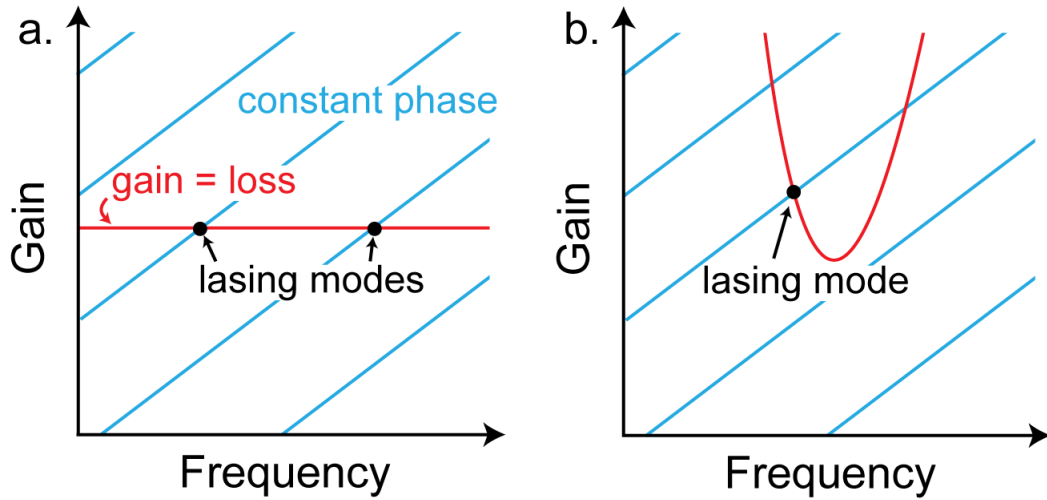


Figure 3.5: (a) Diagram of the conditions for lasing. The level of cavity loss (constant) must equal the gain, and only frequencies satisfying the integer-multiple phase condition may lase. Multiple modes with similar loss may lase in this case. (b) In the case of frequency-dependent loss, such as that introduced by a filter, a single mode may be selected to lase.

If a spectral filter is used in the cavity (Figure 3.5b), then a larger contrast between the loss of potential modes can allow for single mode lasing. The gain and frequency are related by Equation 3.16:

$$2kL = \alpha gL \quad (3.17)$$

$$\frac{2\omega L}{c} = \alpha gL \quad (3.18)$$

$$g = \frac{2\omega}{\alpha c} = \left(\frac{2}{\alpha}\right) \frac{\omega}{c} \quad (3.19)$$

The gain is therefore related to the wavenumber (in  $\text{cm}^{-1}$ ) by  $2/\alpha$ . This value is the slope of the constant phase lines in Figure 3.5. Other cavities may have much steeper phase response than the Fabry-Perot cavity considered here. For example, a ring resonator has the phase response shown in Figure 3.6. This shows a very steep slope at values close to resonance. If we now consider that the gain is perturbed by a finite amount  $\Delta g$ , the constant phase condition requires a

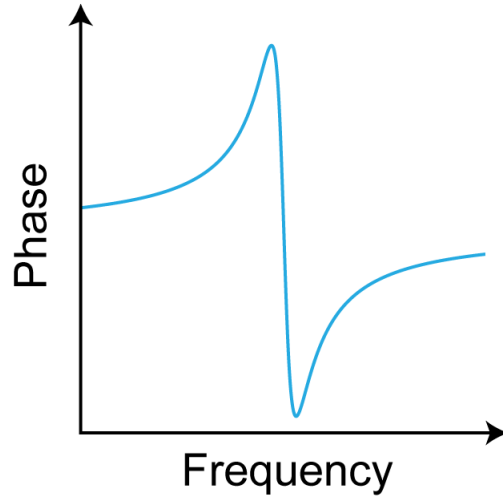


Figure 3.6: Phase response of a ring resonator close to resonance.

shift in frequency to compensate. This process is illustrated in Figure 3.7a. The change in gain  $\Delta g$  shifts the constant phase lines downward, which creates a new operating point at a frequency shifted by  $\Delta\omega_0$ . This relationship explains how frequency noise arises from changes in gain and leads to laser linewidth broadening. Now consider a laser cavity with a steeper phase response (such as that of Figure 3.6) and a frequency-dependent loss (such as that arising from a cavity filter). The new lasing condition is shown in Figure 3.7b. For the same  $\Delta g$ , a greatly reduced  $\Delta\omega$  is found. The slope of the phase is now

$$\frac{dg}{d\omega} = \frac{2}{\alpha} \left( 1 + \frac{1}{\tau_0} \frac{d\phi}{d\omega} \right) \quad (3.20)$$

$$\equiv \frac{2}{\alpha} (1 + A) \quad (3.21)$$

where  $\tau_0 = 2L_0/v_{g0}$  is the roundtrip time in the semiconductor. The  $A$  parameter indicates the relative steepness in phase compared to the Fabry-Perot cavity. Meanwhile, if we take the gain/loss curve to represent the reflection  $r$  of the

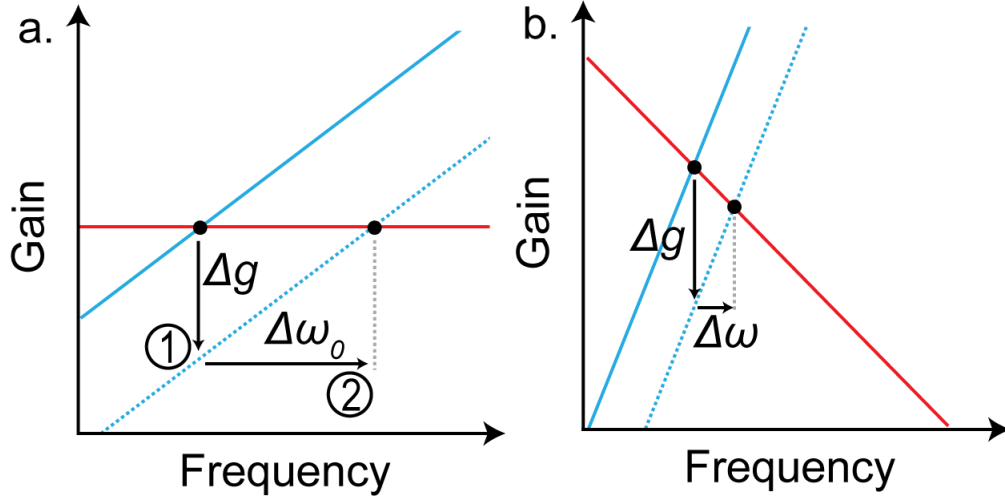


Figure 3.7: (a) Diagram showing change in lasing conditions in response to a change in gain. First, a perturbation in gain shifts the constant phase curve downwards. The lasing frequency is in turn shifted by an amount  $\Delta\omega$ . (b) The same gain perturbation  $\Delta g$  is applied to a cavity with steeper phase and loss profiles. This results in a smaller  $\Delta\omega$ . (Based on [1])

cavity, we can relate it to the gain by

$$\frac{dg}{d\omega} = -\frac{2}{\alpha} \frac{\alpha}{\tau_0} \frac{d(\ln r)}{d\omega} \quad (3.22)$$

$$\equiv -\frac{2}{\alpha} (\alpha B) \quad (3.23)$$

Here, the  $B$  parameter indicates steepness of the reflection (or loss), and like  $A$ , it also decreases the  $\Delta\omega$  from a gain perturbation. Putting these two new variables together, we can define a chirp reduction factor  $F$  as [1]

$$F = 1 + \frac{1}{\tau_0} \frac{d\phi}{d\omega} + \frac{\alpha}{\tau_0} \frac{d(\ln r)}{d\omega} \quad (3.24)$$

$$= 1 + A + B \quad (3.25)$$

This factor relates  $\Delta\omega_0$  to the reduced  $\Delta\omega$ :

$$F = \frac{\Delta\omega_0}{\Delta\omega} \quad (3.26)$$

With a passive cavity section providing feedback to the laser, phase fluctuations are reduced by  $F$ . The laser linewidth  $\Delta\nu$  is then related to the cavity linewidth without feedback  $\Delta\nu_0$  (Equation 3.14) by

$$\Delta\nu = \frac{\Delta\nu_0}{F^2} \quad (3.27)$$

The preceding derivation has shown that by decreasing the sensitivity of the lasing frequency to changes in gain, a significant reduction in linewidth can be achieved. The main factors for such a reduction are the frequency dependence of the phase (represented by  $A$ ) and of the reflection (represented by  $B$ ) introduced by the external cavity. Further, by Equation 3.15, a long length of passive section external to the semiconductor allows a narrow linewidth as well. In Chapter 6, this technique is applied to an integrated laser cavity.

## CHAPTER 4

### NONLINEAR OPTICS AND FREQUENCY COMBS

When low-intensity light of a particular color is shone through a material, its color does not change as it exits the opposite side (a prism may separate the colors of white light, but white light is not monochromatic). Doubling the intensity of light at the input would also result in a doubling of the output, with the same fraction of attenuation from the material. However, at higher intensities, light exhibits nonlinear properties.

The advent of the laser in 1960 not only produced sources of highly monochromatic light, but also those of high intensity. The strong electromagnetic fields made possible using lasers allowed Franken et al. [17] to observe laser light of 694 nm generate light at 347 nm. This halving of wavelength (doubling of frequency) was termed second-harmonic generation and marks the beginning of the study of nonlinear optics.

In the years since the foundation of nonlinear optics, many revolutionary technologies have been developed that rely on nonlinear processes. These range from modulators to microscopy and even green laser pointers. The main nonlinear technology of interest in this dissertation, frequency combs, will be explored further in Chapter 7.

In this chapter, we will derive the origins of optical nonlinearities in materials. This foundation will be expanded to nonlinear processes such as four-wave mixing, which forms the basis for the generation of frequency combs and mode-locked soliton states.

## 4.1 Nonlinear optics

When a dielectric material is placed in an electric field, the charges in its molecules reorient such that the molecules become polarized. As an electromagnetic wave, light has an electric field which affects a molecule's polarization. In a linear optical model of this effect, the polarization  $P$  is described by [18]

$$P(t) = \varepsilon_0 \chi^{(1)} E(t) \quad (4.1)$$

where  $\chi^{(1)}$  is the first-order electric susceptibility. As we can see, the induced polarization is directly proportional to the electric field, representing a purely linear relationship.  $\chi^{(1)}$  in turn relates to the index of refraction  $n$  by

$$n^2 = 1 + \chi^{(1)} \quad (4.2)$$

In a nonlinear model, the polarization can be expanded to include higher-order terms:

$$P(t) = \varepsilon_0 \chi^{(1)} E(t) + \varepsilon_0 \chi^{(2)} E^2(t) + \varepsilon_0 \chi^{(3)} E^3(t) + \dots \quad (4.3)$$

Before the high intensity of lasers was easily attainable, all but the first term on the right side of Equation 4.3 were vanishingly small due to small  $E$  values. Since then, experiments have shown that many materials can have  $\chi^{(2)}$  and  $\chi^{(3)}$  that result in strong effects.

Second-order nonlinear processes include sum frequency generation (SFG), difference frequency generation (DFG), the electro-optic (Pockel's) effect, and the second-harmonic generation (SHG) effect observed by Franken. In SHG, two photons at input frequency  $\omega_1$  go through a  $\chi^{(2)}$  material and can produce a photon at twice the frequency (half the wavelength), so energy is conserved.

$\chi^{(2)}$  exists in materials that are non-centrosymmetric (such as lithium niobate and gallium arsenide) but not in centro-symmetric materials such as silicon.

The third-order nonlinearity  $\chi^{(3)}$  is present in all materials, including silicon.  $\chi^{(3)}$  effects include third-harmonic generation (THG), two-photon absorption (TPA), nonlinear refraction, and four-wave mixing (FWM). A common example of the manifestation of  $\chi^{(3)}$  is the intensity-dependent refractive index, described by

$$n = n_0 + n_2 I \quad (4.4)$$

where the nonlinear index  $n_2$  relates to  $\chi^{(3)}$  by

$$n_2 = \frac{3}{4n_0^2 \epsilon_0 c} \chi^{(3)} \quad (4.5)$$

This effect allows a simple way to measure  $\chi^{(3)}$ , as well as interesting properties such as self-focusing (Kerr lens).

In the next section, we will focus on four-wave mixing.

## 4.2 Four-wave mixing

Four-wave mixing is a  $\chi^{(3)}$  nonlinear process whereby three optical waves mix to produce a fourth. In the non-degenerate case, the frequencies follow the relation

$$\omega_4 = \omega_1 + \omega_2 - \omega_3 \quad (4.6)$$

where  $\omega_1$ ,  $\omega_2$ , and  $\omega_3$  generate  $\omega_4$ . If  $\omega_1$  and  $\omega_2$  are equal, the FWM process is considered degenerate. The original optical waves are typically called the pump and signal, and the resulting beam the idler. In addition to generation of

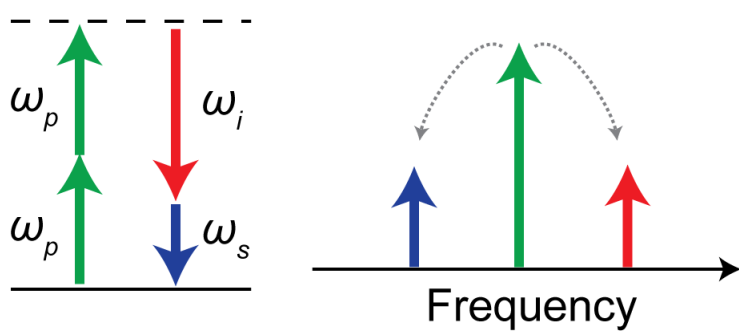


Figure 4.1: Diagram showing degenerate four-wave mixing process, whereby a pump generates sidebands. Left: energy level diagram. Right: spectral diagram.

the idler beam, the signal is amplified during this process. In degenerate FWM, Equation 4.6 becomes

$$\omega_i = 2\omega_p - \omega_s \quad (4.7)$$

This situation is shown schematically in Figure 4.1. The induced polarization from multiple fields allows an update to Equation 4.3 in the form

$$P_i^{(3)} = \varepsilon_0 \chi^{(1)} E_i + \sum_{p,p,s} \varepsilon_0 \chi^{(3)} E_p^2 E_s \quad (4.8)$$

If we assume a relatively strong pump, and that there is minimal group-velocity mismatch among the three beams, we can relate the amplitudes of the beams during propagation in a waveguide along the  $z$ -direction as

$$\frac{\partial E_p}{\partial z} = -\frac{\alpha}{2} E_p + i\gamma |E_p|^2 E_p \quad (4.9)$$

$$\frac{\partial E_s}{\partial z} = -\frac{\alpha}{2} E_s + i\gamma [2|E_p|^2 E_s + E_p^2 E_i^* e^{i\Delta k z}] \quad (4.10)$$

$$\frac{\partial E_i}{\partial z} = -\frac{\alpha}{2} E_i + i\gamma [2|E_p|^2 E_i + E_p^2 E_s^* e^{i\Delta k z}] \quad (4.11)$$

where  $\alpha$  is the propagation loss of the waveguide,  $\gamma$  is a nonlinear parameter equal to  $n_2 \omega_p / A_{eff} c$ , where  $A_{eff}$  is the mode area [19]. The phase mismatch  $\Delta k$  is given by

$$\Delta k = 2k_p - k_s - k_i \quad (4.12)$$

To meet the phase-matching condition, this linear phase mismatch must balance the nonlinear phase shift:

$$\kappa = 2\gamma P_p + \Delta k \approx 0 \quad (4.13)$$

The phase mismatch  $\Delta k$  can be approximated with the group velocity dispersion  $\beta_2$  such that

$$\kappa \approx 2\gamma P_p + \beta_2(\omega_s - \omega_p)^2 \quad (4.14)$$

Therefore,  $\beta_2$  must be negative to meet the phase-matching condition. This can be achieved by designing the waveguide geometry such that the waveguide dispersion is negative (anomalous). The dispersion balances against the self-phase modulation brought by  $\gamma$  and the pump power to remove the nonlinear phase shift.

In the next section, we will reach an application of the optical gain enabled by four-wave mixing.

### 4.3 Frequency combs

The possibility of generating new frequencies from a single laser brings many attractive possibilities. For optical communications, this means that wavelength-division multiplexing can be enabled by a single pump laser rather than an array of many lasers. Additionally, the precisely defined frequencies generated following the energy conservation conditions of FWM can be leveraged for applications ranging from metrology to waveform synthesis. For these applications, it is often desirable to control where the frequencies are generated, and if possible, to tune them.

Inside an optical resonator, a dispersion-engineered waveguide may exhibit parametric gain from FWM. An optical parametric oscillator (OPO) is achieved in a resonator, such as a microring resonator, due to the high intensity and long interaction length. The intensity enhancement in a resonator is  $(2/\pi)\mathcal{F}$ . As in a laser, the gain must exceed the loss to generate new oscillating fields. The gain is aided by the  $\chi^{(3)}$  of the material and by the optical intensity (pump power relative to mode volume  $V$ ). On the opposing side, the propagation losses of a resonator are evident in the intrinsic quality factor ( $Q_0$ ), while the coupling rate between the bus waveguide and microresonator also decreases the nonlinear interaction, lowering the loaded  $Q$  ( $Q_L$ ). The threshold power for parametric oscillation is given by [20,21]

$$P_{th} \approx 1.54 \frac{\pi}{2} \frac{Q_c}{2Q_L} \frac{n_0^2 V}{n_2 \lambda Q_L^2} \quad (4.15)$$

Once the pump power exceeds this threshold in an OPO, we expect that a set of signal and idler sidebands will be generated by degenerate FWM. The spontaneous generation of both the signal and idler is due to amplification of vacuum fluctuations. These sidebands correspond to resonant frequencies of the microresonator, separated by an integer number of FSRs. At higher pump powers, the sidebands and pump may interact to generate additional frequencies, which may in turn generate more. This process is called cascaded FWM, and the result is a comb of frequencies.

Such Kerr frequency combs have been demonstrated in many microresonator material platforms [20, 22, 23]. Microresonators generating combs may be smaller than 100  $\mu\text{m}$  in size, allowing for small mode volumes and even greater intensity enhancement. Integrated microresonator comb generation has potential application for multi-wavelength sources for optical communications

and spectroscopy. Further, frequency combs have highly precise phase properties which make them excellent for metrology. The relative line spacing is precise to  $\sim 7 \times 10^{-18}$  [22], and the pump laser frequency can be locked to a precise reference, e.g. an atomic transition. If the exact frequency spacing ( $\Delta f$ ) and carrier envelope offset ( $f_{ceo}$ ) are known, then all comb lines represent accurate frequency references. For combs spanning an octave, an  $f - 2f$  reference based on SHG allows conclusive determination of  $\Delta f$  and  $f_{ceo}$ .

## 4.4 Solitons

Optical fibers used for communications suffer from pulse broadening due to the dispersion of fiber. Hasegawa and Tappert [24] first pointed out that the nonlinear refractive index (Equation 4.4) experienced by certain pulses could be used to compensate the dispersion. These pulses have been termed solitons<sup>1</sup> due their solitary, localized, non-decaying features. Solitons were first observed by Mollenauer *et al.* in optical fibers using mode-locked color-center lasers [25]. Self-phase modulation lowers frequencies in the leading half of the pulse, while it raises those frequencies in the trailing half of the pulse. The resulting frequency chirp allows the anomalous dispersion to compress the pulse rather than broaden it. Similarly, frequency combs in microresonators can reach states balancing these effects such that a soliton state is achieved.

Solitons in microresonators can be described analytically by the nonlinear Schrödinger equation (NLSE) [26]. Take  $\mu$  as the index of each oscillating mode,

---

<sup>1</sup>The first recorded observation of waves with soliton-like features dates back to John Scott Russell in 1834. He observed water in a canal propagate at a constant velocity while maintaining its shape for over a mile.

$\phi$  as the angular coordinate in the resonator, and  $T$  as normalized time. The total waveform  $\Psi$  is then given by the sum of the oscillating fields

$$\Psi(T, \phi) = \sum a_\mu(T) e^{i\mu\phi} \quad (4.16)$$

and the NLSE is then

$$i \frac{\partial \Psi}{\partial T} + \frac{1}{2} \frac{\partial^2 \Psi}{\partial \theta^2} + |\Psi|^2 \Psi = (-i + \zeta_0) \Psi + if \quad (4.17)$$

where  $\theta$  is the longitudinal coordinate,  $\zeta_0$  is the detuning from the cold-cavity resonance, and  $f$  is a scaling factor proportional to  $\sqrt{n_2 P / V}$ . If the solution to the NLSE is a soliton, then  $\frac{\partial \Psi}{\partial T} = 0$  and the single soliton waveform is given by

$$\Psi \approx \Psi_0 + B e^{i\varphi_0} \text{sech}(B\theta) \quad (4.18)$$

where  $\Psi_0$  is a constant background field,  $B \approx \sqrt{2\zeta_0}$  defines the profile of the soliton, and  $\varphi_0$  is the phase angle. The solution is not considered exact because zero loss is assumed. The time domain waveform can be converted to the frequency domain by a Fourier transform, which is again a hyperbolic secant shape [26]

$$\Psi(\mu) = \sqrt{d_2/2} \text{sech} \left( \frac{\pi\mu}{2} \sqrt{\frac{d_2}{\zeta_0}} \right) \quad (4.19)$$

where  $d_2$  is the dimensionless dispersion. Note that it is possible for multiple solitons to propagate in the cavity, resulting in a structured, periodic spectrum that still follows the general sech envelope.

A single soliton mode-locked frequency comb emits a single pulse per roundtrip at a repetition rate corresponding to the FSR of the OPO (typically MHz to GHz range in microresonators). The narrow pulse widths are achievable through the broad parametric gain bandwidth of FWM, as opposed to mode-locked lasers which rely on saturable absorbers, typically resulting in

longer pulses (see Section 3.3). Depending on the detuning, the soliton may reach pulse durations as low as

$$\Delta t = \sqrt{\frac{2}{\pi}} \sqrt{\frac{-\beta_2}{\eta \gamma \mathcal{F} P_{in}}} \quad (4.20)$$

where  $\eta$  is  $1/2$  at critical coupling and  $P_{in}$  is the input power.

Microresonator-based solitons offer many new possibilities compared to previous fiber solitons, due to the increased control of dispersion, short cavity lengths, increased nonlinear interaction, and cavity tunability. This topic will be retouched in Chapter 7 to demonstrate a highly integrated soliton comb source.

## CHAPTER 5

### MODE MULTIPLEXING

This chapter concerns the use of the spatial degree of freedom, namely transverse modes, in order to increase the bandwidth capacity of waveguides. Such mode multiplexing approaches have received great attention for fiber transmission (sometimes using combinations of multi-core and few-mode fiber), while multimode silicon waveguides have also emerged as a platform with great potential. Here, an integrated multimode switch is first demonstrated, and in the second section a multimode link is shown.

#### 5.1 Switch

Mode-division multiplexing (MDM) offers a new dimension to scale on-chip bandwidth by utilizing the spatial modes of waveguides to carry multiple optical signals simultaneously [27–47]. The ability to switch and route such channels through a reconfigurable network would enable new functionalities for MDM, which, when combined with wavelength-division multiplexing (WDM), has been projected to allow over 4 Tbps data rate on a single multimode waveguide. However, switching has only been achieved in single-mode on-chip networks [5, 48–52]. The difficulty in implementing switching for multimode waveguides is due to the contradictory design requirements: since the mode confinements in a multimode waveguide vary significantly between the different modes, the dimensions of the photonic structure required to perform the switching differ greatly from mode to mode as well. In fiber communication, despite the fact that spatial multiplexing has allowed enormous data rates over

kilometers of fiber [53–63], its small index contrast ( $\Delta n \approx 5 \times 10^{-3}$ ) makes coupling between modes rather strong, and therefore modes are not easily separable and switching is confined only to the wavelength domain [64–68]. In integrated silicon waveguides, due to the much higher index contrast ( $\Delta n \approx 2$ ), coupling between modes is much weaker and therefore an integrated multimode platform could allow arbitrary access to individual spatial modes and wavelengths alike to enable reconfigurable switching [69,70] for fully flexible, dense, on-chip optical networks.

The following sections present an integrated multimode switch and demonstrate routing for simultaneous MDM and WDM on-chip. The switch routes four 10 Gb/s data channels independently between multimode waveguides with less than -16 dB measured crosstalk between modes.

### 5.1.1 Processing multimode signals

We propose a platform for active, integrated multimode photonics based on the independent processing of the spatial modes' signals using single-mode elements. This approach leverages the high index contrast on-chip, which in turn enables access to the individual modes. In the proposed platform, the input multimode signals are first all converted into the fundamental mode, as illustrated in step (1) in Figure 5.1 for the example case of 12 channels, consisting of three modes and four wavelengths. Once the modes are converted, processing the individual channels, now all accessible regardless of mode or wavelength, is possible, including variable attenuation (step (2) in Figure 5.1), switching or modulation. Following the processing step, the channels are then reconverted

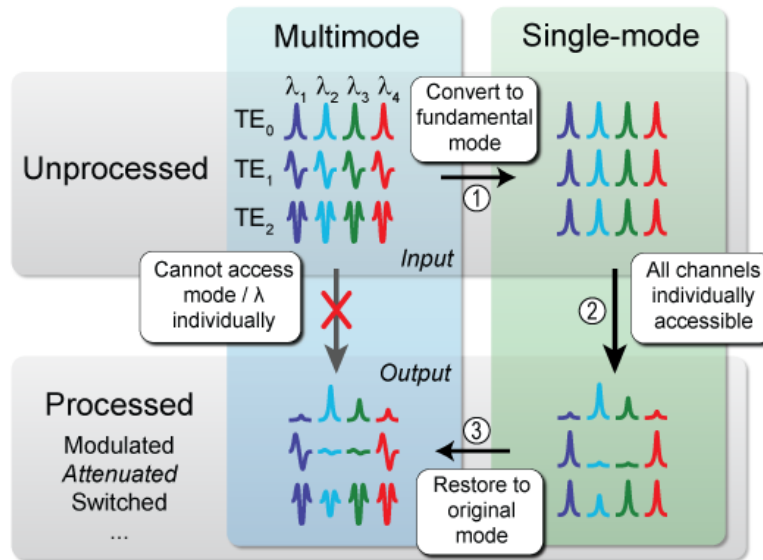


Figure 5.1: In order to enable access to individual mode-multiplexed channels, multimode signals are temporarily encoded as the fundamental mode (step (1)), and are then processed independently (step (2)). Processing by variable attenuation is shown as an example for the case of 12 channels (three modes and four wavelengths). Finally, the channels are restored as higher-order spatial modes (step (3)) and coupled to a multimode waveguide output.

into their original spatial modes at the output (step (3) in Figure 5.1).

### 5.1.2 Multimode switch

As an example of the proposed platform we show a multimode 1x2 switch for a silicon chip that supports four data channels, based on ring resonators for switching and for converting the different modes and wavelengths. The switch routes four channels, consisting of two transverse electric modes,  $TE_0$  (fundamental) and  $TE_1$ , at two wavelengths near 1550 nm, from a single input to either of the two output ports (Figure 5.2(a)). Each of the four channels can be

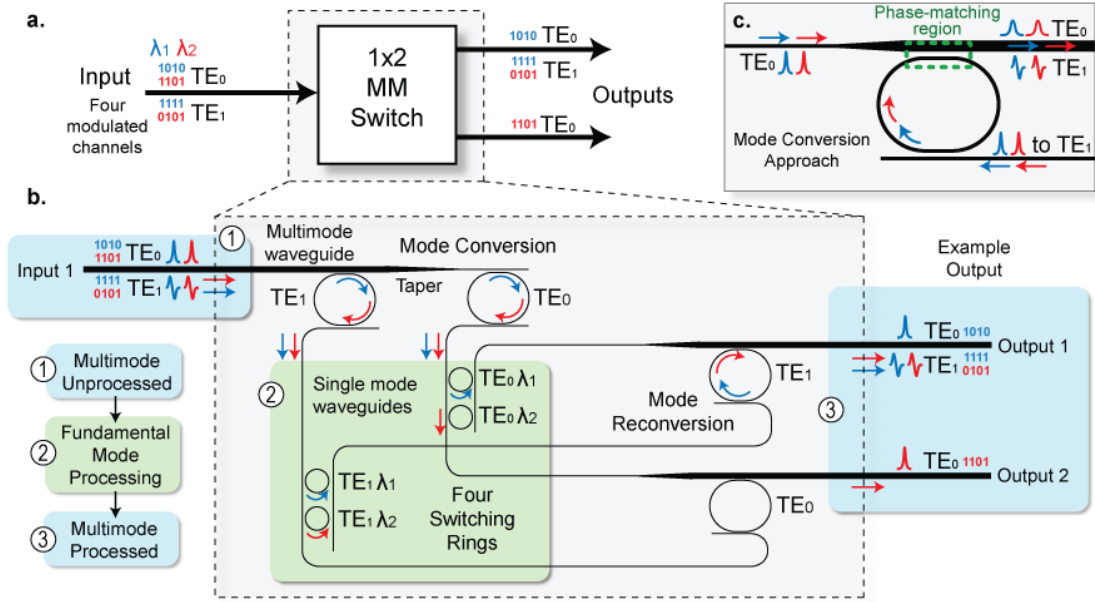


Figure 5.2: (a) Block diagram of 1x2 multimode switch operation. The four input data channels, consisting of two modes at two different wavelengths, may be switched in any combination to the two outputs. The example shows three channels routed to Output 1 and one channel to Output 2. (b) Schematic of multimode switch. The input  $TE_1$  channels are converted to the fundamental mode through phase-matching to single-mode rings. The channels are switched using actively-tuned rings to route them individually. This example shows three channels routed from Input 1 to Output 1 using on-resonance rings, and the fourth channel ( $TE_0 \lambda_2$ ) is routed from Input 1 to Output 2 using an off-resonance ring. (c) Illustration of mode (re)conversion approach showing the phase-matched coupling region.

routed independently of each other for full switching selectivity. An example switching configuration is shown in Figure 5.2(b). In order to convert all channels into the fundamental mode and back (stages (1) and (3) in Figure 5.2(b)), we optimize the waveguide widths to ensure phase-matching between the different modes in the waveguides: the  $TE_1$  in the 930-nm wide multimode bus waveguide and the  $TE_0$  in the 450-nm wide single-mode waveguides. We utilize racetrack ring resonators, as seen in Figure 5.2(c), to enhance the coupling

between these modes for efficient conversion within a short coupling section, as demonstrated in our previous work [44].

The coupling gaps between the rings and waveguides are chosen to meet the critical coupling condition in Equation 2.48. To enable 10 Gbps operation,  $\kappa$  and  $\kappa'$  (power coupled between the ring and add/drop waveguides) are also optimized for a bandwidth of 16 GHz per ring, although this narrows when rings are in series. The coupling gaps, calculated by the eigenmode expansion method based on the waveguide geometry, are listed in Table 5.1. The racetrack ring resonators used for the (de)multiplexers have radii of 16  $\mu\text{m}$  and coupling lengths ( $L_c$ ) of 5.9  $\mu\text{m}$ , at which the crosstalk is minimized due to the phase-matching. The switching rings have 8.6  $\mu\text{m}$  radii and 1.2  $\mu\text{m}$  coupling lengths, for half the circumference of the multiplexing rings.

Table 5.1: Table of coupling gaps for ring resonators in multimode switch.

Coupling region	Gap (nm)
TE <sub>1</sub> MM to SM ring - Add port	210
TE <sub>1</sub> MM to SM ring - Drop port	220
TE <sub>0</sub> SM to SM ring - Add port	250
TE <sub>0</sub> SM to SM ring - Drop port	260
Switching Ring - Add port	190
Switching Ring - Drop port	200

The switching backbone (stage (2) in Figure 5.2(b)) also consists of ring resonators to allow for compact, active control by integrated heaters [71]. These rings have a smaller radius of 8.6  $\mu\text{m}$  (for a free spectral range (FSR) of 10 nm) and are only tuned into resonance when the desired channel is set to be

switched, in contrast to the rings employed for mode conversion which have a larger  $16\ \mu\text{m}$  radius (for an FSR of  $5\ \text{nm}$ ) and are always kept tuned on resonance so that at all wavelengths the channels are converted between modes [72]. Note that, in principle, increasing the number of rings used for switching and tripling, quadrupling, etc. the FSRs of the rings used for conversion would enable additional wavelength channels (see section 5.1.7).

### 5.1.3 Device fabrication

We demonstrate the switch using high-index-contrast silicon waveguides fabricated on a silicon-on-insulator (SOI) wafer with  $250\text{-nm}$  thick silicon device layer on  $3\ \mu\text{m}$  buried oxide. The waveguides are patterned using electron beam lithography and fully etched using reactive ion etching. The devices are then clad with  $1\ \mu\text{m}$  of plasma enhanced chemical vapor deposition (PECVD)  $\text{SiO}_2$ . A thin Cr adhesion layer and  $100\ \text{nm}$  of Ni are evaporated along with a lift-off process to define the heaters for tuning resonances. For the metal contacts,  $1.7\ \mu\text{m}$  of Al is sputtered with a thin Ti adhesion layer and then etched using inductively coupled plasma. Deep trenches are etched into the silicon substrate near the input and output waveguide tapers for improved coupling [73,74]. The final chip is mounted to a custom printed circuit board (PCB), onto which the Al pads are wirebonded out for easy control of heater tuning by DC voltages. Figure 5.3(a-b) shows microscope and scanning electron microscope (SEM) images of the on-chip multimode switch. The switch area is less than  $0.07\ \text{mm}^2$ , and an even more compact design could be achieved by using smaller tapers or placing components closer together.

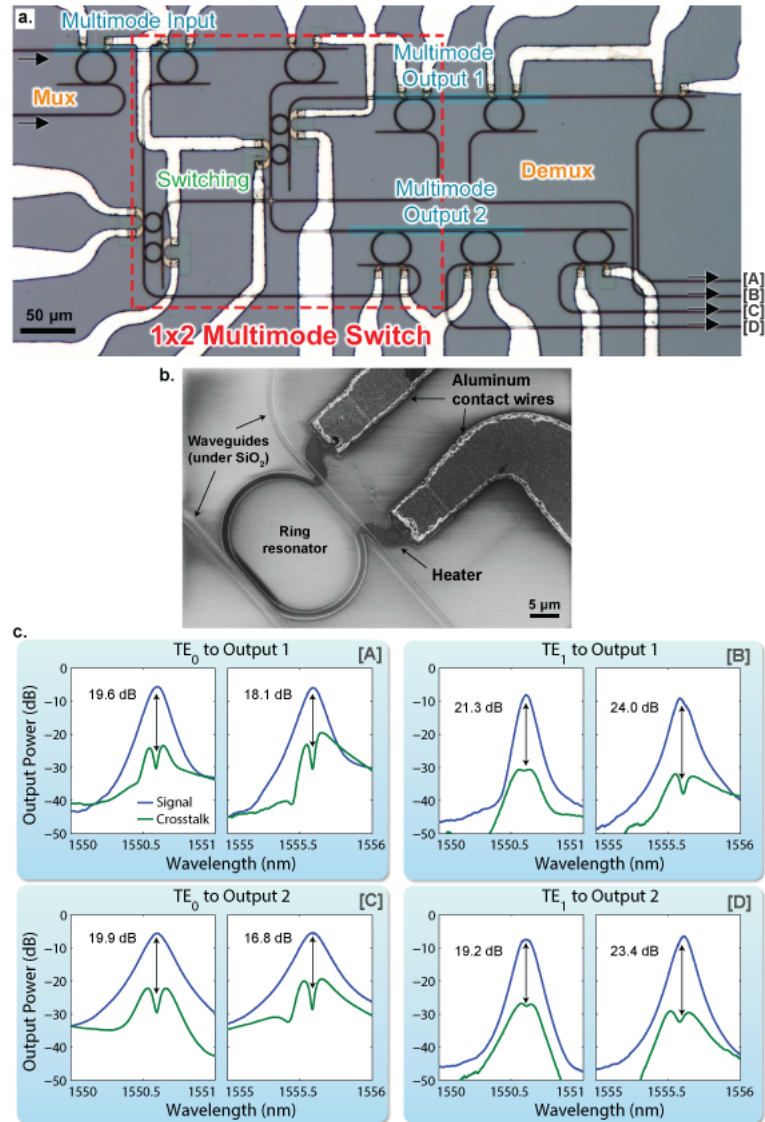


Figure 5.3: (a) Optical microscope image of fabricated device. The input channels are coupled into single-mode waveguides from an off-chip laser, and a multiplexer (mux) produces the MDM input to the multimode switch. The areas highlighted in blue show the multimode waveguides. The four small rings actively switch the four channels and are tuned by integrated heaters. Following the switch, each of the two outputs is demultiplexed (demux) so that the channels can be individually monitored off-chip. (b) SEM image of a ring resonator in the fabricated device with active heater used to tune the resonance. (c) Crosstalk measurements for the different channels. Spectral profiles at both outputs for each of the input four channels, compared with the profiles from interfering channels.

## 5.1.4 Results

We measure less than -16.8 dB crosstalk when switching each of the four individual channels to the different output ports. In order to couple on and off the chip using single-mode edge coupling based on an inverted taper [74], a mode (de)multiplexer is added to the input (outputs) of the switch [44]. We measure the intermodal crosstalk between channels by launching one channel at a time and detecting the power within the channel's bandwidth at each output to compare the desired signal with leaked, interfering signals from other channels (Figure 5.3(c)). For all channels and switching configurations, this crosstalk remains low, ranging from -16.8 to -24.0 dB for each channel. These crosstalk values are comparable to previous integrated multimode multiplexer systems [36, 39, 44], indicating that the switch introduces negligible crosstalk. The measured insertion loss, including on- and off-chip coupling losses, is 5.4 to 9.1 dB for the different four channels. Based on the measured losses from test structures that do not include the switch or multiplexers, we estimate the losses due to the switch and multiplexers together to be between 0.9 dB and 4.6 dB. This mode-dependent insertion loss is likely due to variations in the rings' coupling (and therefore extinction ratio [9]) and also a result of narrowing bandwidth after multiple conversion steps, which leads to greater losses for the higher-order modes in this case. The extinction ratio can in principle be improved using tunable couplers such as interferometers on the single-mode coupling regions of the rings [75], and a wider bandwidth for the rings through stronger coupling can prevent accumulated loss during each conversion step.

Our 1x2 multimode switch exhibits bit-error rates (BER) below  $10^{-9}$  on all channels, and open eye diagrams while routing 10 Gb/s data when each chan-

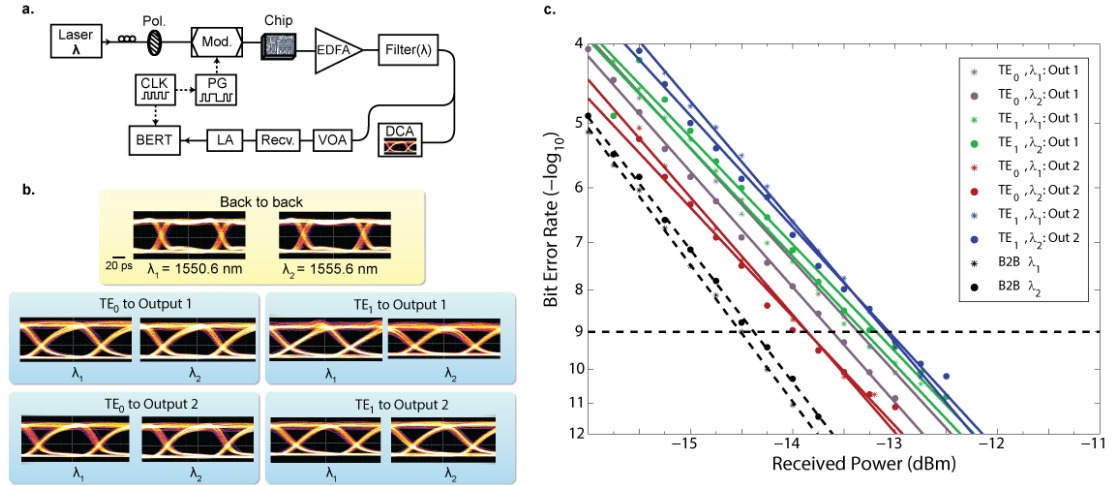


Figure 5.4: (a) Testing configuration, including tunable laser, polarization controller, fiber polarizer, electro-optic modulator (Mod.), pattern generator (PG) for the  $2^7 - 1$  pseudo-random binary sequence (PRBS), function generator clock source (CLK), Er-doped fiber amplifier (EDFA), tunable band-pass filter (1.4 nm), digital communications analyzer (DCA), variable optical attenuator (VOA), optical receiver (Recv.), limiting amplifier (LA), and bit-error rate tester (BERT). (b) Eye diagrams of the switched signals for all channels at both outputs are open. Comparison with the rise time of back-to-back eyes confirms that the output signal is bandwidth-limited. (c) Error free transmission ( $\text{BER} < 10^{-9}$ ) is achieved with power penalties ranging from 0.5 to 1.4 dB, compared to the back to back (B2B) references.

nel is input and routed separately. We perform the experiment using a tunable laser modulated by a pseudo-random binary sequence (PRBS) from a pattern generator (Figure 5.4(a)). The modulated light is coupled onto the chip using a tapered fiber. A DC voltage is applied to each integrated heater to align their resonances with the laser or to tune and detune the resonances of the rings used for switching to route the channels to the outputs. The total power supplied to the heaters is up to 30 mW, depending on the switching state, and is almost entirely used for aligning the resonances of all rings due to fabrication variations.

A back-to-back reference for the transmission experiment is measured for each wavelength by removing the chip and replacing the tapered fibers with a single fiber connection. The output signal from the chip is amplified and filtered (to reject amplified spontaneous emission (ASE) noise) to obtain optical eye diagrams of the transmitted data pattern (Figure 5.4(b)). One can see that the signals exhibit open eye diagrams for all four channels routed to either output. We further characterize the data integrity with BER measurements (Figure 5.4(c)). We measure error-free switching ( $\text{BER} < 10^{-9}$ ) for all channels, with the power penalty ranging between 0.5 and 1.0 dB for  $\text{TE}_0$  and 1.2 to 1.4 dB for  $\text{TE}_1$ .

The switch exhibits an additional power penalty of less than 2.4 dB when all four channels are simultaneously inserted onto the chip and routed. In order to accommodate two wavelength channels ( $\lambda_1$  and  $\lambda_2$ ), we decorrelate them using 500 m of single-mode fiber (SMF) and then combine and split them equally on two paths (Figure 5.5(a)). Another length of 2 km of fiber on one path ensures phase decoherence of the two paths, as it is several times the laser coherence length of 450 m. Each path has equal power and is coupled simultaneously into the  $\text{TE}_0$  and  $\text{TE}_1$  inputs respectively using a pitch reducing optical fiber array (PROFA) [76]. A tapered fiber is used to selectively measure the outputs of the chip by mode, and the tunable filter is aligned to measure by wavelength channel. We observe open eye diagrams for the four simultaneously routed 10 Gb/s channels (Figure 5.5(b)). The back to back references are measured by replacing the chip and PROFA with an attenuator to replicate each path's insertion loss. We also measure the BER for all channels (Figure 5.5(c)) for the highest crosstalk configuration, i.e. when the mode channels are routed to the same output. We observe power penalties of 2.4 to 5.1 dB for simultaneous operation, and error-free switching ( $\text{BER} < 10^{-9}$ ) for all channels except  $\text{TE}_1\lambda_1$  at Output 1, which

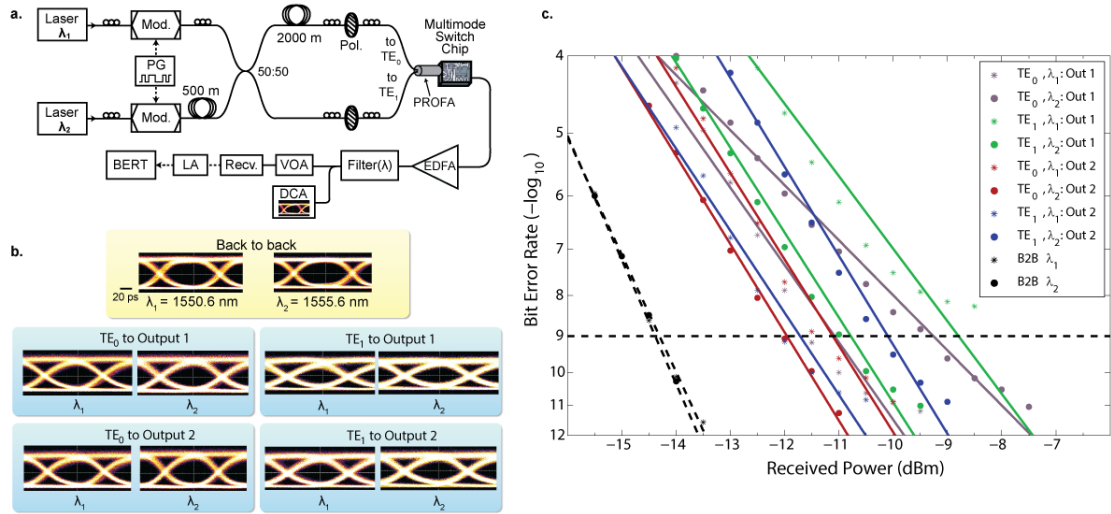


Figure 5.5: (a) Testing setup for simultaneous switching, derived from that of Figure 5.4a, includes fiber spools for decorrelation and decoherence of data channels, a 50:50 combiner/splitter, and pitch reducing optical fiber array (PROFA). Solid connections are in fiber, and dotted connections are electrical. (b) Eye diagrams for each 10 Gb/s channel switching to either output. (c) Bit-error rate measurements for simultaneous operation of all channels. The worst-case switching configuration for each channel is plotted. For each channel, a back to back reference was measured by replacing the PROFA and chip with an attenuator replicating the insertion loss. The best-performing back to back measurements for each wavelength are plotted. All channels achieve error-free ( $\text{BER} < 10^{-9}$ ) transmission, except the  $\text{TE}_1\lambda_1$  channel, which is impaired when switched to Output 1 due to a fabrication error causing one ring resonator to be under-coupled with a narrow bandwidth.

reaches  $5 \times 10^{-9}$ . The additional power penalty of 1.8 to 2.4 dB due to simultaneous operation could be minimized by optimizing the bandwidth of each ring to equalize the effect of intrachannel crosstalk among the different paths. The higher power penalty for channel  $\text{TE}_1\lambda_1$  at Output 1 is due to a fabrication error causing one switching ring to be under-coupled, resulting in a narrow bandwidth of only 9 GHz, compared to the larger bandwidth for the other channels

of approximately 13 GHz.

### 5.1.5 Fabrication tolerance of mode multiplexing

Asymmetric coupling regions are used in the multiplexing, demultiplexing, and mode conversion steps of the switch in order to selectively couple to particular modes. The multimode waveguides are designed to be 930 nm wide to accommodate phase-matching of the  $TE_1$  mode with the  $TE_0$  mode of 450-nm wide single-mode waveguides (see Figure 5.6) [44]. At this combination of widths, the effective indices of the modes in their respective waveguides match with index 2.46, and so the  $TE_0$  mode in the single-mode waveguide selectively excites the  $TE_1$  mode in the multimode waveguide, without also exciting the  $TE_0$  therein, which would contribute to crosstalk. The phase-matching condition is tolerant to typical fabrication variations in waveguide width (Figure 5.7). For example, an alteration of the multimode waveguide width within a 50-nm range leads to a drop of only 1% in coupling to the ring from a peak of around 9%. The peak coupling occurs at a slightly narrower width than the point of effective index matching because the mode is more delocalized, but the phase-matching is still mostly in effect. If the fundamental mode alone is present in a waveguide, it can be adiabatically tapered wider or narrower without disturbing the mode. The adiabatic taper length used is 95  $\mu\text{m}$ .

Propagation of modes in multimode waveguides in principle should not lead to significant mode mixing, even with typical sidewall roughness. From coupled-mode theory, the period of a spatial perturbation can lead to coupling between modes with different propagation constants (i.e. different index) [77].

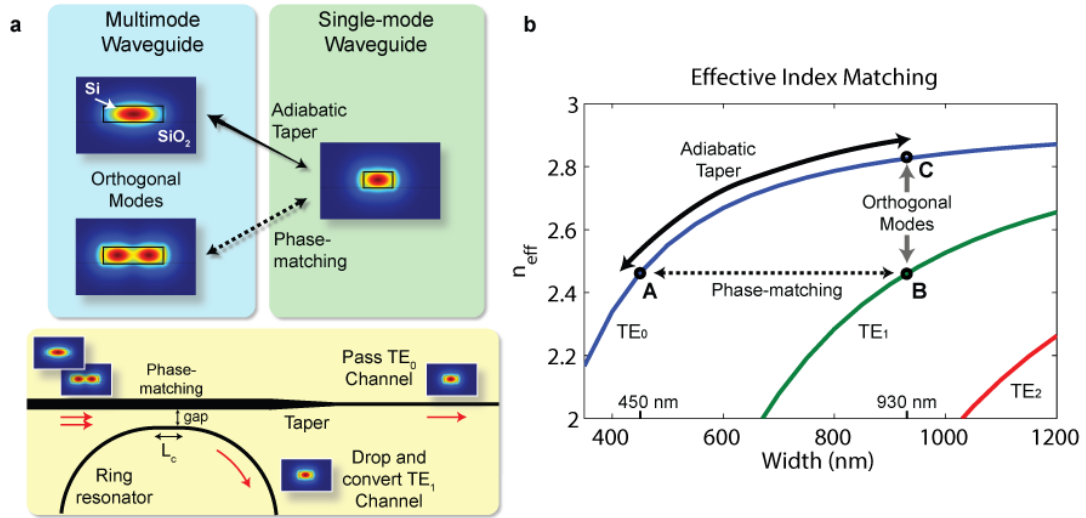


Figure 5.6: (a) Method for accessing individual modes in a multimode waveguide. A single-mode ring resonator which is properly phase-matched to the bus waveguide will drop the TE<sub>1</sub> channel, while the TE<sub>0</sub> channel can be adiabatically tapered into a single-mode waveguide. (b) Simulated effective index of 250-nm tall Si waveguide as a function of width. The phase-matching condition is met when the index for TE<sub>0</sub> in the single-mode waveguide (point A) matches that of the TE<sub>1</sub> in the multimode bus waveguide (point B). The TE<sub>0</sub> signals can adiabatically taper to the same width as the multimode bus waveguide (point C) and back.

This relation is given by

$$\frac{2\pi}{\Lambda} = \Delta\beta = \frac{2\pi\Delta n}{\lambda} \quad (5.1)$$

where  $\Lambda$  is the spatial period of the perturbation,  $\Delta\beta$  is the propagation constant difference, and  $\Delta n$  is the refractive index difference of the modes. Rearranging, we obtain the period

$$\Lambda = \frac{\lambda}{\Delta n} \quad (5.2)$$

For telecom wavelengths and index differences on the order of those in Figure 5.6(b) (vertical separation between modes), the period is about 5  $\mu\text{m}$ . How-

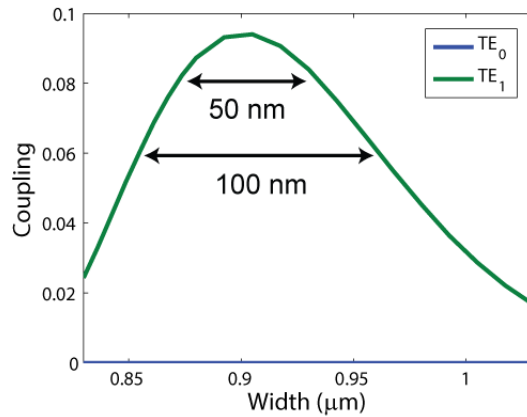


Figure 5.7: Sensitivity of phase-matching to width for coupling between  $TE_0$  mode in 450 nm waveguide and  $TE_1$  mode in 930 nm waveguide. The simulation shows a large tolerance for fabrication variations in width dimensions of waveguides.

ever, typical waveguide sidewall roughness has a correlation length of 50-100 nm with magnitude on the order of 2-5 nm. [78,79]. Thus the unwanted coupling between modes through this mechanism is inefficient.

### 5.1.6 Discussion

This demonstration of the first integrated multimode switch establishes MDM as a viable platform for optical interconnects. It allows scaling of bandwidth density for on-chip networks by expanding routing to include waveguides employing simultaneous MDM and WDM for multi-dimensional multiplexing. The ability to route on-chip MDM-WDM signals with full flexibility enables integrated networks with many nodes connected by high-bandwidth multimode links to dynamically allocate bandwidth. While each multimode input or output in this demonstration carries 40 Gb/s aggregate bandwidth ( $4 \times 10$  Gb/s), the design is scalable in principle to more modes and wavelengths. In addition,

the switching design can be optimized to accommodate higher data rates such as 25 Gb/s at the expense of fewer wavelength channels while still reaching similar aggregate bandwidths. In principle one can also use MDM channels to reduce the number of independent laser sources required. Because lasers are the dominant cause of power consumption in WDM systems [80], mode channels can also significantly reduce power consumption. The platform we present for processing multimode signals in the single-mode domain also creates the possibility for numerous future applications of MDM beyond routing, such as modulation, attenuation, or performance monitoring.

### 5.1.7 Scaling considerations for multimode switching

Expanding the number of mode and wavelength channels supported by the switch allows for further expansion of bandwidth. For increasing the number of wavelength channels beyond the two demonstrated, an additional switching ring is needed per mode such that the total number of switching rings follows  $mn_\lambda$ , where  $m$  is the number of modes, and  $n_\lambda$  is the number of wavelengths. This is also the total number of channels, because each channel is switched individually by a dedicated ring. Scaling to more modes requires conversion rings to phase-match to each multimode waveguide width. The number of conversion rings is  $3(m - 1)$ , which is independent of the number of wavelength channels. The number of rings passed through by channels does not change when scaling to more wavelengths or modes.

The adiabatic taper length needed for sufficiently low crosstalk can be greatly reduced in future switch designs. Simulations show that when linearly

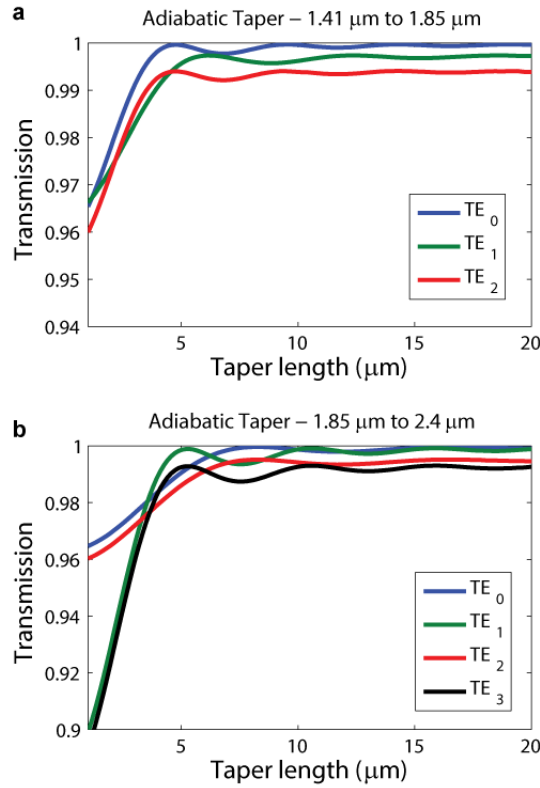


Figure 5.8: Simulated mode transmission for adiabatic linear taper of width of multimode silicon waveguides. All modes rapidly reach high transmission when taper lengths exceed several micrometers. In (a), a taper from 1.41  $\mu\text{m}$  width to 1.85  $\mu\text{m}$  is 99% efficient in just 4  $\mu\text{m}$ , while in (b), from 1.85  $\mu\text{m}$  to 2.4  $\mu\text{m}$ , this efficiency is reached by 6  $\mu\text{m}$ .

tapering width from a multimode waveguide with three modes to a waveguide with four, more than 99% of each mode is preserved in the proper channel with a taper length as short as 4  $\mu\text{m}$  (Figure 5.8(a)). For a taper of a four-mode waveguide to a five-mode waveguide, only 6  $\mu\text{m}$  is required (Figure 5.8(b)). Nonlinear tapers, with parabolic or exponential profiles for example, may optimize this further. The 95  $\mu\text{m}$  taper used in our demonstration can be reduced in length dramatically, and for several mode channels, taper length should not be a dominating concern for area. Thus the total area depends predominantly on the number of rings and scales at most linearly with the number of modes.

## 5.2 Multimode on-chip link

The previous section introduced the first dynamic device for mode multiplexing in silicon waveguides. This section proposes greater integration of mode-multiplexed devices by establishing a data link on-chip through a multimode waveguide.

Silicon photonics has enabled great advances for on-chip optical communications [81], but a major obstacle to adoption of high-bandwidth silicon links is the reliance on using multiple laser sources for wavelength-division multiplexing (WDM). Stabilizing the lasers requires a significant portion of the total power, and integration of multiple lasers can be costly [82, 83]. Additionally, silicon modulators experience larger power penalties at data rates beyond the optimal regime of operation near 10 Gb/s [84].

We achieve a high bandwidth link on-chip using only a single laser source by multiplexing separately modulated signals as spatial modes of a single silicon waveguide. Recent demonstrations of mode-division multiplexing (MDM) have used off-chip modulators and encoded multiple channels as orthogonal

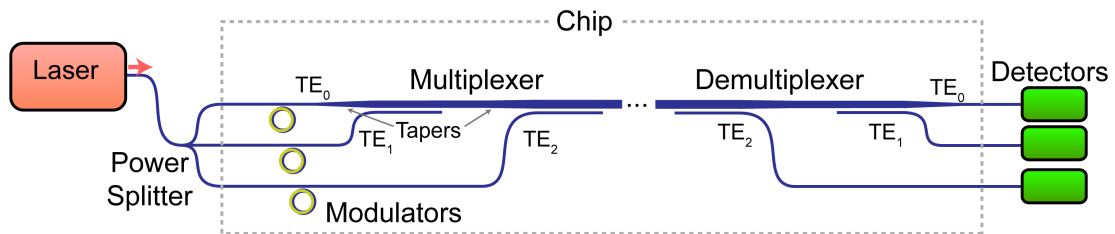


Figure 5.9: Diagram of integrated multimode link design. A single laser is used for all three channels, while after modulation, each channel is multiplexed into its respective mode. At the end of the transmission region, the signals are demultiplexed.

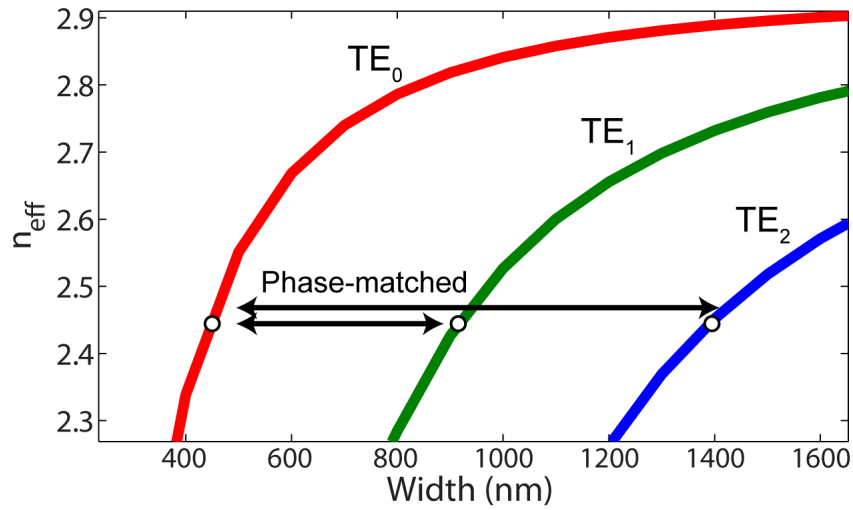


Figure 5.10: Plot of effective index versus waveguide width for the modes supported in a multimode silicon waveguide.

modes of a bus waveguide [44]. Here we extend this approach and demonstrate full integration of silicon modulators for a MDM link on a single chip. Our approach allows the input laser power to be split among several modulators (Figure 5.9), whose signals are then encoded as orthogonal modes on a bus waveguide. The channels can later be demultiplexed for signal detection. By substituting WDM with MDM, the modulators can operate at moderate, efficient data rates, and the constraints imposed by multiple laser sources are relieved.

In our design, three channels are multiplexed using asymmetric directional couplers with widths optimized for phase-matching between different spatial modes. Each modulated signal is excited in a different mode of a multimode bus waveguide by optimizing the directional coupler dimensions for phase-matching [39]. When the effective index of refraction ( $n_{\text{eff}}$ ) of the fundamental transverse electric ( $\text{TE}_0$ ) mode matches that of a higher-order mode in a wider waveguide (Figure 5.10), they match in phase and couple. The higher-order

modes can be excited in this way. For 250 nm thick silicon-on-insulator (SOI) waveguides,  $TE_0$  in a 450 nm wide waveguide matches  $TE_1$  for 930 nm width and  $TE_2$  for 1410 nm. The lower order modes are multiplexed first, and the bus waveguide can be adiabatically tapered to wider widths while preserving the existing modes, and then the higher order modes can be coupled in.

To reduce interchannel crosstalk between the modes, we optimize the multiplexer and demultiplexer for low coupling to unwanted modes. First, coupling to all modes is weaker with a larger gap, but if the desired mode is phase-matched then all power transfers to it with the proper coupling length. Therefore we use a gap of 300 nm to suppress crosstalk. This gap requires coupling lengths near 100  $\mu\text{m}$  to reach full excitation of the higher-order modes, but by adjusting the coupling length slightly in the vicinity of full power transfer, the unwanted modes can be suppressed by taking advantage of the periodic coupling from the phase mismatch (see for example Figure 2.8c). For a 300 nm gap, we expect 96.5  $\mu\text{m}$  coupling length for  $TE_1$  and 111  $\mu\text{m}$  coupling length for  $TE_2$  should minimize crosstalk significantly according to simulations.

The on-chip silicon modulators are single-mode microring resonators with pn junctions across the waveguides [12]. Figure 5.11a shows a microscope image of the fabricated silicon ring modulator, which has a radius of 18  $\mu\text{m}$ . The silicon waveguide is partially etched around the ring, rather than fully etched, so that highly doped silicon contacts to metal vias can be used. The pn junction is shifted 75 nm from the center of the waveguide so that the extent of the depletion width, i.e. the part that modulates, overlaps with the center of the mode (the highest intensity) (Figure 5.11b).

The desired bandwidth of 20 GHz indirectly determines the ideal implan-

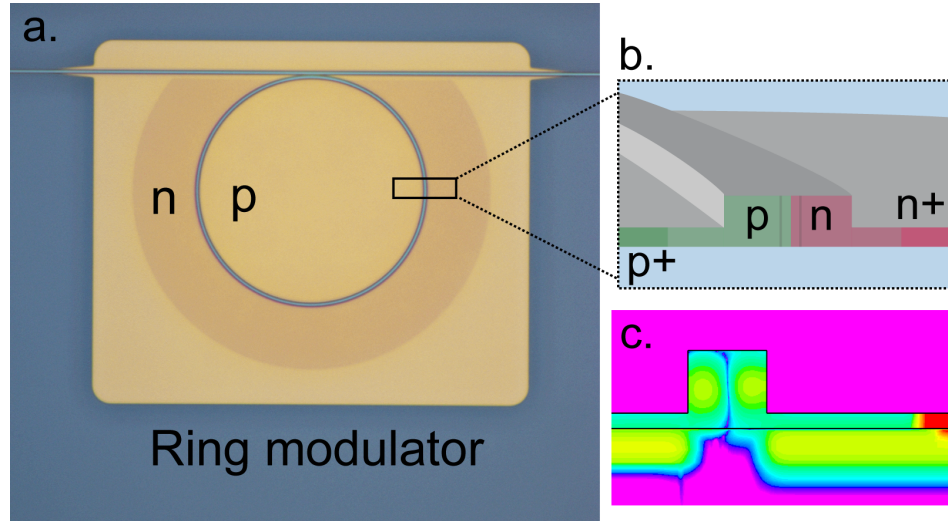


Figure 5.11: (a) Microscope image of fabricated microring modulator before cladding and metal deposition. The yellow box around the ring is a remaining 50 nm slab of silicon, while elsewhere the waveguides are fully etched. (b) Cross-sectional view showing pn junction location in waveguide. (c). SILVACO simulation of dopant density following implantation and anneals.

Table 5.2: Table of implantation values for ring modulator.

Implant Step	Dose ( $cm^{-2}$ )	Energy (keV)
n	$8 \times 10^{13}$	99
n+	$3 \times 10^{15}$	30
p	$8.5 \times 10^{13}$	33
p+	$2 \times 10^{15}$	10

tation conditions. To have a resonance bandwidth of 20 GHz at critical coupling, a loss of 38 dB/cm is needed, as well as 9.9% power coupling to the bus waveguide. An ion implantation dose resulting in a doping concentration of  $5 \times 10^{18} cm^{-3}$  gives this loss, according to Equation 2.58. For implantation, phosphorus and boron are used at the doses and implant energies described in Table 5.2. The implantation and anneals are simulated using SILVACO soft-

ware with Auger and Hall-Shockley-Read models (Figure 5.11c). At 5 V reverse bias, the carrier profile is overlapped with the optical mode profile, and using Equation 2.57, the index shift is calculated. Compared to zero bias, the index variation is  $3.5 \times 10^{-4}$  due to the expanded depletion region, sufficient to shift the ring resonance for modulation.

We fabricate the modulators with the mode (de)multiplexer on a SOI wafer. The waveguides are patterned using electron-beam lithography and etched to leave a 50 nm slab around the modulators and fully etched elsewhere. Before implantation, a thin layer of SiO<sub>2</sub> is deposited with atomic layer deposition (ALD) in order to avoid tubular holes during implantation. The modulator waveguides are then implanted with phosphorus and boron before being annealed at 550 °C and then 900 °C. A rapid thermal anneal at 1050 °C is also used to repair the lattice and allow diffusion of dopants. The device is then clad with 1 μm of PECVD SiO<sub>2</sub>. Platinum heaters for tuning resonances are patterned, sputtered and lifted off. Finally vias are etched to contact the silicon modulators and aluminum is deposited for the wire contacts.

The diode current-voltage curve is measured (Figure 5.12) to confirm rectification performance. A series resistance of 23 Ω is derived. The simulated capacitance of 45 fF matches closely with the measured value of 40 fF. Therefore the RC constant corresponds to  $f = 1/(2\pi R C) = 170$  GHz, which indicates that the modulator should be limited by the photon lifetime (cavity bandwidth) rather than RC.

We measure the multiplexing performance of the device by injecting light at 1555 nm into the mode channels individually. Without modulation, we measure maximum crosstalk levels for TE<sub>0</sub>, TE<sub>1</sub> and TE<sub>2</sub> of -26.3 dB, -21.6 dB and

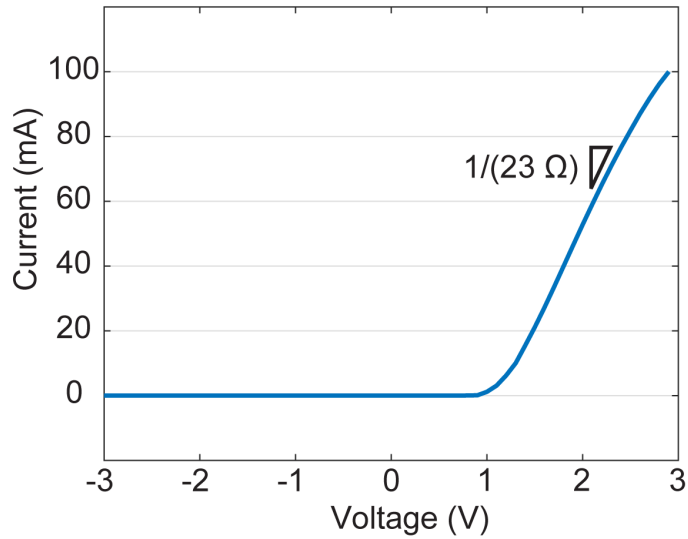


Figure 5.12: Measured current-voltage characteristics of the ring modulator. Device operation for modulation is in reverse bias.

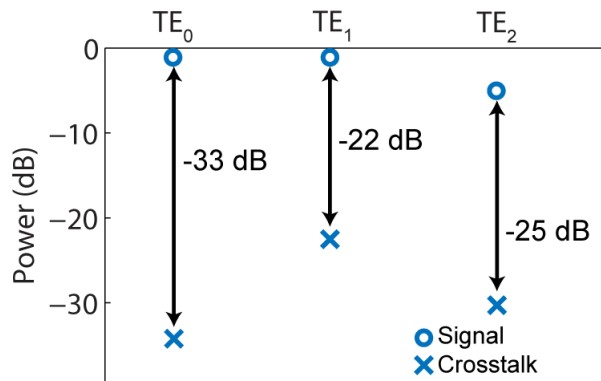


Figure 5.13: Plot of measured crosstalk and insertion loss for each channel accounting for the optimal wavelength of each.

-15.1 dB, respectively, from the other interfering channels. The on-chip insertion loss for  $TE_0$  is negligibly low compared to a simple waveguide, while the loss for  $TE_1$  is approximately -1 dB and  $TE_2$  is about -13 dB. The lower performance for  $TE_2$  likely stems from varied waveguide dimensions altering the expected phase matching condition. However, at certain wavelengths in the C-band, the crosstalk improves to -33.1 dB, -21.5 dB and -24.8 dB respectively, and the in-

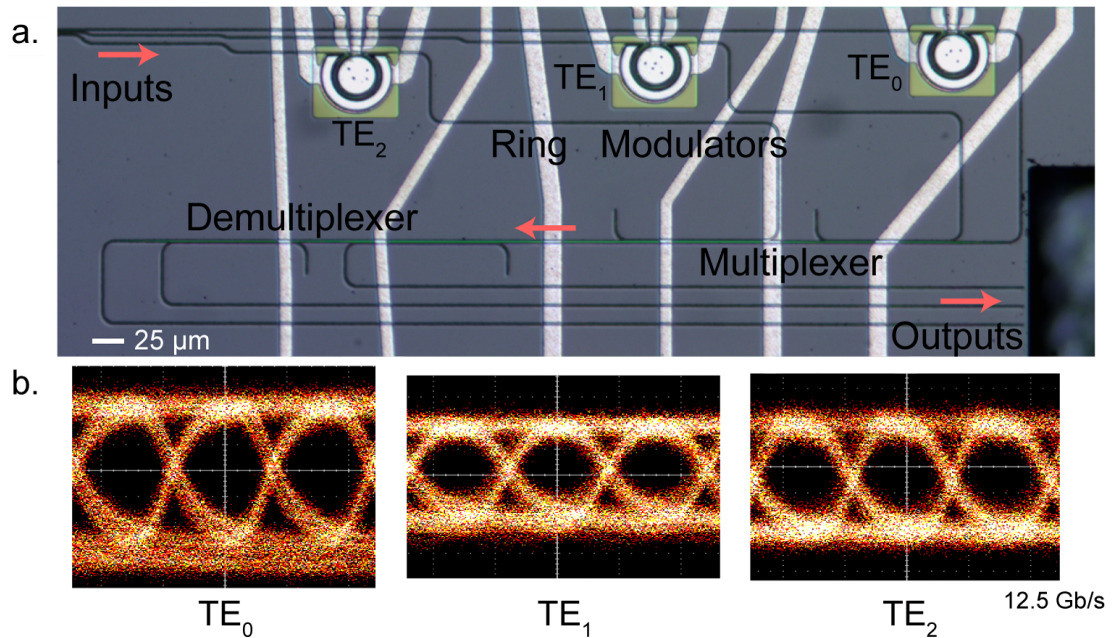


Figure 5.14: (a) Microscope image of silicon chip showing microring modulators, mode multiplexers, and demultiplexers. (b) Eye diagrams at 12.5 Gb/s for the three modes.

sersion loss for  $TE_2$  improves to better than -5 dB (Figure 5.13). Therefore it is expected that a calibration based on fabricated devices could provide optimal results at a single wavelength for all modes.

The integrated ring modulators each function at 12.5 Gb/s with open eye diagrams (Figure 5.14). The modulators operate in reverse bias at -3 V with 7  $V_{pp}$  driving voltage. For experimental purposes, a probe with a 50  $\Omega$  resistor in parallel is used for impedance matching; otherwise the DC current is negligible. The extinction ratio reaches -10 dB with a 26 GHz bandwidth, giving fully open eye diagrams with a pseudo-random binary sequence input pattern. Stabilization of the ring resonance and better coupling efficiency to the chip will provide further improvements in high speed measurements.

We have demonstrated the capability of 37.5 Gb/s on-chip bandwidth by multiplexing three modulators, operating at 12.5 Gb/s each, into separate spatial modes of a silicon waveguide. This approach allows expansion to much higher aggregate data rates while bypassing the potentially prohibitive power consumption and cost of multiple lasers or high data rate modulators. For example, using 8 modes for both polarizations at 25 Gb/s data rate would allow 400 Gb/s aggregate bandwidth with a single laser in a single waveguide. Highly dense on-chip networks or optical I/O may benefit from this expansion in available bandwidth.

## CHAPTER 6

### INTEGRATED NARROW LINEWIDTH LASER

#### 6.1 Introduction

Narrow linewidth lasers are critical for a wide range of applications that require either long coherence lengths or superior phase sensitivity. These include optical communications [85], sensing [86], spectroscopy [87], light detection and ranging (LIDAR) [88], quantum optics [89], and atomic clocks [90]. Optical communications is of particular interest as network capacity demands rapidly grow. In order to expand the capacity of long-haul, metro, and short distance optical links, advanced modulation formats using coherent systems have emerged. Such formats modulate phase in addition to amplitude in order to increase aggregate data rates. This reliance on phase sets stricter requirements for laser linewidth. For example, 16-state quadrature amplitude modulation (16QAM) can require linewidths below 100 kHz, and higher formats have requirements down to the single kHz level [15], far narrower than the approximately 1 MHz linewidth of typical distributed feedback (DFB) or distributed Bragg reflector (DBR) lasers.

Optical networks are moving towards integrated, chip-based solutions in order to address the size, power, and cost of optical transceivers [91,92], with most research focusing on silicon cavities. In systems integrating multiple lasers, e.g. wavelength-division multiplexing (WDM), the realization of compact lasers enables scaling and cost reduction. Integrated, tunable lasers based on silicon photonics have been demonstrated using III-V materials such as indium phosphide, which has been bonded [93,94], epitaxially grown [95], or hybridly

attached [96–99] to the silicon chip. These electrically-pumped lasers have achieved excellent output power, efficiency, and tuning range, with linewidths reaching below 10 kHz [98].

Compact narrow-linewidth lasers based on silicon nitride ( $\text{Si}_3\text{N}_4$ )—a CMOS-compatible, deposited material with low nonlinear losses—would provide numerous advantages over silicon for many applications. In contrast to silicon,  $\text{Si}_3\text{N}_4$  is not limited by two-photon absorption or free-carrier absorption at higher powers [100], while still having a high index contrast ( $\approx 0.5$ ) allowing for compact devices. Additionally, its transparency extends to visible wavelengths, enabling additional applications [86, 89, 90]. While  $\text{Si}_3\text{N}_4$  integrated laser cavities reaching linewidths as low as 24 kHz [101–105] have been demonstrated, they rely on mode delocalization in order to achieve low loss, requiring long lengths [101–104] or large areas (on the order of several  $\text{mm}^2$ ) in order to ensure low bending losses [105].

## 6.2 Cavity reflection assisted $\text{Si}_3\text{N}_4$ laser

Here we present a compact  $\text{Si}_3\text{N}_4$  hybrid laser based on high-confinement waveguides in order to attain a low-loss, small footprint integrated laser cavity. We leverage our recently demonstrated  $\text{Si}_3\text{N}_4$  waveguides with propagation losses as low as 0.8 dB/m at 100  $\mu\text{m}$  radius [21], achieved by addressing sources of loss and confining the optical mode. Such high-confinement  $\text{Si}_3\text{N}_4$  waveguides also compare favorably to silicon, which has only reached losses of 10-50 dB/m at compact dimensions [98, 106] or 3 dB/m at 5 mm size [107].

We use a high quality factor ( $Q$ )  $\text{Si}_3\text{N}_4$  microring resonator as a combined

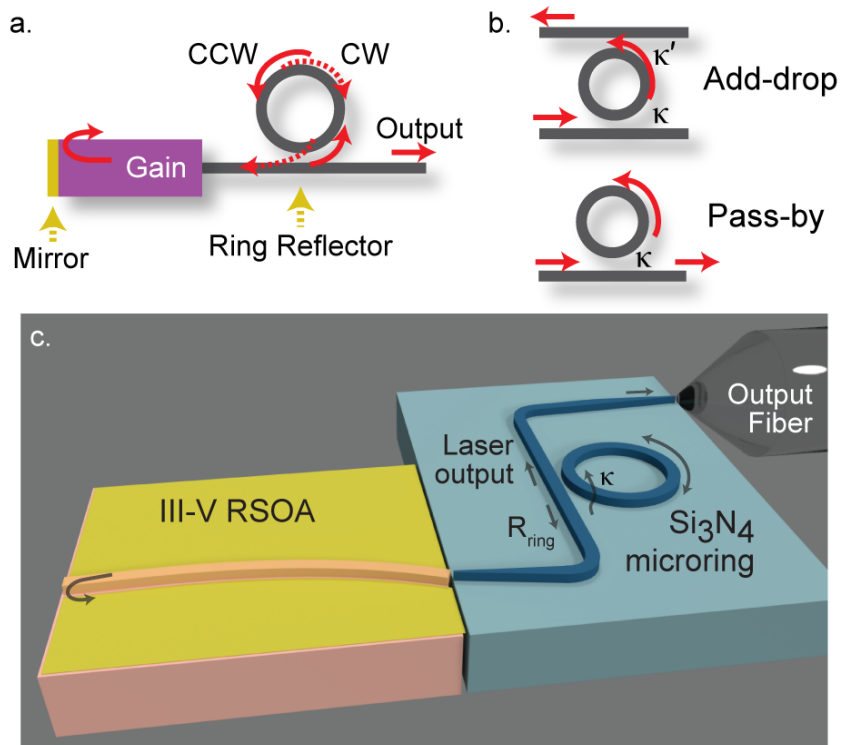


Figure 6.1: (a) Schematic of our laser. The ring acts as a partial reflector by taking advantage of the coupling of the counter clockwise (CCW) propagating mode to the clockwise (CW) mode, which reflects light back into the cavity. (b) Comparison of the pass-by configuration used here (bottom), which leads to a high loaded  $Q$ , with the commonly used add-drop configuration (top), which often leads to a lower loaded  $Q$ . (c) Schematic of our laser cavity design (not to scale).

filter, output mirror, and propagation delay to achieve linewidth reduction. The laser consists only of a gain section and two mirrors, one of which is the high- $Q$  microring, as shown in Figure 6.1a. The ring resonator acts as a partial reflector as well as a tunable filter, by taking advantage of the coupling between the counter-clockwise (CCW) and the clockwise (CW) propagating modes [10,108]. Note that this effect was first used in fiber [10] and later free-space lasers [109], while we now demonstrate that it can be applied to planar resonators. The CW and CCW modes couple to each other when minor scattering points along

the cavity dominate the losses, as opposed to material absorption or out-of-plane scattering. When the  $Q$  is sufficiently high, power builds up in the cavity such that light can fully couple from CW to CCW or the reverse, resulting in an effective reflection. The amount of reflection is controlled by the coupling strength between the two modes and by the  $Q$  relative to the coupling strength  $\kappa$  between the input waveguide and the ring [108]. Because the reflection has a narrow bandwidth, the microring also filters the cavity modes. Tuning the ring's resonance allows the lasing wavelength to be selected.

To achieve a narrow laser linewidth, we utilize the high- $Q$  microring as external cavity feedback and take advantage of the long effective length of the ring. In semiconductor lasers, spontaneous emission events affect carrier density, resulting in refractive index and phase changes, thus broadening the linewidth [16]. An external cavity reduces this linewidth broadening by making the lasing frequency less sensitive to phase and gain changes [1]. Because frequency-dependent feedback contributes to linewidth reduction, the narrow-band reflection from the ring in our design makes an ideal external cavity. The low propagation loss and coupling strength of the microring effectively increases the cavity length. The effective length  $L_{eff}$  of the ring is given by

$$L_{eff} = \frac{\lambda}{\beta} \left| \frac{d\phi}{d\lambda} \right| \quad (6.1)$$

where  $\beta$  is the propagation constant [110]. At critical coupling, this becomes

$$L_{eff} = \frac{1 - \kappa}{\kappa} L \quad (6.2)$$

To achieve a large  $L_{eff}$ , we operate close to critical coupling with low coupling  $\kappa$ . The  $L_{eff}$  provides the linewidth reduction benefits of a physically long external cavity, without the need for centimeters of on-chip space. Note that demonstrations using microcavities in lasers have previously achieved sub-kilohertz

linewidths using feedback from  $\text{MgF}_2$  or silica microsphere cavities with  $Q$ 's on the order of  $10^9$  to achieve ultra-narrow resonances [111,112], but such materials are not planar and therefore not easily integrated on silicon substrates.

To ensure that low-loss waveguides translate to a high loaded quality factor ( $Q_L$ ) and narrow linewidth, we use a single waveguide to couple light in and out of the ring in contrast to the more commonly used add/drop configuration formed by coupling the ring to two waveguides (see Figure 6.1b, top). In a single waveguide pass-by configuration (Figure 6.1b, bottom), the coupling  $\kappa$  must match the roundtrip losses  $\alpha L$  in order to achieve critical coupling so that power builds up in the ring. We operate the ring in the undercoupled regime, where  $\kappa$  is slightly less than  $\alpha L$ . This leads to a high  $Q_L$  close to the intrinsic  $Q_0$ , where  $Q_L = Q_0/(1 + \kappa/\alpha L)$ . In contrast, the commonly used add-drop ring configuration shown in Figure 6.1b (top) must meet the condition  $\kappa = \kappa' + \alpha$  for critical coupling. In this case the coupling ( $\kappa = \kappa'$ ) must be strong compared to  $\alpha L$  to drop the power, and so even a low-loss platform may be limited to a  $Q_L$  on the order of  $10^5$ . Therefore, the pass-by configuration used here is preferred to achieve a high  $Q_L$  in the  $10^7$  range, which takes advantage of  $\text{Si}_3\text{N}_4$ 's low loss.

We form the laser by edge coupling a III-V reflective semiconductor optical amplifier (RSOA) to the  $\text{Si}_3\text{N}_4$  cavity (Figure 6.1c). The RSOA is commercially available (Thorlabs SAF1126) and provides high gain across a 40 nm range near 1550 nm, for which we design the laser cavity. The RSOA has a reflection of 93% at one facet and is anti-reflection coated on the other, which is coupled to a tapered  $\text{Si}_3\text{N}_4$  waveguide. The taper is fabricated at an angle with respect to the facet to avoid reflections. We use a 3-axis stage to align the RSOA to the silicon chip facet (Figure 6.2a) and estimate a coupling loss of 8.5 dB. This

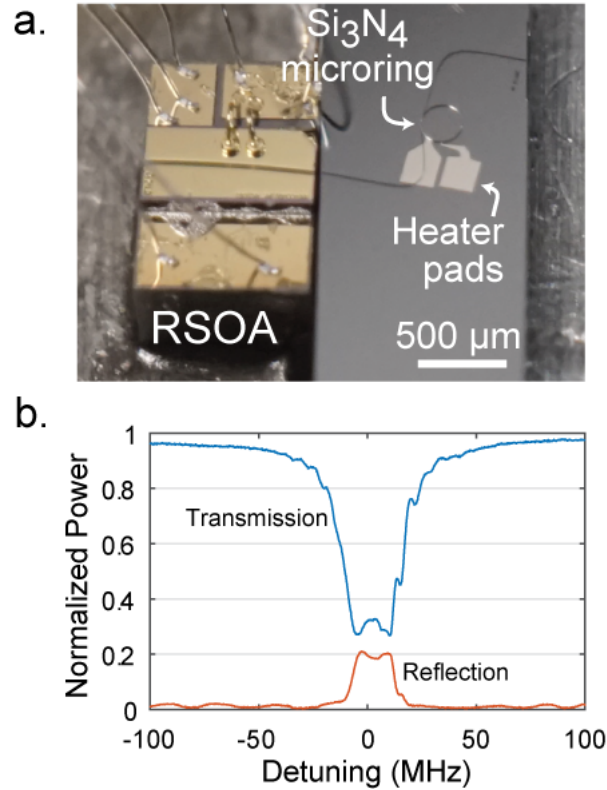


Figure 6.2: (a) Photograph of the coupled chips. Wirebonds are used to supply current to the RSOA, and needle probes (not shown) are used to apply voltage to the heater on the  $\text{Si}_3\text{N}_4$  chip. (b) Measured transmission and reflection spectra of  $\text{Si}_3\text{N}_4$  microring resonator. The degeneracy of the CW and CCW modes causes the resonance splitting (double peak), which is accounted for in the resonance fitting.

can be improved by reducing the separation in air between the two chips to avoid diffraction, as coupling loss below 1 dB has recently been demonstrated in hybrid lasers [98]. The  $\text{Si}_3\text{N}_4$  waveguide has a length of  $950\ \mu\text{m}$  before coupling to a  $120\ \mu\text{m}$  radius microring resonator. We use a coupling gap of  $480\ \text{nm}$  and wide waveguides with cross-section  $730 \times 1800\ \text{nm}$  to localize the optical mode. The output waveguide is then coupled to a lensed fiber to measure the output of the laser.

We fabricate the  $\text{Si}_3\text{N}_4$  cavity using the process described in [21] to attain

low loss waveguides. We grow 4  $\mu\text{m}$  of  $\text{SiO}_2$  on a silicon wafer and then deposit  $\text{Si}_3\text{N}_4$  using low-pressure chemical vapor deposition (LPCVD). The wafer is annealed to remove hydrogen impurities. We then pattern the waveguides using electron beam lithography, and next we etch the waveguides and clad the devices with  $\text{SiO}_2$ . Finally, we pattern and lift-off sputtered platinum heaters over the microring in order to tune the resonance.

### 6.3 Resonator and laser characterization

We measure the quality factor of the  $\text{Si}_3\text{N}_4$  microring to be over  $10^7$ , which in the laser configuration corresponds to an effective length of over 1 meter. Using the measurements of the transmission of the  $\text{Si}_3\text{N}_4$  chip alone, shown in Figure 6.2b, we fit the microring resonance bandwidth to an 18 MHz Lorentzian, indicating a  $Q_0$  of  $1.34 \times 10^7$ , a  $Q_L$  of  $1.05 \times 10^7$ , and an ultra-low propagation loss of 2.2 dB/m. We use a circulator to measure the reflection spectrum of the microring, which is shown in Figure 6.2b. On resonance there is a strong 20% reflection. Using the  $Q_L$  derived from the transmission, we determine  $\kappa$  to be  $1.1 \times 10^{-4}$ . From Equation 6.1 and the transmission fitting,  $L_{eff}$  is calculated to be 1.17 m, achieved in an area of about  $4.5 \times 10^{-2} \text{ mm}^2$  on the chip.

We observe single-mode lasing and greater than 1 mW of output power when pumping the assembled laser above threshold. The output of the laser is sent to an optical spectrum analyzer (OSA) to characterize the lasing spectrum, shown in Figure 6.3a. The laser's side mode suppression ratio (SMSR) is 41 dB at 1550 nm. Figure 6.3b shows the laser's output power versus pump current. The threshold current is 52 mA, above which the slope efficiency is 48 mW/A. The

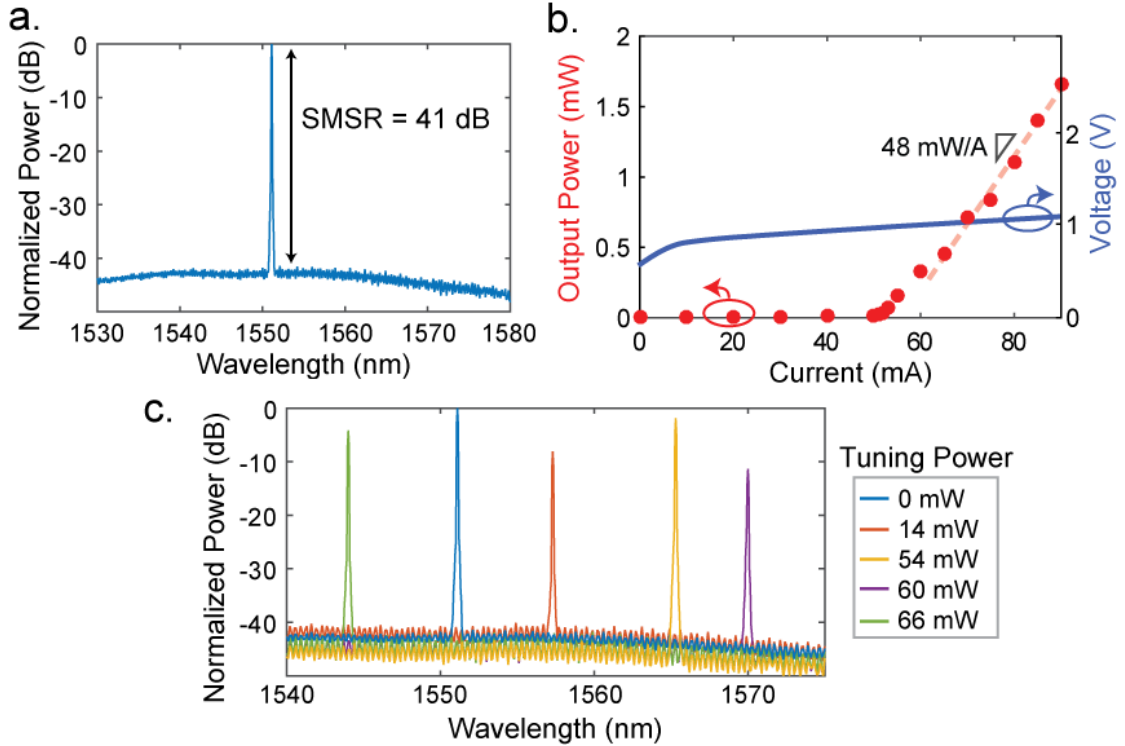


Figure 6.3: (a) Measured spectrum of laser output showing single-mode operation and high side mode suppression ratio (SMSR). (b) Measured uncooled laser output power at room temperature. (c) Measured spectra showing lasing across a wide range of wavelengths. By adjusting the voltage applied to the micro-heater integrated on the ring, lasing is obtained at discrete wavelengths within a 27 nm range.

laser, which is uncooled, has a maximum observed output power of 1.66 mW at 90 mA, with a wall-plug efficiency of 1.7%. In order to confirm that the ring is acting as an output mirror according to design, we also couple the RSOA to an identical  $\text{Si}_3\text{N}_4$  waveguide, but with no on-chip ring, and confirm that it does not lase simply due to facet reflections. Figure 6.3c shows that as we tune the resonance of the ring using the integrated heaters, we observe lasing at wavelengths from 1544 nm 1571 nm, a wide 27 nm range, although the tuning, while repeatable, does not continuously cover the whole tuning range.

We measure a 13 kHz linewidth from the laser using a delayed self-heterodyne (DSH) setup. The linewidth is narrower than the resolution of our OSA, so we perform DSH because it allows measurement of narrow linewidths without the need for a reference laser at a nearby frequency [113]. Figure 6.4a shows our experimental setup. We send the laser output to a fiber interferometer in which one path has a delay of 12 km, which is longer than the laser coherence length and allows reliable measurements for linewidths down to several kHz. To further improve the confidence of our setup, we also independently measured the linewidth of a commercial laser and verified it to be equal to the specified 2.4 kHz linewidth. Figure 6.4b shows the measured beat note of our integrated laser using this setup. We fit a Lorentzian to the beat note's tails, corresponding to a linewidth of 13 kHz, which is among the narrowest demonstrated in integrated lasers with widely adjustable wavelength.

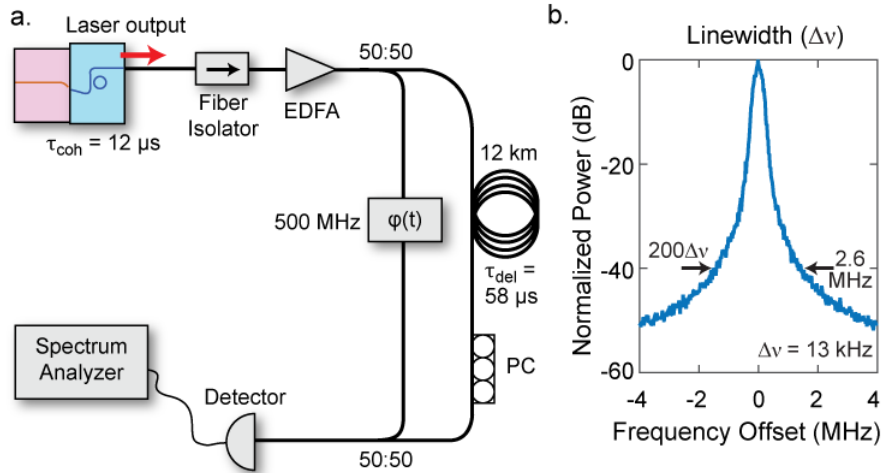


Figure 6.4: (a) Delayed self-heterodyne (DSH) test set-up. EDFA: Erbium Doped Fiber Amplifier. PC: Polarization Controller. (b) Measured DSH beat note in radio frequency (RF) spectrum analyzer. The -40 dB width equals 200 times the Lorentzian linewidth, which is found to be 13 kHz here. The resolution bandwidth used is 10 kHz with 325 ms sweep time.

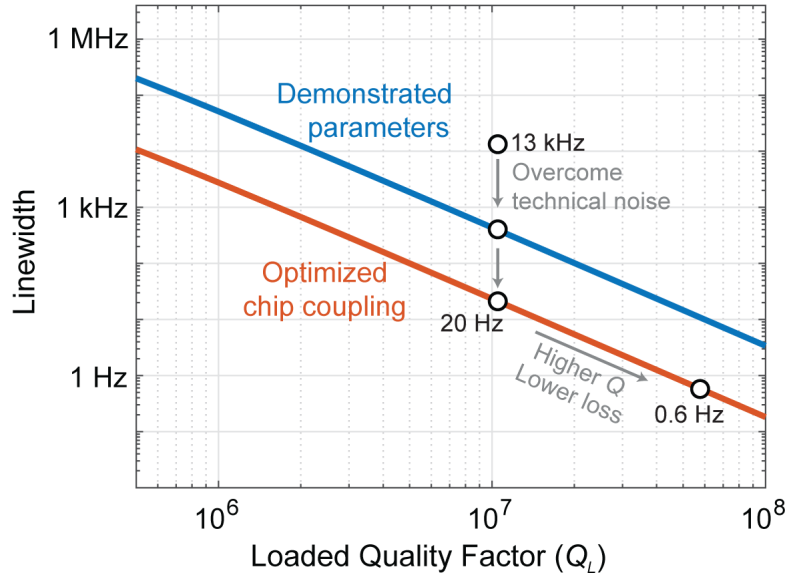


Figure 6.5: Calculated linewidth versus  $Q_L$ , with current cavity parameters (blue), and improved coupling (red). Laser cavities based on  $\text{Si}_3\text{N}_4$  have the potential to reach beyond the demonstrated 13 kHz linewidth and produce sub-Hz linewidths.

## 6.4 Further linewidth reduction

According to our analysis, a linewidth as narrow as 400 Hz should be achievable if we overcome technical noise, and even narrower linewidths are possible with reasonable improvements to the  $Q$  and the coupling loss between the RSOA and chip. Using the experimentally demonstrated cavity parameters, we plot the predicted linewidth as a function of  $Q_L$  in Figure 6.5, using the Schawlow-Townes formula with Henry's linewidth broadening factor [16]. For the  $Q_L$  of  $1.05 \times 10^7$  in our case, the expected linewidth is 400 Hz, indicating that in our experiment we are likely limited by technical noise, such as vibrations or noise from the power supply driving the RSOA. Permanent bonding of the two chips or using a lower noise pump current supply could help reach this prediction. We also plot in Figure 6.5 the achievable linewidths from optimized coupling of

the gain chip to the silicon chip, which we assume can improve to 1 dB loss [98] and 10 mW output power. We see that this optimization is expected to yield a linewidth of 20 Hz for the same  $Q_L$ , and below 1 Hz for a  $Q_L$  of  $5.8 \times 10^7$ . This  $Q_L$  was achieved in  $\text{Si}_3\text{N}_4$  in [21]. Such ultra-narrow linewidths would be especially desirable for metrology applications. It is important to note that at these levels, factors such as acoustic noise and Brownian motion may also become limiting factors [112], but using a fully integrated platform aids one in addressing those challenges.

## 6.5 Conclusion

In summary, we have demonstrated a compact  $\text{Si}_3\text{N}_4$  laser cavity with narrow linewidth. Using a highly confined optical mode enables both compact bends and ultra-low loss in  $\text{Si}_3\text{N}_4$  waveguides. Our design leverages the narrowband reflection generated by backscattering in a high- $Q$   $\text{Si}_3\text{N}_4$  microring to act as an output mirror and to provide laser linewidth reduction. The narrow resonance of the ring allows the laser to achieve single-mode lasing with a 41 dB SMSR. We have shown lasing at discrete wavelengths across a 27 nm range. A larger continuous tuning range should be possible with additional cavity control that would include a tunable coarse filter. Further, an additional heater to tune the cavity phase would allow for more consistent output power while tuning. The laser has a measured 13 kHz linewidth, due to a high  $Q$  of over  $10^7$  and low  $\kappa$  coupling design which result in an effective length of over 1 m in a sub-mm area. In addition to the C-band (1550 nm) laser demonstrated here, a design using amplifiers at 1310 nm or even visible wavelengths would also be possible due to  $\text{Si}_3\text{N}_4$ 's broad transparency. Approaches using heterogeneous bonding [93, 94]

rather than edge coupling should be compatible with this novel cavity architecture as well. Further enhancements in cavity parameters could enable sub-Hz linewidths on a  $\text{Si}_3\text{N}_4$  platform, which may otherwise be far beyond the reach of silicon.

## CHAPTER 7

### FULLY INTEGRATED FREQUENCY COMB SOURCE

Optical frequency combs are broadband sources that offer mutually-coherent, equidistant spectral lines with unprecedented precision in frequency and timing for an array of applications [114–122]. Kerr frequency combs in microresonators require a single-frequency pump laser and have offered the promise of highly compact, scalable, and power efficient devices. Here, we realize this promise by demonstrating the first fully integrated Kerr frequency comb source through the use of extremely low-loss silicon nitride waveguides that form both the microresonator and an integrated laser cavity. Our device generates low-noise soliton-modelocked combs spanning over 100 nm using only 98 mW of electrical pump power. Our design is based on a novel dual-cavity configuration that demonstrates the flexibility afforded by full integration. The realization of a fully integrated Kerr comb source with ultra-low power consumption brings the possibility of highly portable and robust frequency and timing references, sensors, and signal sources. It also enables new tools to investigate the dynamics of comb and soliton generation through close chip-based integration of microresonators and lasers.

#### 7.1 Introduction

Frequency combs based on chip-scale microresonators offer the potential for high-precision photonic devices for time and frequency applications in a highly compact and robust platform. By pumping the microresonator with a single-frequency pump laser, additional discrete, equidistant frequencies are generated through parametric four-wave mixing (FWM; see Chapter 4), resulting in

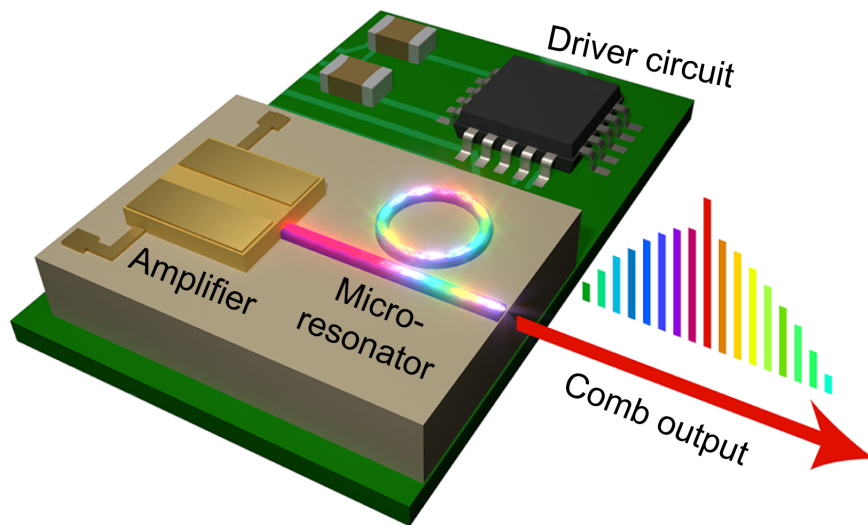


Figure 7.1: Concept illustration of an integrated Kerr comb source with an on-chip amplifier and microresonator.

a Kerr frequency comb [22, 123]. Under suitable conditions temporal cavity solitons can be excited, which results in stable, low-noise combs with ultra-precise spacing [26, 124–127]. Many applications require such tight frequency and timing stability, including spectroscopy [114–116], low-noise microwave generation [117, 118], atomic clocks [119], lidar [120, 128], and telecommunications [121, 122]. Extensive research has explored different microresonator platforms to generate frequency combs for these applications [7, 21, 129–133].

While one of the most compelling advantages for microresonator combs is the potential for the pump source and the microresonator to be fully integrated (Figure 7.1), previous demonstrations using integrated resonators have relied on external pump lasers that are typically large, expensive, and power hungry, preventing applications where size, portability and low power consumption are critical. Power-efficient integrated lasers have been developed using silicon laser cavities with bonded or attached III-V gain sections [97, 98, 134, 135],

but losses in these silicon waveguides make comb generation impractical at low power. On the other hand, silicon nitride ( $\text{Si}_3\text{N}_4$ ) microresonators were recently demonstrated with record low parametric oscillation thresholds [21] due to the high quality factors ( $Q > 3 \times 10^7$ ), high nonlinearity ( $n_2 \sim 2.4 \times 10^{19} \text{ m}^2\text{W}^{-1}$ ), and small mode volume (ring radius  $\sim 100 \text{ }\mu\text{m}$ ). Additionally, due to  $\text{Si}_3\text{N}_4$ 's high index of refraction ( $n \sim 2.0$ ) and low loss, compact, tunable  $\text{Si}_3\text{N}_4$  laser cavities with narrow linewidth have been demonstrated [136,137].  $\text{Si}_3\text{N}_4$  is a common complementary metal oxide semiconductor (CMOS)-compatible deposited material that can be fabricated at wafer scale, and the combination of efficient comb generation and available integration of active devices make it an ideal platform for complete integration of optical frequency combs.

## 7.2 Integrated Kerr comb source

Here we demonstrate a Kerr comb source on a fully integrated  $\text{Si}_3\text{N}_4$  platform, using a compact, low-power, electrically-pumped source. In our approach (Figure 7.2), a gain section based on a III-V reflective semiconductor optical amplifier (RSOA) is coupled to a  $\text{Si}_3\text{N}_4$  laser cavity, which consists of two Vernier microring filters for wavelength tunability and a high- $Q$  nonlinear microresonator (Figure 7.2a). The nonlinear microresonator serves two purposes. First, it generates a narrowband back-reflection due to Rayleigh scattering [111], effectively serving as an output mirror of the pump laser cavity, as we previously demonstrated [136]. Second, the microresonator generates a frequency comb through parametric FWM. In this way, the comb generation and pump laser are inherently aligned, a configuration that was previously explored using resonators in fiber laser cavities with fiber amplifiers [138,139]. Fully integrating the comb

source allows the flexibility to use such a configuration, avoiding the typical chain of discrete components found in all previous Kerr comb demonstrations. Figure 7.2b shows the assembled millimeter-sized comb source, which has only electrical inputs and an optical output.

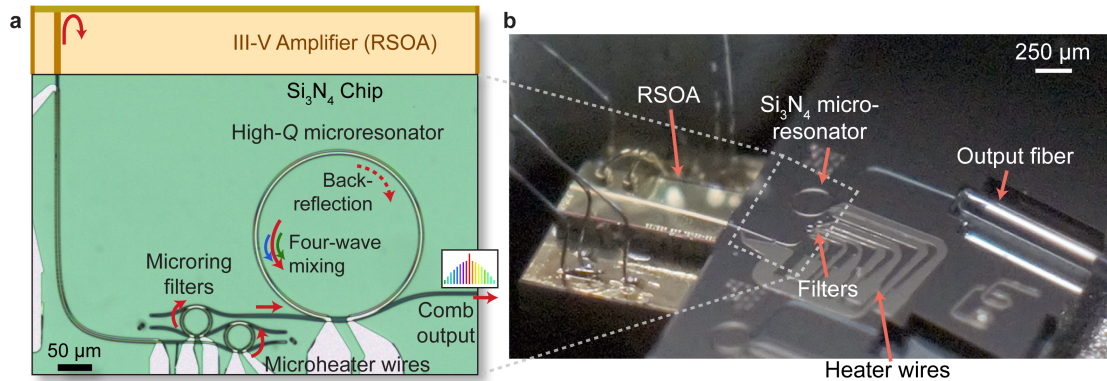


Figure 7.2: (a) Microscope image and diagram of integrated comb source, including laser cavity and nonlinear microresonator for comb generation. The amplifier waveguide provides electrically-pumped optical gain and includes a reflective facet on one end, while the opposite side is coupled to the Si<sub>3</sub>N<sub>4</sub> portion of the laser cavity. The microring filters are tunable using integrated microheaters. The larger microresonator generates a partially reflected beam to form a second effective mirror of the laser cavity. This microresonator also has a high  $Q$  to enable FWM and comb generation. (b) Photograph of the fully integrated comb source. The RSOA is edge-coupled to the Si<sub>3</sub>N<sub>4</sub> chip and supplied with electric current via wirebonds, while the comb output is measured using an optical fiber.

We design the Si<sub>3</sub>N<sub>4</sub> laser cavity to ensure tunable, single-mode lasing and provide sufficient pump output power for comb generation in the nonlinear microresonator. The lasing wavelength is controlled by the alignment of the two microring Vernier filters [98], which are in turn aligned with one of the modes of the larger microresonator shown in Figure 7.2a. The filters' radii are 20 μm and 22 μm, corresponding to free spectral ranges (FSR) of 1.18 THz and 1.07 THz,

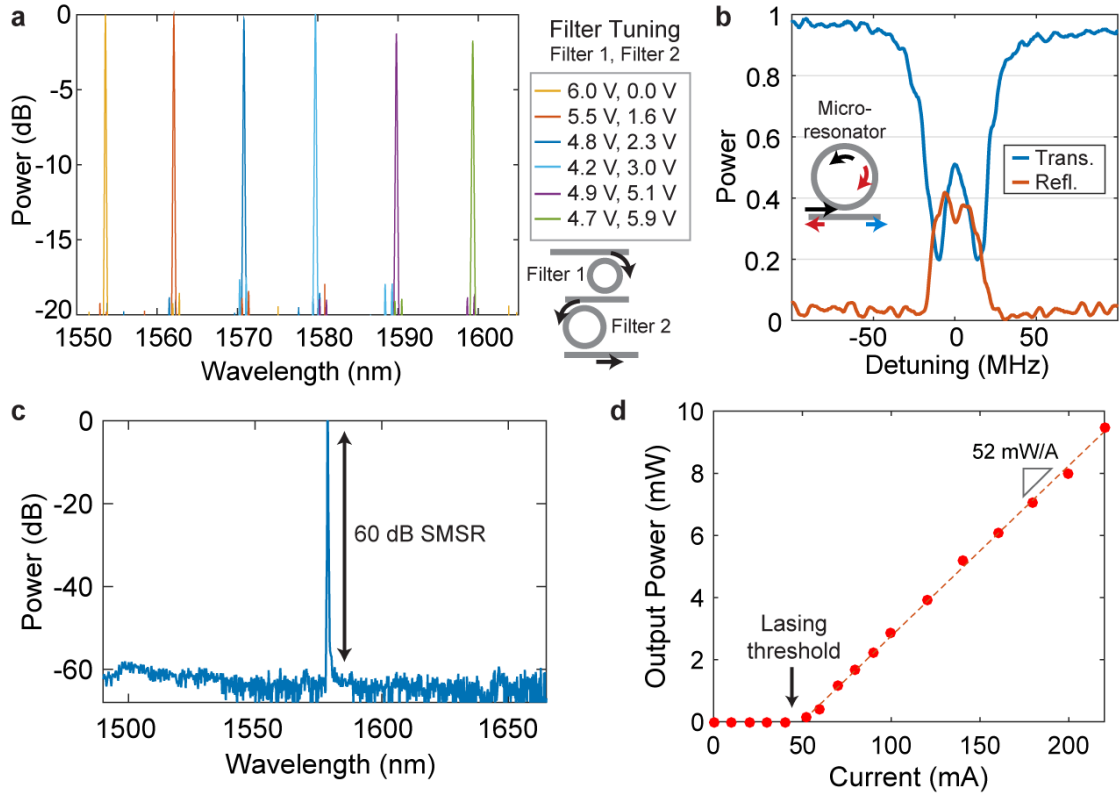


Figure 7.3: (a) Measured transmission spectrum for the Vernier filter rings. By adjusting the voltage applied to the microheaters, the filters relative detuning is adjusted and a single transmission wavelength is selected. (b) Measured optical transmission and reflection spectra (normalized) of the high- $Q$  microresonator. The 32-MHz resonance bandwidth reveals a  $Q$  of  $8 \times 10^6$ . The narrowband reflection is generated by coupling via Rayleigh scattering between counter-propagating beams in the ring, which is apparent due to the resonance splitting observed from these degenerate beams. (c) Laser output spectrum showing single-mode lasing with over 60 dB side-mode suppression ratio (SMSR). (d) Output optical power of laser versus pump current at 1580 nm.

respectively, which results in transmission at only a single frequency when the filters are aligned. Their resonance positions can be widely tuned using integrated resistive microheaters, as shown in Figure 7.3a. The filters' transmission bandwidth is designed to have a full-width half-maximum (FWHM) of 15 GHz

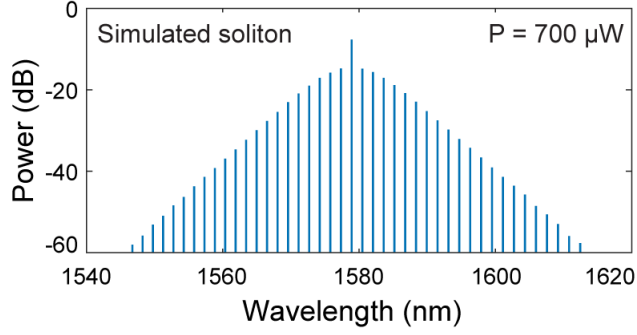


Figure 7.4: Simulated optical spectrum of soliton generated with 700  $\mu\text{W}$  optical pump power. The microresonator dimensions used in the model are  $730 \times 1800$  nm with a radius of 120  $\mu\text{m}$ , corresponding to a 194 GHz FSR (pulse repetition rate).

by ensuring strong coupling to the add and drop waveguides with a 5  $\mu\text{m}$  coupling length. The optical gain in the laser cavity comes from electrical pumping of the III-V waveguide on the RSOA, which is coupled to the  $\text{Si}_3\text{N}_4$  cavity on one end and strongly reflects at the opposite end. The output coupler of the laser cavity is a 120  $\mu\text{m}$  radius microresonator with a measured reflection of 40% on resonance (due to coupling between counter-propagating circulating beams resulting from Rayleigh scattering [136]), as shown in Figure 7.3b. This level of reflection allows for high laser output power due to the high roundtrip gain of the RSOA. The measured transmission spectrum of the microresonator (Figure 7.3d) corresponds to an intrinsic  $Q$  of  $(8.0 \pm 0.8) \times 10^6$ . Based on this  $Q$  and the anomalous group-velocity dispersion for the  $730 \times 1800$  nm waveguide, simulations based on the Lugiato-Lefever equation [140] indicate that a soliton-state frequency comb can be generated at 700  $\mu\text{W}$  of pump power (Figure 7.4).

The III-V RSOA gain chip used here is commercially available from Thorlabs (SAF 1126) and provides broad gain near 1550 nm. One side has 93% reflection and the other side is anti-reflection coated. This second side is coupled to the  $\text{Si}_3\text{N}_4$  chip with the waveguides angled relative to the facets to further prevent

reflections [136]. The  $\text{Si}_3\text{N}_4$  chip is polished up to the end of a tapered 280-nm wide waveguide which is simulated to have less than 1 dB coupling loss to the mode of the RSOA waveguide. The two chips are attached and aligned using three-axis stages with micrometers. We measure an experimental 2 dB coupling loss. The RSOA is wirebonded to an electrical printed circuit board (PCB) for supplying the pump current from either a Keithley 2400 SourceMeter or a AAA battery with a tunable potentiometer. The  $\text{Si}_3\text{N}_4$  chip's microheaters are connected to pads and interfaced with a DC wedge probe (GGB Industries) and controlled by a DAC (Measurement Computing). The  $\text{Si}_3\text{N}_4$  waveguide output is formed as an inverse-taper to edge-couple to a lensed single-mode fiber.

The  $\text{Si}_3\text{N}_4$  devices are fabricated [21] by first growing 4  $\mu\text{m}$  of  $\text{SiO}_2$  on a crystalline silicon wafer using thermal oxidation to form the bottom cladding of the waveguides. Then 730 nm of  $\text{Si}_3\text{N}_4$  is deposited using low pressure chemical vapor deposition (LPCVD). The wafer is annealed in two stages to remove hydrogen impurities. The waveguides are then patterned using electron beam lithography and etched using  $\text{CHF}_3$  plasma etching. The waveguides are clad with 2  $\mu\text{m}$   $\text{SiO}_2$ . The microheaters are placed over the waveguides using 100 nm of sputtered platinum (with a titanium adhesion layer) and lift-off patterning.

### 7.3 Laser characterization

We show lasing with up to 9.5 mW output optical power using the integrated  $\text{Si}_3\text{N}_4$  laser. In order to characterize the laser, we first operate the microresonator slightly detuned from resonance to ensure that only lasing occurs and a

frequency comb is not generated. We observe lasing with over 60 dB side-mode suppression ratio (SMSR) (Figure 7.3c). As shown in Figure 7.3d, the lasing threshold is 49 mA, with a slope efficiency of 52 mW/A. The maximum on-chip output power of 9.5 mW is obtained at 277 mW (220 mA) electrical pump power. This corresponds to a 3.4% wall-plug efficiency. Additionally, we measure a narrow laser linewidth of 40 kHz using the delayed self-heterodyne method [136]. The laser output is sent to an interferometer with one path delayed by 12 km of fiber (corresponding to a delay of 58  $\mu$ s). The other path is phase modulated at 300 MHz. The resulting beat signal is measured on an electrical spectrum analyzer (Agilent E4407B) and a 40 kHz Lorentzian linewidth is determined. The relatively high output power and narrow linewidth is competitive with those of many bulk pump lasers, yet is significantly more compact.

## 7.4 Comb and soliton generation

Using our novel cavity design we generate a Kerr comb spanning 100 nm and achieve a mode-locked, single-soliton state with less than 100 mW electrical pump power consumption, enabling battery-operation applications. At 1.1 mW optical output laser power (corresponding to 78 mW electrical power), new frequency components begin to appear due to FWM in the microresonator. We then monitor the comb formation as the microresonator is tuned into the lasing mode's wavelength using a fixed electrical pump power of 130 mW. In order to generate the comb, the microresonator is roughly aligned with the filter rings such that lasing occurs at 1579 nm with 2.5 mW output power (Figure 7.5a). As the microresonator is tuned into resonance, greater circulating power leads to comb formation, accompanied by high RF noise (Figure 7.5b). Tuning the

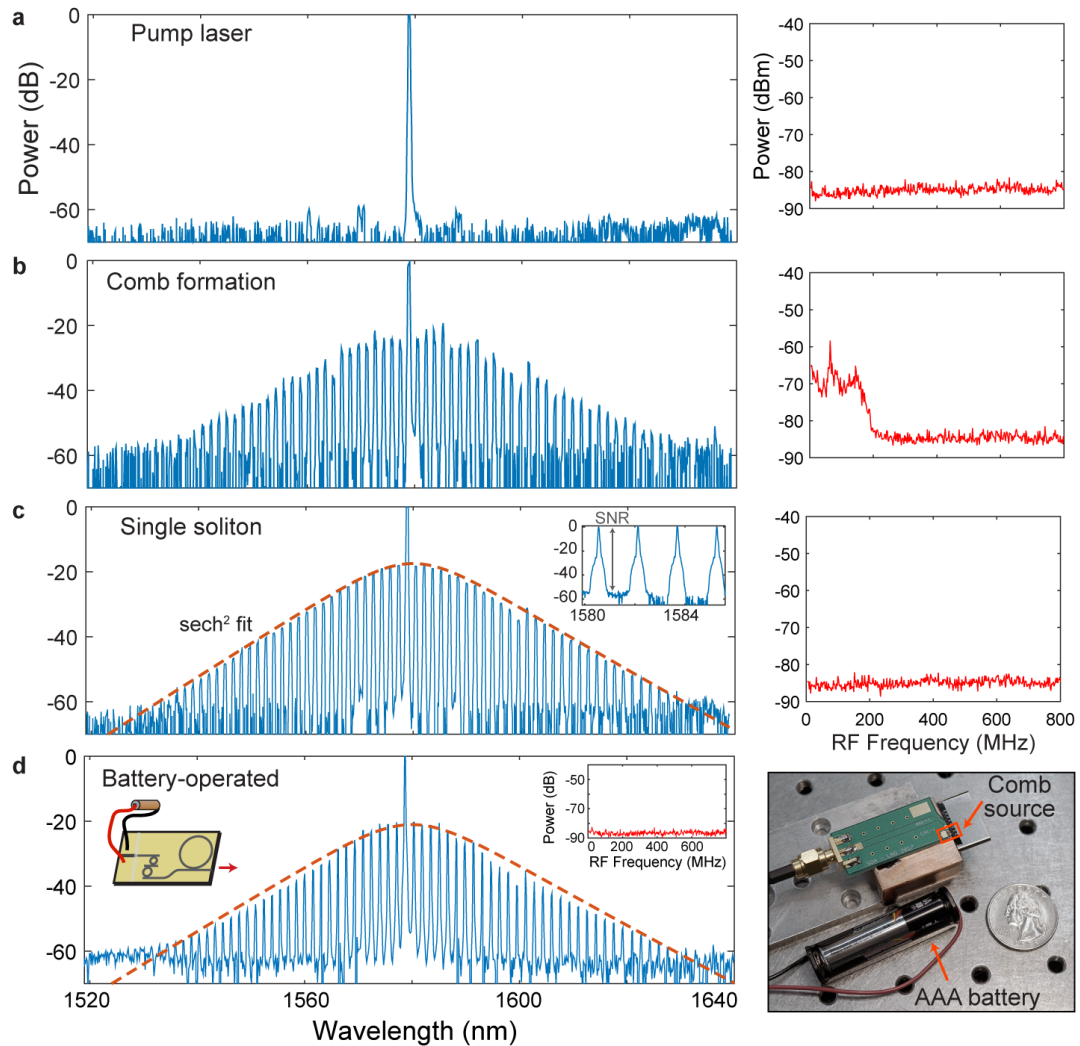


Figure 7.5: (a-c) Spectra of output from comb source as measured by an optical spectrum analyzer (OSA) at varying stages of comb generation with corresponding RF spectra. A current supply provides 130 mW electrical pump power. (d) Frequency comb matching soliton profile generated with a AAA battery supplying pump power of 98 mW. Inset: RF spectrum showing low-noise state. Right: Photograph of integrated comb source with a printed circuit board and the battery.

resonance further results in stable combs with smooth spectral envelopes characteristic of temporal cavity solitons. We measure a single-soliton state (Figure 7.5c) with an associated drop in RF noise. Once generated, the soliton ex-

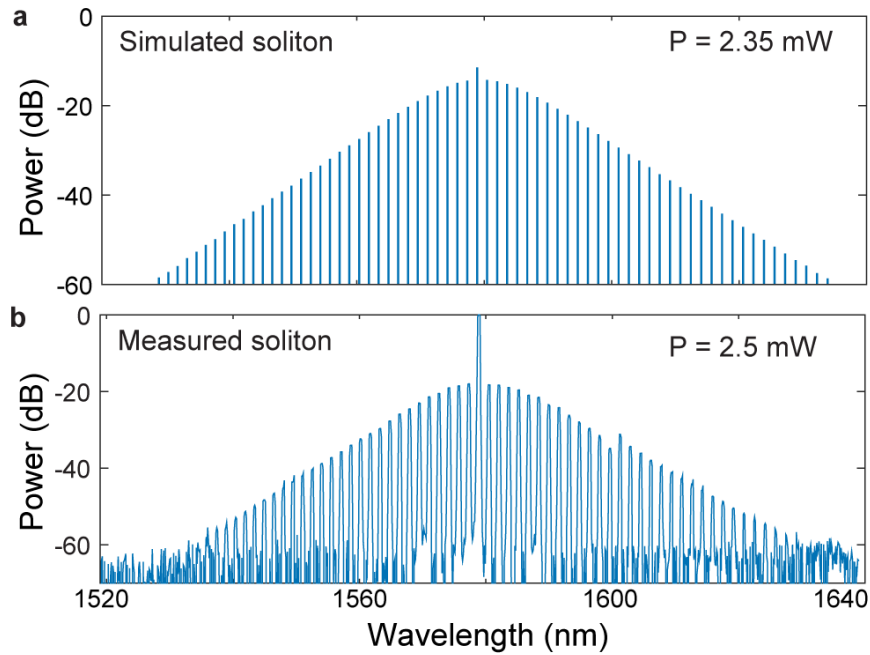


Figure 7.6: (a) Simulation of single-soliton comb generated with 2.35 mW pump power. The microresonator dimensions used in the model are  $730 \times 1800$  nm with a radius of  $120 \mu\text{m}$ , corresponding to a 194 GHz FSR (pulse repetition rate). (b) Optical spectrum of measured single-soliton comb (from Figure 7.5c) generated with 2.5 mW pump power. The  $\text{sech}^2$  profile matches well with the simulated comb at slightly higher pump power.

hibits stable behavior without feedback electronics or temperature control, with no visible changes in the optical spectrum or output power until intentionally detuned. The signal-to-noise ratio of the central comb lines is approximately 50 dB, which is useful for spectroscopy applications [116]. We additionally show battery-operation of the comb source by supplying the pump current using a standard AAA battery. At 98 mW of electrical power from the battery, we measure 1.3 mW output optical power and a comb matching the single-soliton profile (Figure 7.5d). These results represent unprecedented low power consumption for generating Kerr frequency combs and solitons with an integrated microresonator.

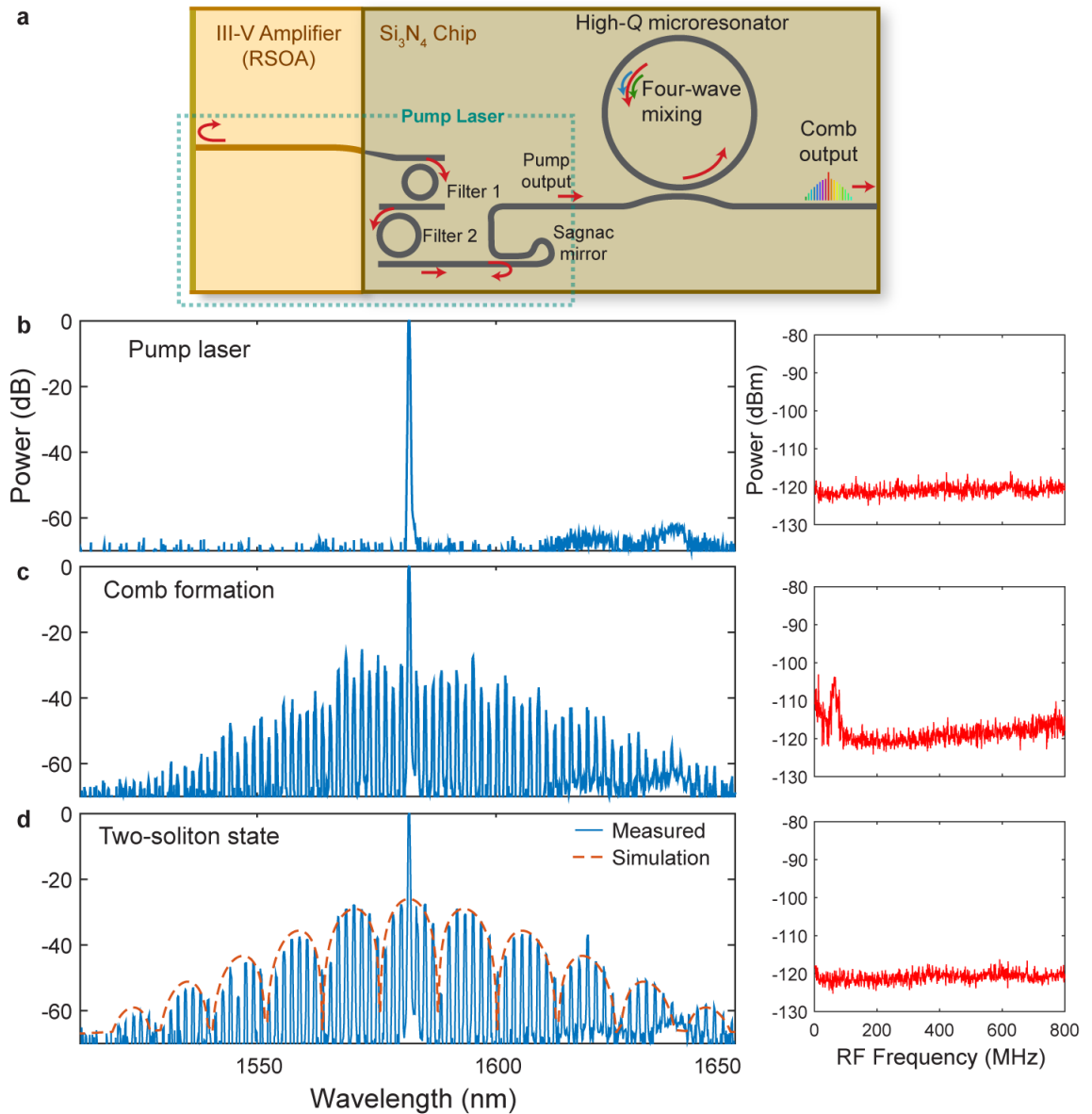


Figure 7.7: (a) Schematic of the modular comb source configuration, based on the typical external pump scheme. Here the integrated laser is distinct from the nonlinear microresonator, with a Sagnac loop mirror serving as the laser output coupler. (b-d) Optical output spectra at varying stages of comb generation with corresponding RF spectra.

In order to show the versatility of this platform, we also demonstrate a more traditional but fully integrated configuration where the comb is generated in a microresonator that is not also used to generate the laser. In this second design, shown in Figure 7.7a, the pump laser is distinct from the high- $Q$  microresonator. The Vernier filters and RSOA function the same as the first design, while a Sagnac loop mirror is included to serve as the output coupler with approximately 20% reflection. Since this mirror has a broadband reflection, tunable lasing can take place independent of the resonance position of the comb microresonator. With the microresonator fully off-resonance, we measure single-mode lasing at 1582 nm with 4.9 mW output power and over 60 dB SMSR (Figure 7.7b) at 162 mW electrical pump power. By tuning the microresonator into resonance with the laser wavelength, we can generate a frequency comb spanning 110 nm (Figure 7.7c). By further tuning into resonance such that the laser is effectively red-detuned, we observe a multiple-soliton state frequency comb spanning over 130 nm with the characteristic drop in RF noise (Figure 7.7d). We model a two-soliton state comb and obtain a profile closely matching that of the experimental comb (Figure 7.7d). The comb generation process in this second design is directly analogous to previous Kerr comb experiments [126, 127], but this demonstration brings a high level of integration which affords greater flexibility in laser design and reduced power consumption.

## 7.5 Discussion

This demonstration of the first fully integrated Kerr frequency comb source opens the door to countless new applications previously limited by the size and power requirements of discrete comb systems. The high level of integra-

tion enables new flexibility in designing the pump laser for generating the frequency comb, as evidenced by the two designs demonstrated here, consisting of an inherently aligned comb source enabled by a feedback reflection and a traditional modular configuration. Furthermore, the platform used here is CMOS-compatible for wafer-scale fabrication of robust, fully integrated photonic chips, potentially enabling wide deployment of precision references and sensors. The realization of a mode-locked Kerr comb on an integrated platform presents opportunities in many fields that rely on the precision and stability of frequency combs and solitons, including sensing, metrology, communications, and waveform generation. The low power consumption of the platform enables battery-powered and mobile systems, no longer relying on external lasers, movable optics, and laboratory set-ups.

## CHAPTER 8

### DISCUSSION AND FUTURE DIRECTIONS

The work presented here has shown the wide versatility of integrated photonic devices. Silicon photonics provides tunability of the shape and path of light, and microresonators are critical for precise spectral control and further enhancement of light-matter interactions. The novel devices demonstrated here push the capabilities of using silicon photonics for optical communications, signal generation, sensing, and metrology.

#### 8.1 Multimode silicon photonics

Multimode silicon photonics continues to attract research attention for its potential to expand bandwidth density of integrated waveguides [141, 142]. On-chip mode-division multiplexing (MDM) may first bolster MDM and space-division multiplexing (SDM) in fiber. There is a strong motivation to increase capacity in fiber because single-mode fiber (SMF) that has reached the maximum capacity given by Shannon's limit necessitates laying and maintaining more fiber. The capacity of multimode, few-mode, and multi-core fiber pushes that capacity into new territory<sup>1</sup>. Record transmission experiments have shown over 10 Pb/s in a single fiber [145], while transmission of 45 modes in fiber has been demonstrated as well [146, 147]. Fiber amplifiers for MDM have also been shown, allowing long-distance transmission [148]. However, optical networks rely on switches based on micro-electro-mechanical systems (MEMS) or liquid crystal

---

<sup>1</sup>Orbital angular momentum is another active research area for transmission and fiber and interfacing with silicon chips [143, 144].

on silicon (LCoS) which operate as free-space components and are limited to millisecond switching speeds. In contrast, the switch demonstrated in Chapter 5 is fully integrated (allowing for robust operation) and has microsecond-scale speed. The microring switches could even be substituted for electro-optic switches with nanosecond speeds [149]. This faster switching speed allows for much higher throughputs, depending on the network load [150].

Integrated MDM can be pushed to far higher capacities than demonstrated here. Selective excitation of 7 or more TE modes in silicon waveguides has been demonstrated with wide spectral bandwidth and fabrication tolerance [151]. In addition, both polarizations may be leveraged. Polarization multiplexing is already being leveraged for silicon photonic transceivers, and in essence this technology is identical to multiplexing of spatial modes. We could project that for 10 modes (consisting of both polarizations) and 160 wavelengths across the C and L bands (corresponding to the DWDM grid) with a data rate of 64 Gb/s (using e.g. pulse-amplitude modulation [PAM4]), then the total capacity would be over 100 Tb/s. This aggregate bandwidth in a single silicon waveguide of 3  $\mu\text{m}$  width corresponds to a bandwidth density of 33 Tb/s per  $\mu\text{m}$ . The potential for high capacity I/O to electronic chips is therefore another major benefit.

A challenge facing MDM, however, is coupling between the multimode fiber and chip. Several approaches have been proposed and demonstrated based on grating couplers or edge coupling [60, 152–155], but a scalable solution has not been shown yet. In Appendix A, a novel solution is proposed for robust, scalable coupling between a few-mode fiber and a silicon chip. Efficient coupling of multimode fibers to integrated waveguides could position on-chip MDM to become a critical tool for switching and transceivers in data centers and long-haul

transmission. Modal decomposition could also find use for image processing, for example detecting visual features imaged through a multimode fiber.

As opposed to long-distance transmission, silicon photonic MDM has advantages for short-distance communications as well. Computing systems have saturated in performance due to bottlenecks in connectivity. Connections between computational units and memory need to be pushed to higher bandwidths to enable higher computing power in supercomputers, for example [150]. Additionally, optical interconnects may replace some integrated electrical wires (e.g. between cores of a multi-core CPU) due to the potential for higher bandwidth, reduced latency, and lower power consumption. Integration of electronics and photonics together [156, 157] depends on reducing the footprint of optical components, which can be considered large in comparison to transistors. The bandwidth density achievable in a single silicon waveguide supporting MDM works towards lowering the area required for photonics. The size of multiplexers may be reduced by using novel design strategies such as inverse design and genetic algorithms [158, 159]. Tight requirements for power consumption may require reducing the number of lasers, but higher bandwidth capacity may be achieved by using modes instead [160]. For example, a single laser using 10 modes and 128 Gb/s ring modulators [161] can achieve over 1 Tb/s capacity, avoiding the power consumption, complexity, and packaging costs of multiple lasers.

## 8.2 Narrow linewidth lasers

There are many paths for expanding the capabilities of lasers based on silicon nitride. Due to the high  $Q$ s that are achievable using integrated microresonators, there is a path towards ultra-narrow linewidth tunable integrated lasers. The demonstrated linewidth of 13 kHz in Chapter 6 could likely be narrowed considerably by addressing sources of technical noise through packaging the integrated laser. Higher output powers can be obtained by proper packaging, including thermal management and heatsinking, as the demonstrated laser could then operate at much higher pump currents. Further investigation into the mechanisms causing the backscattering which results in the mode splitting and reflection in microresonators could provide further design insight [162]. There are also strategies to dynamically control the backscattering in microresonators [163], and other methods, such as intentionally adding periodic scattering points in lithography, may also prove useful.

A compact, integrated narrow-linewidth laser could be used in silicon photonic transceivers leveraging coherent communications. For example, the use of a single laser with several spatial modes and coherent modulation formats (such as 16QAM) could expand bandwidth capacities even further. The precision of narrow-linewidth lasers can also be useful for sensing, because precise phase sensitivity is needed to detect small changes in refractive index. Additionally, coherent lidar needs narrow-linewidth lasers for long distance ranging.

While silicon nitride is attractive for its low propagation loss, integration compatibility, and high index contrast, it does not inherently support high-speed tunability. However, it is possible to integrate graphene, for example, on

silicon nitride to enable fast modulation [164], and that could enable many new possibilities. With high-speed operation, the laser could also be directly modulated to allow for reduced cost, energy consumption, and area [165]. Other materials may also be considered, such as lithium niobate, which may now be integrated into compact modulators [166] and high quality factor microresonators [167]. However, its ease of fabrication and CMOS-compatibility are unfavorable in comparison to silicon nitride.

### **8.3 Microresonator frequency combs**

The integrated comb source presented in Chapter 7 demonstrates the feasibility of achieving low-power and portable frequency comb generation using silicon nitride microresonators. Comprehensive packaging of the comb source, including bonding the output fiber and electrical connections, should allow for operation outside of the laboratory. In addition to the low nonlinear threshold enabling low power consumption, such portability also relies on the robustness of the integration. It is crucial that the microresonator, including its coupling to the bus waveguide, is fully integrated and clad, preventing variations in the coupling gap or other interference from the environment. The coupling between the RSOA and silicon chip is far less sensitive though, so some misalignment during packaging can be tolerated. However, new approaches to coupling may allow a more reliable interface between the gain section and silicon chip. For example, the RSOA may be placed in a trench on the silicon chip which has been etched precisely and lithographically aligned to the integrated waveguide. The RSOA may alternately be bonded on top of the silicon chip and use gratings to couple out-of-plane. Another critical fabrication step involves transferring the

fabrication process for low-loss silicon nitride to use photolithography and low-temperature deposition methods on large wafers. This would reduce costs and promote commercial development of the platform.

The versatility of the integrated frequency comb platform allows custom designs for many applications that have previously been investigated for combs. For example, dual-comb spectroscopy using microresonators [115,116] allows for absorption in liquids and gases to be determined by the beat notes generated by interfering two combs. The high repetition rate achieved using compact microresonators with approximately 100  $\mu\text{m}$  radius results in very fast acquisition times, or, equivalently, rapid averaging over many samples. The fully-integrated comb source demonstrated here could allow for widespread use of dual-comb spectroscopy. The low power consumption, portability, and robustness potentially make the platform practical for wearable sensors monitoring biological markers, for example, while wafer-scale fabrication supports high-volume manufacturing. The flexibility in designing the laser and microresonator is conducive to investigating more efficient dual-comb designs, perhaps splitting the laser output and generating combs with two resonators to enable dispersive measurements in addition to absorption [116]. Other novel designs leveraging the counter-propagating beams may also produce dual-comb setups [168]. Additionally, pushing integrated combs into the mid-infrared spectral region would be beneficial for detecting molecular signatures [169].

For optical communications, soliton frequency combs provide many precisely-spaced carrier wavelengths for WDM. Over 50 Tb/s capacity using microresonator combs has been demonstrated, using almost 200 wavelengths [121]. Rather than requiring an array of continuous-wave lasers, Kerr

combs only need a single pump laser. Therefore, ultra-high bandwidth capacity using WDM may be realized without the need for integration of many lasers, removing some of the constraints discussed at the beginning of this chapter: implementing many wavelength and mode channels for ultra-high bandwidth density on-chip may be realized without overly complicating packaging. An important consideration would be the comb generation efficiency, but using normal dispersion instead of anomalous may be a path towards higher efficiencies. Combs based on normal dispersion have demonstrated over 30% efficiency [170]. Kerr combs are therefore an attractive technology for realizing WDM on-chip using a single laser.

APPENDIX A  
COUPLING TO MULTIMODE FIBER

Just as coupling between single-mode fiber and silicon waveguides was one of the major advancements allowing the growth of silicon photonics [74], an important advance in mode-division multiplexing may come from the ability to efficiently couple between multimode fibers and integrated waveguides. Typically this is not possible by edge coupling to silicon waveguides because nanotapers are inherently single mode. Horn tapers are only multimode in one direction, so at best one of the first higher-order modes may couple, but those that are multimode in the vertical direction would not couple. Grating couplers may be arranged to couple to certain lower-order modes, but they are inherently bandwidth-limited, and this solution is likely not scalable.

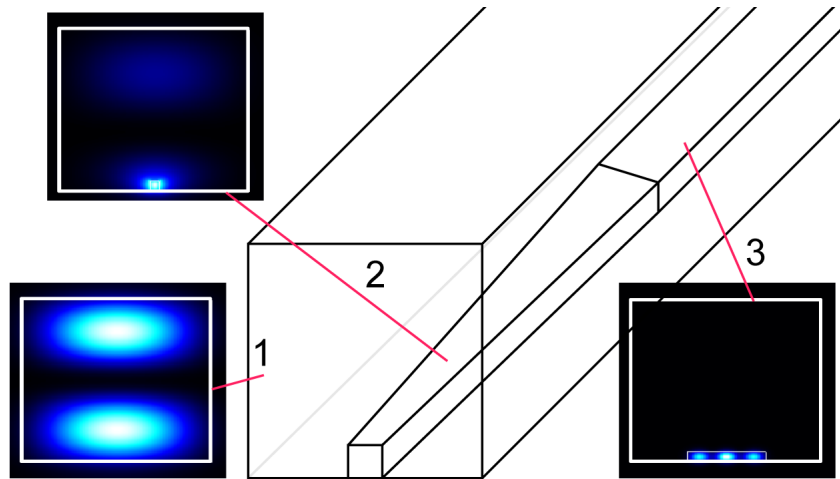


Figure A.1: Diagram of an adiabatic multimode fiber coupler. Light from a few-mode fiber couples to a large integrated intermediate waveguide and then adiabatically to a silicon waveguide.

We have proposed using adiabatic coupling to convert modes from fiber to silicon waveguides. Figure A.1 shows the approach. An intermediate waveguide similar in size to the fiber core is integrated over the silicon waveguide. The

intermediate waveguide has modes corresponding almost exactly to those of the fiber. As light propagates in the intermediate waveguide, the silicon waveguide tapers wider, from single mode until it supports the same number of modes as the original fiber. Modes "leak" into the silicon waveguide as it supports more and more modes. By designing the geometry of this coupler, modes can couple in one-to-one correspondence into the silicon waveguide, with very low loss. Demonstration of such a coupler would be a major advancement for silicon photonics and multimode multiplexing.

## BIBLIOGRAPHY

- [1] R. Kazarinov and C. Henry, "The relation of line narrowing and chirp reduction resulting from the coupling of a semiconductor laser to passive resonator," *IEEE Journal of Quantum Electronics* **23**, 1401–1409 (1987).
- [2] C. R. Pollock, *Fundamentals of Optoelectronics* (Irwin, 1995).
- [3] L. A. Coldren, S. W. Corzine, and M. L. Mashanovitch, *Diode Lasers and Photonic Integrated Circuits* (John Wiley & Sons, 2012).
- [4] Q. Xu, B. Schmidt, S. Pradhan, and M. Lipson, "Micrometre-scale silicon electro-optic modulator," *Nature* **435**, 325–327 (2005).
- [5] P. Dong, S. F. Preble, and M. Lipson, "All-optical compact silicon comb switch," *Optics Express* **15**, 9600–9605 (2007).
- [6] S. Werquin, S. Verstuyft, and P. Bienstman, "Integrated interferometric approach to solve microring resonance splitting in biosensor applications," *Optics Express* **21**, 16955–16963 (2013).
- [7] A. G. Griffith, R. K. W. Lau, J. Cardenas, Y. Okawachi, A. Mohanty, R. Fain, Y. H. D. Lee, M. Yu, C. T. Phare, C. B. Poitras, A. L. Gaeta, and M. Lipson, "Silicon-chip mid-infrared frequency comb generation," *Nature Communications* **6**, 6299 (2015).
- [8] M. Soltani, "Novel integrated silicon nanophotonic structures using ultra-high Q resonators," PhD. Thesis (Georgia Tech) (2009).
- [9] A. Yariv, "Universal relations for coupling of optical power between microresonators and dielectric waveguides," *Electronics Letters* **36**, 321–322 (2000).
- [10] K. Kieu and M. Mansuripur, "Fiber laser using a microsphere resonator as a feedback element," *Optics Letters* **32**, 244–246 (2007).
- [11] R. Soref and B. Bennett, "Electrooptical effects in silicon," *IEEE Journal of Quantum Electronics* **23**, 123–129 (1987).
- [12] P. Dong, S. Liao, D. Feng, H. Liang, D. Zheng, R. Shafiiha, C.-C. Kung, W. Qian, G. Li, X. Zheng, A. V. Krishnamoorthy, and M. Asghari, "Low

- Vpp, ultralow-energy, compact, high-speed silicon electro-optic modulator," *Optics Express* **17**, 22484 (2009).
- [13] M. Bruel, B. Aspar, and A.-J. Auberton-Herv, "Smart-Cut: A New Silicon On Insulator Material Technology Based on Hydrogen Implantation and Wafer Bonding," *Japanese Journal of Applied Physics* **36**, 1636 (1997).
- [14] O. Svelto, *Principles of Lasers* (Springer Science & Business Media, 2012).
- [15] M. Seimetz, "Laser Linewidth Limitations for Optical Systems with High-Order Modulation Employing Feed Forward Digital Carrier Phase Estimation," in "OFC/NFOEC 2008 - 2008 Conference on Optical Fiber Communication/National Fiber Optic Engineers Conference," (2008), pp. 1–3.
- [16] C. Henry, "Theory of the linewidth of semiconductor lasers," *IEEE Journal of Quantum Electronics* **18**, 259–264 (1982).
- [17] P. A. Franken, A. E. Hill, C. W. Peters, and G. Weinreich, "Generation of Optical Harmonics," *Physical Review Letters* **7**, 118–119 (1961).
- [18] R. W. Boyd, *Nonlinear Optics* (Academic Press, 2013).
- [19] J. E. Sharping, M. Fiorentino, A. Coker, P. Kumar, and R. S. Windeler, "Four-wave mixing in microstructure fiber," *Optics Letters* **26**, 1048–1050 (2001).
- [20] A. B. Matsko, A. A. Savchenkov, D. Strekalov, V. S. Ilchenko, and L. Maleki, "Optical hyperparametric oscillations in a whispering-gallery-mode resonator: Threshold and phase diffusion," *Physical Review A* **71**, 033804 (2005).
- [21] X. Ji, F. A. S. Barbosa, S. P. Roberts, A. Dutt, J. Cardenas, Y. Okawachi, A. Bryant, A. L. Gaeta, and M. Lipson, "Ultra-low-loss on-chip resonators with sub-milliwatt parametric oscillation threshold," *Optica* **4**, 619–624 (2017).
- [22] P. Del'Haye, A. Schliesser, O. Arcizet, T. Wilken, R. Holzwarth, and T. J. Kippenberg, "Optical frequency comb generation from a monolithic microresonator," *Nature* **450**, 1214–1217 (2007).
- [23] J. S. Levy, A. Gondarenko, M. A. Foster, A. C. Turner-Foster, A. L. Gaeta,

- and M. Lipson, "CMOS-compatible multiple-wavelength oscillator for on-chip optical interconnects," *Nature Photonics* **4**, 37–40 (2010).
- [24] A. Hasegawa and F. Tappert, "Transmission of stationary nonlinear optical pulses in dispersive dielectric fibers. I. Anomalous dispersion," *Applied Physics Letters* **23**, 142–144 (1973).
- [25] L. F. Mollenauer, R. H. Stolen, and J. P. Gordon, "Experimental Observation of Picosecond Pulse Narrowing and Solitons in Optical Fibers," *Physical Review Letters* **45**, 1095–1098 (1980).
- [26] T. Herr, V. Brasch, J. D. Jost, C. Y. Wang, N. M. Kondratiev, M. L. Gorodetsky, and T. J. Kippenberg, "Temporal solitons in optical microresonators," *Nature Photonics* **8**, 145–152 (2014).
- [27] B.-T. Lee and S.-Y. Shin, "Mode-order converter in a multimode waveguide," *Optics Letters* **28**, 1660–1662 (2003).
- [28] M. Greenberg and M. Orenstein, "Multimode add-drop multiplexing by adiabatic linearly tapered coupling," *Optics Express* **13**, 9381–9387 (2005).
- [29] S. Bagheri and W. Green, "Silicon-on-insulator mode-selective add-drop unit for on-chip mode-division multiplexing," in "6th IEEE International Conference on Group IV Photonics, 2009. GFP '09," (2009), pp. 166–168.
- [30] A. Ruege and R. Reano, "Multimode Waveguides Coupled to Single Mode Ring Resonators," *Journal of Lightwave Technology* **27**, 2035–2043 (2009).
- [31] L. H. Frandsen, Y. Elesin, L. F. Frellsen, M. Mitrovic, Y. Ding, O. Sigmund, and K. Yvind, "Topology optimized mode conversion in a photonic crystal waveguide fabricated in silicon-on-insulator material," *Optics Express* **22**, 8525–8532 (2014).
- [32] M. Heinrich, M.-A. Miri, S. Sttzer, R. El-Ganainy, S. Nolte, A. Szameit, and D. N. Christodoulides, "Supersymmetric mode converters," *Nature Communications* **5** (2014).
- [33] N. Hanzawa, K. Saitoh, T. Sakamoto, T. Matsui, K. Tsujikawa, M. Koshiba, and F. Yamamoto, "Mode multi/demultiplexing with parallel waveguide for mode division multiplexed transmission," *Optics Express* **22**, 29321–29330 (2014).

- [34] W. Chen, P. Wang, and J. Yang, "Mode multi/demultiplexer based on cascaded asymmetric Y-junctions," *Optics Express* **21**, 25113–25119 (2013).
- [35] C. P. Chen, J. Driscoll, B. Souhan, R. Grote, X. Zhu, R. M. Osgood, and K. Bergman, "Experimental Demonstration of Spatial Scaling for High-Throughput Transmission Through A Si Mode-Division-Multiplexing Waveguide," in "Advanced Photonics for Communications," (Optical Society of America, 2014), OSA Technical Digest (online), p. IM2A.3.
- [36] J. B. Driscoll, R. R. Grote, B. Souhan, J. I. Dadap, M. Lu, and R. M. Osgood, "Asymmetric Y junctions in silicon waveguides for on-chip mode-division multiplexing," *Optics Letters* **38**, 1854–1856 (2013).
- [37] J. B. Driscoll, C. P. Chen, R. R. Grote, B. Souhan, J. I. Dadap, A. Stein, M. Lu, K. Bergman, and R. M. Osgood, "A 60 Gb/s MDM-WDM Si photonic link with  $< 0.7$  dB power penalty per channel," *Optics Express* **22**, 18543–18555 (2014).
- [38] T. Uematsu, Y. Ishizaka, Y. Kawaguchi, K. Saitoh, and M. Koshiba, "Design of a Compact Two-Mode Multi/Demultiplexer Consisting of Multimode Interference Waveguides and a Wavelength-Insensitive Phase Shifter for Mode-Division Multiplexing Transmission," *Journal of Lightwave Technology* **30**, 2421–2426 (2012).
- [39] J. Wang, P. Chen, S. Chen, Y. Shi, and D. Dai, "Improved 8-channel silicon mode demultiplexer with grating polarizers," *Optics Express* **22**, 12799 (2014).
- [40] J. Wang, S. Chen, P. Chen, Y. Shi, and D. Dai, "64-channel hybrid (de)multiplexer enabling wavelength- and mode-division multiplexing for on-chip optical interconnects," in "Asia Communications and Photonics Conference 2014," (Optical Society of America, 2014), OSA Technical Digest (online), p. ATh1A.7.
- [41] M. Yin, Q. Deng, Y. Li, X. Wang, and H. Li, "Compact and broadband mode multiplexer and demultiplexer based on asymmetric plasmonic dielectric coupling," *Applied Optics* **53**, 6175–6180 (2014).
- [42] Y. Ding, J. Xu, F. Da Ros, B. Huang, H. Ou, and C. Peucheret, "On-chip two-mode division multiplexing using tapered directional coupler-based mode multiplexer and demultiplexer," *Optics Express* **21**, 10376–10382 (2013).

- [43] Y.-D. Yang, Y. Li, Y.-Z. Huang, and A. W. Poon, "Silicon nitride three-mode division multiplexing and wavelength-division multiplexing using asymmetrical directional couplers and microring resonators," *Optics Express* **22**, 22172–22183 (2014).
- [44] L.-W. Luo, N. Ophir, C. P. Chen, L. H. Gabrielli, C. B. Poitras, K. Bergmen, and M. Lipson, "WDM-compatible mode-division multiplexing on a silicon chip," *Nature Communications* **5** (2014).
- [45] T. Mulugeta and M. Rasras, "Silicon hybrid (de)multiplexer enabling simultaneous mode and wavelength-division multiplexing," *Optics Express* **23**, 943–949 (2015).
- [46] B. A. Dorin and W. N. Ye, "Two-mode division multiplexing in a silicon-on-insulator ring resonator," *Optics Express* **22**, 4547–4558 (2014).
- [47] H. Chen, R. van Uden, C. Okonkwo, and T. Koonen, "Compact spatial multiplexers for mode division multiplexing," *Optics Express* **22**, 31582–31594 (2014).
- [48] V. R. Almeida, C. A. Barrios, R. R. Panepucci, and M. Lipson, "All-optical control of light on a silicon chip," *Nature* **431**, 1081–1084 (2004).
- [49] M. Yang, W. M. J. Green, S. Assefa, J. Van Campenhout, B. G. Lee, C. V. Jahnes, F. E. Doany, C. L. Schow, J. A. Kash, and Y. A. Vlasov, "Non-Blocking 4x4 Electro-Optic Silicon Switch for On-Chip Photonic Networks," *Optics Express* **19**, 47–54 (2011).
- [50] R. Ji, L. Yang, L. Zhang, Y. Tian, J. Ding, H. Chen, Y. Lu, P. Zhou, and W. Zhu, "Five-port optical router for photonic networks-on-chip," *Optics Express* **19**, 20258–20268 (2011).
- [51] A. Biberman, K. Preston, G. Hendry, N. Sherwood-Droz, J. Chan, J. S. Levy, M. Lipson, and K. Bergman, "Photonic Network-on-chip Architectures Using Multilayer Deposited Silicon Materials for High-performance Chip Multiprocessors," *J. Emerg. Technol. Comput. Syst.* **7**, 7:1–7:25 (2011).
- [52] B. G. Lee, A. V. Rylyakov, W. M. J. Green, S. Assefa, C. W. Baks, R. Rimolo-Donadio, D. M. Kuchta, M. H. Khater, T. Barwicz, C. Reinholm, E. Kiewra, S. M. Shank, C. L. Schow, and Y. A. Vlasov, "Monolithic Silicon Integration of Scaled Photonic Switch Fabrics, CMOS Logic, and Device Driver Circuits," *Journal of Lightwave Technology* **32**, 743–751 (2014).

- [53] D. J. Richardson, J. M. Fini, and L. E. Nelson, "Space-division multiplexing in optical fibres," *Nature Photonics* **7**, 354–362 (2013).
- [54] P. J. Winzer, "Making spatial multiplexing a reality," *Nature Photonics* **8**, 345–348 (2014).
- [55] K. Igarashi, T. Tsuritani, I. Morita, Y. Tsuchida, K. Maeda, M. Tadakuma, T. Saito, K. Watanabe, K. Imamura, R. Sugizaki, and M. Suzuki, "Super-Nyquist-WDM transmission over 7,326-km seven-core fiber with capacity-distance product of 1.03 Exabit/s km," *Optics Express* **22**, 1220–1228 (2014).
- [56] J. Sakaguchi, B. Puttnam, W. Klaus, Y. Awaji, N. Wada, A. Kanno, T. Kawanishi, K. Imamura, H. Inaba, K. Mukasa, R. Sugizaki, T. Kobayashi, and M. Watanabe, "305 Tb/s Space Division Multiplexed Transmission Using Homogeneous 19-Core Fiber," *Journal of Lightwave Technology* **31**, 554–562 (2013).
- [57] R. G. H. van Uden, R. A. Correa, E. A. Lopez, F. M. Huijskens, C. Xia, G. Li, A. Schlzgen, H. d. Waardt, A. M. J. Koonen, and C. M. Okonkwo, "Ultra-high-density spatial division multiplexing with a few-mode multicore fibre," *Nature Photonics* **8**, 865–870 (2014).
- [58] N. Amaya, M. Irfan, G. Zervas, R. Nejabati, D. Simeonidou, J. Sakaguchi, W. Klaus, B. Puttnam, T. Miyazawa, Y. Awaji, N. Wada, and I. Henning, "Fully-elastic multi-granular network with space/frequency/time switching using multi-core fibres and programmable optical nodes," *Optics Express* **21**, 8865 (2013).
- [59] H. Takara, A. Sano, T. Kobayashi, H. Kubota, H. Kawakami, A. Matsuura, Y. Miyamoto, Y. Abe, H. Ono, K. Shikama, Y. Goto, K. Tsujikawa, Y. Sasaki, I. Ishida, K. Takenaga, S. Matsuo, K. Saitoh, M. Koshihara, and T. Morioka, "1.01-Pb/s (12 SDM/222 WDM/456 Gb/s) Crosstalk-managed Transmission with 91.4-b/s/Hz Aggregate Spectral Efficiency," in "European Conference and Exhibition on Optical Communication," (Optical Society of America, 2012), OSA Technical Digest (online), p. Th.3.C.1.
- [60] N. K. Fontaine, C. R. Doerr, M. A. Mestre, R. Ryf, P. Winzer, L. Buhl, Y. Sun, X. Jiang, and R. Lingle, "Space-division multiplexing and all-optical MIMO demultiplexing using a photonic integrated circuit," in "Optical Fiber Communication Conference," (Optical Society of America, 2012), OSA Technical Digest, p. PDP5B.1.

- [61] S. Randel, R. Ryf, A. Sierra, P. J. Winzer, A. H. Gnauck, C. A. Bolle, R.-J. Essiambre, D. W. Peckham, A. McCurdy, and R. Lingle, "6x56-Gb/s mode-division multiplexed transmission over 33-km few-mode fiber enabled by 6x6 MIMO equalization," *Optics Express* **19**, 16697 (2011).
- [62] R. Ryf, S. Randel, A. Gnauck, C. Bolle, A. Sierra, S. Mumtaz, M. Esmaelpour, E. Burrows, R. Essiambre, P. Winzer, D. Peckham, A. McCurdy, and R. Lingle, "Mode-Division Multiplexing Over 96 km of Few-Mode Fiber Using Coherent 6x6 MIMO Processing," *Journal of Lightwave Technology* **30**, 521–531 (2012).
- [63] R. Ryf, N. K. Fontaine, H. Chen, B. Guan, B. Huang, M. Esmaelpour, A. H. Gnauck, S. Randel, S. Yoo, A. Koonen, R. Shubochkin, Y. Sun, and R. Lingle, "Mode-multiplexed transmission over conventional graded-index multimode fibers," *Optics Express* **23**, 235–246 (2015).
- [64] K.-P. Ho, J. M. Kahn, and J. P. Wilde, "Wavelength-Selective Switches for Mode-Division Multiplexing: Scaling and Performance Analysis," *Journal of Lightwave Technology* **32**, 3724–3735 (2014).
- [65] R. Ryf, N. Fontaine, J. Dunayevsky, D. Sinefeld, M. Blau, M. Montoliu, S. Randel, C. Liu, B. Ercan, M. Esmaelpour, S. Chandrasekhar, A. Gnauck, S. Leon-Saval, J. Bland-Hawthorn, J. Salazar-Gil, Y. Sun, L. Gruner-Nielsen, R. Lingle, and D. Marom, "Wavelength-selective switch for few-mode fiber transmission," in "39th European Conference and Exhibition on Optical Communication (ECOC 2013)," (2013), pp. 1–3.
- [66] X. Chen, A. Li, J. Ye, A. Al Amin, and W. Shieh, "Demonstration of Few-Mode Compatible Optical Add/Drop Multiplexer for Mode-Division Multiplexed Superchannel," *Journal of Lightwave Technology* **31**, 641–647 (2013).
- [67] R. Y. Gu, E. Ip, M.-J. Li, Y.-K. Huang, and J. M. Kahn, "Experimental Demonstration of a Spatial Light Modulator Few-Mode Fiber Switch for Space-Division Multiplexing," in "Frontiers in Optics 2013 Postdeadline," (Optical Society of America, 2013), OSA Postdeadline Paper Digest (online), p. FW6B.4.
- [68] J. A. Carpenter, S. G. Leon-Saval, J. R. Salazar Gil, J. Bland-Hawthorn, G. Baxter, L. Stewart, S. Frisken, M. A. Roelens, B. J. Eggleton, and J. Schröder, "1x11 Few-Mode Fiber Wavelength Selective Switch using Photonic Lanterns," in "Optical Fiber Communication Conference," (Optical Society of America, 2014), OSA Technical Digest (online), p. Th4A.2.

- [69] M. Cvijetic, I. B. Djordjevic, and N. Cvijetic, "Dynamic multidimensional optical networking based on spatial and spectral processing," *Optics Express* **20**, 9144–9150 (2012).
- [70] D. Dai, J. Wang, and S. He, "Silicon multimode photonic integrated devices for on-chip mode-division-multiplexed optical interconnects," *Progress In Electromagnetics Research* **143**, 773–819 (2013).
- [71] N. Sherwood-Droz, H. Wang, L. Chen, B. G. Lee, A. Biberman, K. Bergman, and M. Lipson, "Optical 4x4 hitless silicon router for optical networks-on-chip (NoC)," *Optics Express* **16**, 15915–15922 (2008).
- [72] J. Chan, N. Ophir, C. P. Lai, A. Biberman, H. L. R. Lira, M. Lipson, and K. Bergman, "Data Transmission Using Wavelength-Selective Spatial Routing for Photonic Interconnection Networks," in "Optical Fiber Communication Conference/National Fiber Optic Engineers Conference 2011," (Optical Society of America, 2011), OSA Technical Digest (CD), p. OThQ3.
- [73] J. Cardenas, C. Poitras, K. Luke, L. Luo, P. Morton, and M. Lipson, "High Coupling Efficiency Etched Facet Tapers in Silicon Waveguides," *IEEE Photonics Technology Letters* **26**, 2380–2382 (2014).
- [74] V. R. Almeida, R. R. Panepucci, and M. Lipson, "Nanotaper for compact mode conversion," *Optics Letters* **28**, 1302–1304 (2003).
- [75] L.-W. Luo, S. Ibrahim, A. Nitkowski, Z. Ding, C. B. Poitras, S. J. Ben Yoo, and M. Lipson, "High bandwidth on-chip silicon photonic interleaver," *Optics Express* **18**, 23079 (2010).
- [76] V. Kopp, J. Park, M. Wlodawski, J. Singer, D. Neugroschl, and A. Genack, "Pitch Reducing Optical Fiber Array for dense optical interconnect," in "2012 IEEE Avionics, Fiber- Optics and Photonics Technology Conference (AVFOP)," (2012), pp. 48–49.
- [77] H. A. Haus, *Waves and Fields in Optoelectronics*, vol. 1 (Prentice-Hall, 1984).
- [78] Y. A. Vlasov and S. J. McNab, "Losses in single-mode silicon-on-insulator strip waveguides and bends," *Optics Express* **12**, 1622 (2004).
- [79] M. G. Wood, L. Chen, J. R. Burr, and R. M. Reano, "Optimization of electron beam patterned hydrogen silsesquioxane mask edge roughness for

- low-loss silicon waveguides," *Journal of Nanophotonics* **8**, 083098–083098 (2014).
- [80] R. Hendry, D. Nikolova, S. Rumley, N. Ophir, and K. Bergman, "Physical Layer Analysis and Modeling of Silicon Photonic WDM Bus Architectures," (HiPEAC, 2014).
- [81] B. Jalali and S. Fathpour, "Silicon Photonics," *Journal of Lightwave Technology* **24**, 4600–4615 (2006).
- [82] Z. Zhou, B. Yin, Q. Deng, X. Li, and J. Cui, "Lowering the energy consumption in silicon photonic devices and systems [Invited]," *Photonics Research* **3**, B28 (2015).
- [83] H. Ishii, K. Kasaya, H. Oohashi, Y. Shibata, H. Yasaka, and K. Okamoto, "Widely Wavelength-Tunable DFB Laser Array Integrated With Funnel Combiner," *IEEE Journal of Selected Topics in Quantum Electronics* **13**, 1089–1094 (2007).
- [84] A. Biberman, S. Manipatruni, N. Ophir, L. Chen, M. Lipson, and K. Bergman, "First demonstration of long-haul transmission using silicon microring modulators," *Optics Express* **18**, 15544 (2010).
- [85] B. J. Puttnam, R. S. Lus, W. Klaus, J. Sakaguchi, J. M. D. Mendinueta, Y. Awaji, N. Wada, Y. Tamura, T. Hayashi, M. Hirano, and J. Marciante, "2.15 Pb/s transmission using a 22 core homogeneous single-mode multi-core fiber and wideband optical comb," in "2015 European Conference on Optical Communication (ECOC)," (2015), pp. 1–3.
- [86] I. M. White, H. Zhu, J. D. Suter, N. M. Hanumegowda, H. Oveys, M. Zourob, and X. Fan, "Refractometric Sensors for Lab-on-a-Chip Based on Optical Ring Resonators," *IEEE Sensors Journal* **7**, 28–35 (2007).
- [87] W.-C. Lai, S. Chakravarty, X. Wang, C. Lin, and R. T. Chen, "Photonic crystal slot waveguide absorption spectrometer for on-chip near-infrared spectroscopy of xylene in water," *Applied Physics Letters* **98**, 023304 (2011).
- [88] E. Dale, W. Liang, D. Eliyahu, A. Savchenkov, V. Ilchenko, A. B. Matsko, D. Seidel, and L. Maleki, "Ultra-Narrow Line Tunable Semiconductor Lasers for Coherent LIDAR Applications," in "Imaging and Applied Optics 2014 (2014), paper JTu2C.3," (Optical Society of America, 2014), p. JTu2C.3.

- [89] N. Prtljaga, C. Bentham, J. O'Hara, B. Royall, E. Clarke, L. R. Wilson, M. S. Skolnick, and A. M. Fox, "On-chip interference of single photons from an embedded quantum dot and an external laser," *Applied Physics Letters* **108**, 251101 (2016).
- [90] B. J. Bloom, T. L. Nicholson, J. R. Williams, S. L. Campbell, M. Bishof, X. Zhang, W. Zhang, S. L. Bromley, and J. Ye, "An optical lattice clock with accuracy and stability at the 10<sup>-18</sup> level," *Nature* **506**, 71–75 (2014).
- [91] C. R. Doerr, L. Chen, D. Vermeulen, T. Nielsen, S. Azemati, S. Stulz, G. McBrien, X.-M. Xu, B. Mikkelsen, M. Givehchi, C. Rasmussen, and S. Y. Park, "Single-Chip Silicon Photonics 100-Gb/s Coherent Transceiver," in "Optical Fiber Communication Conference: Postdeadline Papers (2014), paper Th5C.1," (Optical Society of America, 2014), p. Th5C.1.
- [92] P. Dong, X. Liu, S. Chandrasekhar, L. L. Buhl, R. Aroca, and Y. K. Chen, "Monolithic Silicon Photonic Integrated Circuits for Compact 100+ Gb/s Coherent Optical Receivers and Transmitters," *IEEE Journal of Selected Topics in Quantum Electronics* **20**, 150–157 (2014).
- [93] Y. de Koninck, G. Roelkens, and R. Baets, "Design of a Hybrid III-V-on-Silicon Microlaser With Resonant Cavity Mirrors," *IEEE Photonics Journal* **5**, 2700413–2700413 (2013).
- [94] T. Komljenovic, S. Srinivasan, E. Norberg, M. Davenport, G. Fish, and J. E. Bowers, "Widely Tunable Narrow-Linewidth Monolithically Integrated External-Cavity Semiconductor Lasers," *IEEE Journal of Selected Topics in Quantum Electronics* **21**, 214–222 (2015).
- [95] Z. Wang, B. Tian, M. Pantouvaki, W. Guo, P. Absil, J. Van Campenhout, C. Merckling, and D. Van Thourhout, "Room-temperature InP distributed feedback laser array directly grown on silicon," *Nature Photonics* **9**, 837–842 (2015).
- [96] N. Fujioka, T. Chu, and M. Ishizaka, "Compact and Low Power Consumption Hybrid Integrated Wavelength Tunable Laser Module Using Silicon Waveguide Resonators," *Journal of Lightwave Technology* **28**, 3115–3120 (2010).
- [97] J.-H. Lee, J. Bovington, I. Shubin, Y. Luo, J. Yao, S. Lin, J. E. Cunningham, K. Raj, A. V. Krishnamoorthy, and X. Zheng, "Demonstration of 122% wall plug efficiency in uncooled single mode external-cavity tunable Si/III-V hybrid laser," *Optics Express* **23**, 12079 (2015).

- [98] N. Kobayashi, K. Sato, M. Namiwaka, K. Yamamoto, S. Watanabe, T. Kita, H. Yamada, and H. Yamazaki, "Silicon Photonic Hybrid Ring-Filter External Cavity Wavelength Tunable Lasers," *Journal of Lightwave Technology* **33**, 1241–1246 (2015).
- [99] S. Yang, Y. Zhang, D. W. Grund, G. A. Ejzak, Y. Liu, A. Novack, D. Prather, A. E.-J. Lim, G.-Q. Lo, T. Baehr-Jones, and M. Hochberg, "A single adiabatic microring-based laser in 220 nm silicon-on-insulator," *Optics Express* **22**, 1172–1180 (2014).
- [100] D. T. H. Tan, K. Ikeda, P. C. Sun, and Y. Fainman, "Group velocity dispersion and self phase modulation in silicon nitride waveguides," *Applied Physics Letters* **96**, 061101 (2010).
- [101] R. M. Oldenbeuving, E. J. Klein, H. L. Offerhaus, C. J. Lee, H. Song, and K.-J. Boller, "25 kHz narrow spectral bandwidth of a wavelength tunable diode laser with a short waveguide-based external cavity," *Laser Physics Letters* **10**, 015804 (2013).
- [102] Y. Fan, R. M. Oldenbeuving, E. J. Klein, C. J. Lee, H. Song, M. R. H. Khan, H. L. Offerhaus, P. J. M. van der Slot, and K.-J. Boller, "A hybrid semiconductor-glass waveguide laser," in "Proc. SPIE," , vol. 9135 (2014), vol. 9135.
- [103] J. L. Zhao, R. M. Oldenbeuving, J. P. Epping, M. Hoekman, R. G. Heideman, R. Dekker, Y. Fan, K. J. Boller, R. Q. Ji, S. M. Fu, and L. Zeng, "Narrow-linewidth widely tunable hybrid external cavity laser using Si<sub>3</sub>N<sub>4</sub>/SiO<sub>2</sub> microring resonators," in "2016 IEEE 13th International Conference on Group IV Photonics (GFP)," (2016), pp. 24–25.
- [104] Y. Fan, J. P. Epping, R. M. Oldenbeuving, C. G. H. Roeloffzen, M. Hoekman, R. Dekker, R. G. Heideman, P. J. M. v. d. Slot, and K. J. Boller, "Optically Integrated InP Si N Hybrid Laser," *IEEE Photonics Journal* **8**, 1–11 (2016).
- [105] D. T. Spencer, M. L. Davenport, T. Komljenovic, S. Srinivasan, and J. E. Bowers, "Stabilization of heterogeneous silicon lasers using Pound-Drever-Hall locking to Si<sub>3</sub>N<sub>4</sub> ring resonators," *Optics Express* **24**, 13511–13517 (2016).
- [106] M. Borselli, T. J. Johnson, and O. Painter, "Beyond the Rayleigh scattering limit in high-Q silicon microdisks: theory and experiment," *Optics Express* **13**, 1515–1530 (2005).

- [107] A. Biberman, M. J. Shaw, E. Timurdogan, J. B. Wright, and M. R. Watts, "Ultralow-loss silicon ring resonators," *Optics Letters* **37**, 4236–4238 (2012).
- [108] T. J. Kippenberg, S. M. Spillane, and K. J. Vahala, "Modal coupling in traveling-wave resonators," *Optics Letters* **27**, 1669–1671 (2002).
- [109] Z. Xie, W. Liang, A. A. Savchenkov, J. Lim, J. Burkhart, M. McDonald, T. Zelevinsky, V. S. Ilchenko, A. B. Matsko, L. Maleki, and C. W. Wong, "Extended ultrahigh-Q-cavity diode laser," *Optics Letters* **40**, 2596–2599 (2015).
- [110] B. Liu, A. Shakouri, and J. E. Bowers, "Passive microring-resonator-coupled lasers," *Applied Physics Letters* **79**, 3561–3563 (2001).
- [111] W. Liang, V. S. Ilchenko, A. A. Savchenkov, A. B. Matsko, D. Seidel, and L. Maleki, "Whispering-gallery-mode-resonator-based ultranarrow linewidth external-cavity semiconductor laser," *Optics Letters* **35**, 2822–2824 (2010).
- [112] J. Lim, A. A. Savchenkov, E. Dale, W. Liang, D. Eliyahu, V. Ilchenko, A. B. Matsko, L. Maleki, and C. W. Wong, "Chasing the thermodynamical noise limit in whispering-gallery-mode resonators for ultrastable laser frequency stabilization," *Nature Communications* **8** (2017).
- [113] T. Okoshi, K. Kikuchi, and A. Nakayama, "Novel method for high resolution measurement of laser output spectrum," *Electronics Letters* **16**, 630–631 (1980).
- [114] G. Villares, A. Hugi, S. Blaser, and J. Faist, "Dual-comb spectroscopy based on quantum-cascade-laser frequency combs," *Nature Communications* **5**, 5192 (2014).
- [115] M.-G. Suh, Q.-F. Yang, K. Y. Yang, X. Yi, and K. J. Vahala, "Microresonator soliton dual-comb spectroscopy," *Science* **354**, 600–603 (2016).
- [116] A. Dutt, C. Joshi, X. Ji, J. Cardenas, Y. Okawachi, K. Luke, A. L. Gaeta, and M. Lipson, "On-chip dual-comb source for spectroscopy," *Science Advances* **4**, e1701858 (2018).
- [117] J. Li, X. Yi, H. Lee, S. A. Diddams, and K. J. Vahala, "Electro-optical

- frequency division and stable microwave synthesis,” *Science* p. 1252909 (2014).
- [118] D. T. Spencer, T. Drake, T. C. Briles, J. Stone, L. C. Sinclair, C. Fredrick, Q. Li, D. Westly, B. R. Ilic, A. Bluestone, N. Volet, T. Komljenovic, L. Chang, S. H. Lee, D. Y. Oh, M.-G. Suh, K. Y. Yang, M. H. P. Pfeiffer, T. J. Kippenberg, E. Norberg, L. Theogarajan, K. Vahala, N. R. Newbury, K. Srinivasan, J. E. Bowers, S. A. Diddams, and S. B. Papp, “An Integrated-Photonics Optical-Frequency Synthesizer,” arXiv:1708.05228 [physics] (2017). ArXiv: 1708.05228.
- [119] S. B. Papp, K. Beha, P. DelHaye, F. Quinlan, H. Lee, K. J. Vahala, and S. A. Diddams, “Microresonator frequency comb optical clock,” *Optica* **1**, 10–14 (2014).
- [120] M.-G. Suh and K. J. Vahala, “Soliton microcomb range measurement,” *Science* **359**, 884–887 (2018).
- [121] P. Marin-Palomo, J. N. Kemal, M. Karpov, A. Kordts, J. Pfeifle, M. H. P. Pfeiffer, P. Trocha, S. Wolf, V. Brasch, M. H. Anderson, R. Rosenberger, K. Vijayan, W. Freude, T. J. Kippenberg, and C. Koos, “Microresonator-based solitons for massively parallel coherent optical communications,” *Nature* **546**, 274–279 (2017).
- [122] C. Reimer, L. Caspani, M. Clerici, M. Ferrera, M. Kues, M. Peccianti, A. Pasquazi, L. Razzari, B. E. Little, S. T. Chu, D. J. Moss, and R. Morandotti, “Integrated frequency comb source of heralded single photons,” *Optics Express* **22**, 6535–6546 (2014).
- [123] A. A. Savchenkov, A. B. Matsko, D. Strekalov, M. Mohageg, V. S. Ilchenko, and L. Maleki, “Low Threshold Optical Oscillations in a Whispering Gallery Mode CaF<sub>2</sub> Resonator,” *Physical Review Letters* **93**, 243905 (2004).
- [124] A. B. Matsko, A. A. Savchenkov, W. Liang, V. S. Ilchenko, D. Seidel, and L. Maleki, “Mode-locked Kerr frequency combs,” *Optics Letters* **36**, 2845–2847 (2011).
- [125] S. Coen, H. G. Randle, T. Sylvestre, and M. Erkintalo, “Modeling of octave-spanning Kerr frequency combs using a generalized mean-field Lugiato Lefever model,” *Optics Letters* **38**, 37–39 (2013).
- [126] X. Yi, Q.-F. Yang, K. Y. Yang, M.-G. Suh, and K. Vahala, “Soliton frequency

- comb at microwave rates in a high-Q silica microresonator," *Optica* **2**, 1078–1085 (2015).
- [127] V. Brasch, M. Geiselmann, T. Herr, G. Lihachev, M. H. P. Pfeiffer, M. L. Gorodetsky, and T. J. Kippenberg, "Photonic chipbased optical frequency comb using soliton Cherenkov radiation," *Science* **351**, 357–360 (2016).
- [128] P. Trocha, M. Karpov, D. Ganin, M. H. P. Pfeiffer, A. Kordts, S. Wolf, J. Krockenberger, P. Marin-Palomo, C. Weimann, S. Randel, W. Freude, T. J. Kippenberg, and C. Koos, "Ultrafast optical ranging using microresonator soliton frequency combs," *Science* **359**, 887–891 (2018).
- [129] H. Jung, C. Xiong, K. Y. Fong, X. Zhang, and H. X. Tang, "Optical frequency comb generation from aluminum nitride microring resonator," *Optics Letters* **38**, 2810–2813 (2013).
- [130] Y. Okawachi, K. Saha, J. S. Levy, Y. H. Wen, M. Lipson, and A. L. Gaeta, "Octave-spanning frequency comb generation in a silicon nitride chip," *Optics Letters* **36**, 3398–3400 (2011).
- [131] F. Ferdous, H. Miao, D. E. Leaird, K. Srinivasan, J. Wang, L. Chen, L. T. Varghese, and A. M. Weiner, "Spectral line-by-line pulse shaping of on-chip microresonator frequency combs," *Nature Photonics* **5**, 770–776 (2011).
- [132] B. Kuyken, T. Ideguchi, S. Holzner, M. Yan, T. W. Hensch, J. Van Campenhout, P. Verheyen, S. Coen, F. Leo, R. Baets, G. Roelkens, and N. Picqu, "An octave-spanning mid-infrared frequency comb generated in a silicon nanophotonic wire waveguide," *Nature Communications* **6** (2015).
- [133] B. J. M. Hausmann, I. Bulu, V. Venkataraman, P. Deotare, and M. Lonar, "Diamond nonlinear photonics," *Nature Photonics* **8**, 369–374 (2014).
- [134] A. W. Fang, H. Park, O. Cohen, R. Jones, M. J. Paniccia, and J. E. Bowers, "Electrically pumped hybrid AlGaInAs-silicon evanescent laser," *Optics Express* **14**, 9203–9210 (2006).
- [135] J. V. Campenhout, P. Rojo-Romeo, P. Regreny, C. Seassal, D. V. Thourhout, S. Verstuyft, L. D. Cioccio, J.-M. Fedeli, C. Lagahe, and R. Baets, "Electrically pumped InP-based microdisk lasers integrated with a nanophotonic silicon-on-insulator waveguide circuit," *Optics Express* **15**, 6744–6749 (2007).

- [136] B. Stern, X. Ji, A. Dutt, and M. Lipson, "Compact narrow-linewidth integrated laser based on a low-loss silicon nitride ring resonator," *Optics Letters* **42**, 4541–4544 (2017).
- [137] Y. Fan, R. M. Oldenbeuving, C. G. Roeloffzen, M. Hoekman, D. Geskus, R. G. Heideman, and K.-J. Boller, "290 Hz Intrinsic Linewidth from an Integrated Optical Chip-based Widely Tunable InP-Si<sub>3</sub>N<sub>4</sub> Hybrid Laser," in "Conference on Lasers and Electro-Optics (2017), paper JTh5C.9," (Optical Society of America, 2017), p. JTh5C.9.
- [138] M. Peccianti, A. Pasquazi, Y. Park, B. E. Little, S. T. Chu, D. J. Moss, and R. Morandotti, "Demonstration of a stable ultrafast laser based on a nonlinear microcavity," *Nature Communications* **3**, 765 (2012).
- [139] A. R. Johnson, Y. Okawachi, M. R. E. Lamont, J. S. Levy, M. Lipson, and A. L. Gaeta, "Microresonator-based comb generation without an external laser source," *Optics Express* **22**, 1394–1401 (2014).
- [140] M. R. E. Lamont, Y. Okawachi, and A. L. Gaeta, "Route to stabilized ultrabroadband microresonator-based frequency combs," *Optics Letters* **38**, 3478–3481 (2013).
- [141] B. Stern, X. Zhu, C. P. Chen, L. D. Tzuang, J. Cardenas, K. Bergman, and M. Lipson, "On-chip mode-division multiplexing switch," *Optica* **2**, 530–535 (2015).
- [142] L. Yang, T. Zhou, H. Jia, S. Yang, J. Ding, X. Fu, and L. Zhang, "General architectures for on-chip optical space and mode switching," *Optica* **5**, 180–187 (2018).
- [143] N. K. Fontaine, C. R. Doerr, and L. L. Buhl, "Efficient multiplexing and demultiplexing of free-space orbital angular momentum using photonic integrated circuits," in "OFC/NFOEC," (2012), pp. 1–3.
- [144] J. Sun, M. Moresco, G. Leake, D. Coolbaugh, and M. R. Watts, "Generating and identifying optical orbital angular momentum with silicon photonic circuits," *Optics Letters* **39**, 5977–5980 (2014).
- [145] D. Soma, Y. Wakayama, S. Beppu, S. Sumita, T. Tsuritani, T. Hayashi, T. Nagashima, M. Suzuki, M. Yoshida, K. Kasai, M. Nakazawa, H. Takahashi, K. Igarashi, I. Morita, and M. Suzuki, "10.16-Peta-B/s Dense SDM/WDM Transmission Over 6-Mode 19-Core Fiber Across the C+L Band," *Journal of Lightwave Technology* **36**, 1362–1368 (2018).

- [146] N. K. Fontaine, R. Ryf, H. Chen, D. T. Neilson, K. Kim, and J. Carpenter, "Scalable mode sorter supporting 210 Hermite-Gaussian modes," in "Optical Fiber Communication Conference Postdeadline Papers (2018), paper Th4B.4," (Optical Society of America, 2018), p. Th4B.4.
- [147] S. Bade, B. Denolle, G. Trunet, N. Riguet, P. Jian, O. Pinel, and G. Labroille, "Fabrication and Characterization of a Mode-selective 45-Mode Spatial Multiplexer based on Multi-Plane Light Conversion," in "Optical Fiber Communication Conference Postdeadline Papers (2018), paper Th4B.3," (Optical Society of America, 2018), p. Th4B.3.
- [148] E. Ip, M.-J. Li, K. Bennett, S. Bickham, Y.-K. Huang, A. Tanaka, E. Mateo, J. Hu, T. Wang, A. Korolev, K. Koreshkov, W. Wood, J. Linares, C. Montero, V. Moreno, X. Prieto, Y. Yano, Y. Aono, T. Tajima, and K. Fukuchi, "Few-mode fiber transmission with in-line few-mode erbium-doped fiber amplifier," (2013), vol. 8647, pp. 864709–864709–10.
- [149] Y. Xiong, R. B. Priti, and O. Liboiron-Ladouceur, "High-speed two-mode switch for mode-division multiplexing optical networks," *Optica* **4**, 1098–1102 (2017).
- [150] S. Rumley, M. Bahadori, R. Polster, S. D. Hammond, D. M. Calhoun, K. Wen, A. Rodrigues, and K. Bergman, "Optical interconnects for extreme scale computing systems," *Parallel Computing* **64**, 65–80 (2017).
- [151] Y.-C. Chang, S. P. Roberts, B. Stern, and M. Lipson, "Resonance-Free Light Recycling," arXiv:1710.02891 [physics] (2017). ArXiv: 1710.02891.
- [152] M. Tokushima, J. Ushida, and K. Kurata, "Folded Shallow Grating Couplers With Minimal Back Reflection and Extended Coupling Bandwidth for Robust Coupling to Multimode Fibers," *Journal of Lightwave Technology* **35**, 246–257 (2017).
- [153] J. M. Baumann, E. P. d. Silva, Y. Ding, V. Kamchevska, M. Galili, K. Dalgaard, L. Frandsen, L. K. Oxenlowe, and T. Morioka, "Silicon Chip-to-Chip Mode-Division Multiplexing," in "Optical Fiber Communication Conference (2018), paper W1E.4," (Optical Society of America, 2018), p. W1E.4.
- [154] B. Wohlfeil, G. Rademacher, C. Stamatidis, K. Voigt, L. Zimmermann, and K. Petermann, "A Two-Dimensional Fiber Grating Coupler on SOI for Mode Division Multiplexing," *IEEE Photonics Technology Letters* **28**, 1241–1244 (2016).

- [155] D. Melati, A. Alippi, and A. Melloni, "Reconfigurable photonic integrated mode (de)multiplexer for SDM fiber transmission," arXiv:1602.08414 [physics] (2016). ArXiv: 1602.08414.
- [156] C. Sun, M. T. Wade, Y. Lee, J. S. Orcutt, L. Alloatti, M. S. Georgas, A. S. Waterman, J. M. Shainline, R. R. Avizienis, S. Lin, B. R. Moss, R. Kumar, F. Pavanello, A. H. Atabaki, H. M. Cook, A. J. Ou, J. C. Leu, Y.-H. Chen, K. Asanovic, R. J. Ram, M. A. Popovic, and V. M. Stojanovic, "Single-chip microprocessor that communicates directly using light," *Nature* **528**, 534–538 (2015).
- [157] A. H. Atabaki, S. Moazeni, F. Pavanello, H. Gevorgyan, J. Notaros, L. Alloatti, M. T. Wade, C. Sun, S. A. Kruger, H. Meng, K. A. Qubaisi, I. Wang, B. Zhang, A. Khilo, C. V. Baiocco, M. A. Popovic, V. M. Stojanovic, and R. J. Ram, "Integrating photonics with silicon nanoelectronics for the next generation of systems on a chip," *Nature* **556**, 349–354 (2018).
- [158] A. Y. Piggott, J. Lu, K. G. Lagoudakis, J. Petykiewicz, T. M. Babinec, and J. Vukovi, "Inverse design and demonstration of a compact and broadband on-chip wavelength demultiplexer," *Nature Photonics* **9**, 374–377 (2015).
- [159] B. Shen, P. Wang, R. Polson, and R. Menon, "An integrated-nanophotonics polarization beamsplitter with 2.4 × 2.4 m<sup>2</sup> footprint," *Nature Photonics* **9**, 378–382 (2015).
- [160] B. Stern and M. Lipson, "High-bandwidth link with single laser input using silicon modulators and mode multiplexing," in "2016 Conference on Lasers and Electro-Optics (CLEO)," (2016), pp. 1–2.
- [161] J. Sun, M. Sakib, J. Driscoll, R. Kumar, H. Jayatilleka, Y. Chetrit, and H. Rong, "A 128 Gb/s PAM4 Silicon Microring Modulator," in "Optical Fiber Communication Conference Postdeadline Papers (2018), paper Th4A.7," (Optical Society of America, 2018), p. Th4A.7.
- [162] Q. Li, A. A. Eftekhar, Z. Xia, and A. Adibi, "Unified approach to mode splitting and scattering loss in high-Q whispering-gallery-mode microresonators," *Physical Review A* **88**, 033816 (2013).
- [163] A. Li and W. Bogaerts, "Fundamental suppression of backscattering in silicon microrings," *Optics Express* **25**, 2092–2099 (2017).

- [164] C. T. Phare, Y.-H. D. Lee, J. Cardenas, and M. Lipson, "Graphene electro-optic modulator with 30 GHz bandwidth," *Nature Photonics* **9**, 511–514 (2015).
- [165] A. Roshan-Zamir, K. Yu, D. Liang, C. Zhang, C. Li, G. Fan, B. Wang, M. Fiorentino, R. Beausoleil, and S. Palermo, "A 14 Gb/s Directly Modulated Hybrid Microring Laser Transmitter," in "Optical Fiber Communication Conference (2018), paper M1I.7," (Optical Society of America, 2018), p. M1I.7.
- [166] C. Wang, M. Zhang, B. Stern, M. Lipson, and M. Loncar, "Nanophotonic lithium niobate electro-optic modulators," *Optics Express* **26**, 1547–1555 (2018).
- [167] M. Zhang, C. Wang, R. Cheng, A. Shams-Ansari, and M. Loncar, "Monolithic ultra-high-Q lithium niobate microring resonator," *Optica* **4**, 1536–1537 (2017).
- [168] C. Joshi, A. Klenner, Y. Okawachi, M. Yu, K. Luke, X. Ji, M. Lipson, and A. L. Gaeta, "Counter-rotating cavity solitons in a silicon nitride microresonator," *Optics Letters* **43**, 547–550 (2018).
- [169] S. A. Miller, M. Yu, X. Ji, A. G. Griffith, J. Cardenas, A. L. Gaeta, and M. Lipson, "Low-loss silicon platform for broadband mid-infrared photonics," *Optica* **4**, 707–712 (2017).
- [170] X. Xue, P.-H. Wang, Y. Xuan, M. Qi, and A. M. Weiner, "Microresonator Kerr frequency combs with high conversion efficiency," *Laser & Photonics Reviews* **11**, 1600276 (2017).